Pneumatic Particulate Collection System for an Unmanned Ground Sampling Robot

Michael R. Couch

Thesis submitted to the faculty of the
Virginia Polytechnic Institute and State University
in partial fulfillment of the requirements for the degree of

Master of Science
in
Mechanical Engineering

Kevin B. Kochersberger, Chair
Alan A. Kornhauser
Mark A. Pierson

November 19, 2010
Blacksburg, VA

Keywords: Particulate Sampling, Particle Entrainment, Jet Impingement, Material Collection, Unmanned Systems

Pneumatic Particulate Collection System for an Unmanned Ground Sampling Robot

Michael R. Couch

ABSTRACT

The design of unmanned material collection systems requires a great deal of foresight and innovative design on the engineer's part in order to produce solutions to problems operators may encounter in the field. In this thesis, the development of a particulate collection system for use onboard a lightweight, helicopter deployable ground robot is presented.

The Unmanned Systems Laboratory at Virginia Tech is developing a ground sampling robot to be carried in the payload pod of a Yamaha RMAX unmanned aerial vehicle. The robot's ultimate objective is to collect material samples from a hazardous environment. The pneumatic system presented here is a novel design developed to collect particulate without draining the resources of the robot. Vacuum samplers have been developed in the past, but they are large and cumbersome and require large amounts of electrical energy to operate. The pneumatic particulate collection system utilizes the kinetic energy from the release of compressed air to transport the particulate to a collection chamber.

Consideration is given to the drop in pressure of the air supply tank as it empties, and a feasible air supply tank design is presented. Two forms of particulate collection are investigated experimentally: jet impingement and particle entrainment (i.e. steep attack angle and parallel flow). Turbulent, free jet characteristics and critical velocities of particles are studied. Ultimately, a final design is presented that effectively collects particulate material from the top 5/8" layer of both thick and thin particle beds.

To my wife and best friend, Maggie

Acknowledgements

I wish to acknowledge those without whom this thesis would not have been possible. First, I wish to thank two of my idols in the scientific community: Mr. Bill Nye, your love of science is infectious. And Dr. Emmett Brown, your passion for discovery has given me great inspiration, although, it's a "gigawatt", not "jigawatt" – hard "G" sound. Honest mistake. In addition, I wish to thank WALL-E, who is an enormous inspiration for any designer of a material retrieval system.

Thanks as well to my family: Mom, you held me to the very highest expectations and never accepted anything but my best. Dad, you taught me that hard work is not a process, it's a goal. My brother Eric, you set the bar high, but have encouraged me throughout my whole life. My sister Cheryl, you are stronger than anyone I know, and that strength has always inspired me when times get tough. My sister Danielle, you've made a career out of your compassion, and I only ever hope to be half as selfless as you. And my entire family, in-laws, nieces and nephews, aunts, uncles, cousins and grandparents, the love and support you show is more than any man deserves. I am truly blessed.

I must thank my advisor Dr. K for graciously guiding me back on track countless times, and my colleagues in the Unmanned Systems Lab for making what would have been an overwhelmingly stressful graduate school experience lighthearted and fun. All photographs in this thesis are property of the Unmanned Systems Laboratory at Virginia Tech.

And to whom I will never be able to thank enough: my wife Maggie, for welcoming me home every day with a warm meal and a warm hug. You make me laugh and you give me a reason. Without you, I would never have survived this place. I love you.

Finally, and greatest of all, I thank my God in Heaven. This world is a gift, and we are owed nothing. The majesty of His creation is beyond comprehension, yet we are called to learn, discover, and explore it. It seems everything I learn about this world gives me still another reason to love Him more.

Contents

List of Figures

List of Tables

Nomenclature

Acronyms:	GSR	Ground Sampling Robot
	UAV	Unmanned Aerial Vehicle
Symbols:	A	orifice area
	Ar	Archimedes Number
	C	discharge coefficient
	C_v	flow coefficient
	c	sonic velocity
	D	diameter of height of flow channel
	D_{50}	diameter of height of 50mm flow channel
	d	orifice diameter
	d_p	particle diameter
	g	acceleration due to gravity
	H	pressure vessel head height
	k	specific heat ratio
	M	molecular weight of fluid
	m	mass of fluid
	$\dot{m}$	mass flow rate of fluid
	P	air supply pressure
	P_{atm}	atmospheric pressure
	P_i	initial air supply pressure
	Q	volumetric flow rate
	Q_j	jet volumetric flow rate
	Q_{sf}	volumetric flow rate or secondary fluid
	R	pressure vessel head radius
	Re	Reynolds Number
	Re_p	particle Reynolds Number
	Re_p^*	modified particle Reynolds Number, adjusted for any channel size

R_g	gas constant
r^*	critical pressure ratio
r	radial distance from jet centerline
T	fluid temperature
T_i	initial fluid temperature
t	time
t_w	pressure vessel wall thickness
U	fluid velocity
U^*	critical velocity, gas velocity at which the particle is entrained
U_{avg}	average air velocity
U_c	centerline fluid velocity
U_j	fluid velocity at jet exit
V_s	air supply volume
x	distance in streamwise direction
Z	compressibility factor
α	angle of attack
α_p	tractive force coefficient
θ	array angle
μ	fluid viscosity
ρ	fluid density
$\bar{\rho}$	ratio of air density at jet exit to atmospheric air density
ρ_p	particle density
σ'	von Mises stress
σ_h	hoop stress
σ_l	longitudinal stress
τ_w	bed shear stress

Chapter 1

Introduction

The field of unmanned material sampling presents new and increasingly difficult engineering challenges that require foresight and innovative design in order to produce solutions to problems operators may encounter in the field. The Unmanned Systems Laboratory at Virginia Tech has been tasked with designing the equipment for an unmanned material sampling mission. The lab is developing an unmanned aerial vehicle (UAV) deployable ground sampling robot (GSR) to navigate harsh, rugged terrain leftover from an explosion or natural disaster and collect material from the site for analysis at a remote location. It is the purpose of this thesis to present the design of a pneumatic particulate collection system that the GSR will use for said material collection.

Vacuum samplers have been explored as a possible design for particulate collection where an impeller is used to create suction that lifts particulate into a collection cup. However, because weight and power consumption are limiting factors in lightweight robotic applications, the goal

of this thesis is to present the novel alternative of a pneumatic system, where the energy of compressed air replaces costly electrical energy used to power a motor in a vacuum sampler.

The sections following in this chapter will present the material sampling mission background and mission specific challenges.

1.1 Mission Background

The UAV to be used in the mission is a Yahama RMAX helicopter, seen in Figure 1.1. Modifications to the helicopter necessary to carry out the mission have been made, such as the addition of a TASE camera for navigation and an interchangeable payload system within the landing gear.

Figure 1.1: Virginia Tech's RMAX Helipcopter

The mission is organized into three subtasks needed to collect the necessary information about the event being investigated: aerial data collection, 3-D terrain mapping, and ground data collection. Interchangeable payload pods are attached to the UAV for each of these three subtasks. The aerial data collection is the initial deployment of the UAV with sensors that will

collect data to identify areas of interest on the ground for further investigation by robot deployment. The 3-D terrain mapping utilizes a stereo-vision system to provide information for robot path planning, such as potential hazards or nontraversable terrain. Finally, the ground data collection entails the deployment of the UAV with the GSR. The UAV will hover at 40m and lower the robot via a tether-winch system. It will remain in a hover while the robot is operated from a remote ground station with the tether still attached and is navigated to a point where debris samples of interest and accessibility can be collected. The robot is then retracted part-way back up to the UAV and is returned to the ground station. The entire system architecture is laid out in Figure 1.2.

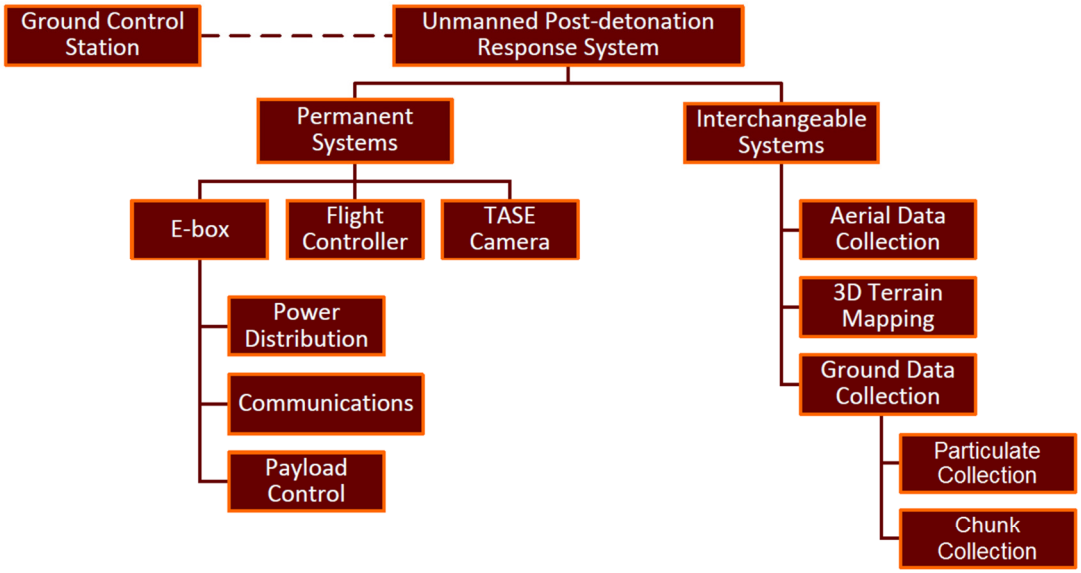

Figure 1.2: System Architecture

The mission calls for collection of ground debris in both chunk and particulate form. Thus, the GSR is designed with interchangeable payloads as well. One version of the robot will have a chunk sampling system onboard, while another will have a particulate sampling system onboard.

The two sampling systems are very different both in objective and operation, and have only the size, weight, and power constraints in common.

The mobility platform of the ground robot on which the sampling system will be used is in Figure 1.3. It is a simple tracked design that sits low to the ground, utilizing space well by allowing for the area within the treads to be used for battery storage and employing lightweight materials and design features[1].

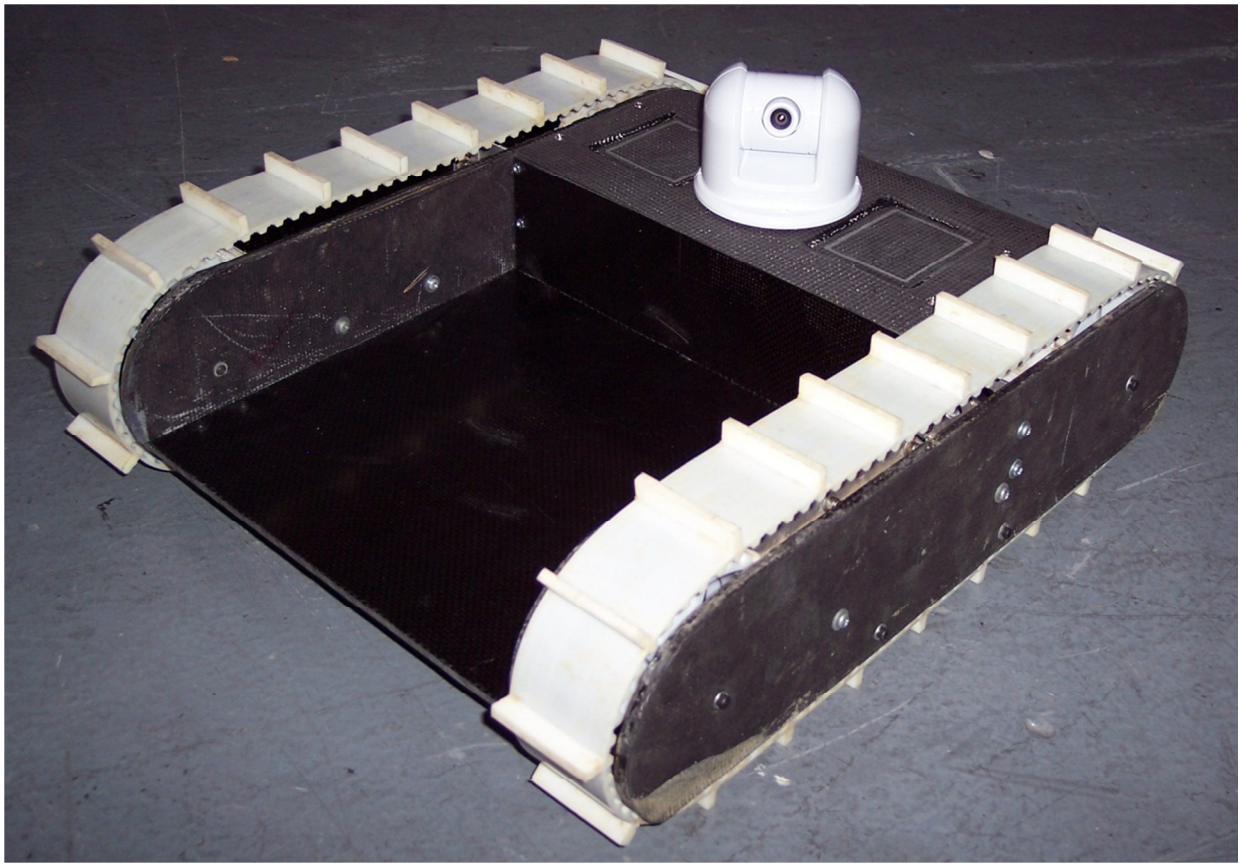

Figure 1.3: Ground Sampling Robot Mobility Platform

Figure 1.4 is a diagram of the key features of the GSR mobility platform onboard which the sampling system will be installed. It was designed to be especially light weight, with the majority of its components fabricated from either carbon fiber or rapid-prototyped polycarbonate. The bulk of the space on the robot is allocated for the implementation of

interchangeable sampling systems to accomplish either the chunk or the particulate sampling. This payload tray directly provides the spatial constraints of the sampler design, which will be discussed in the following section.

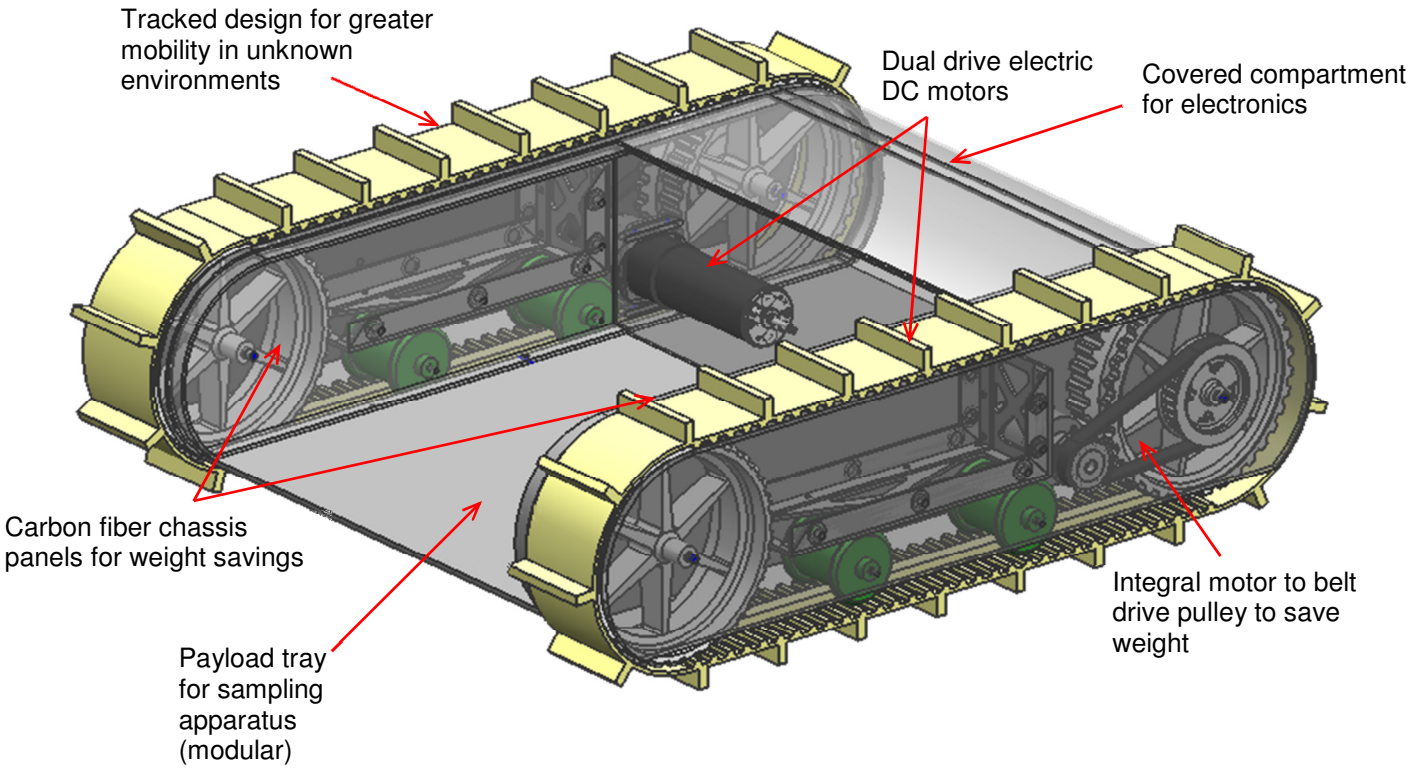

Figure 1.4: Mobility Platform Features

1.2 Challenges and Constraints

Because of the immense challenge that goes along with operating an unmanned vehicle beyond-line-of-sight and with limited system feedback, the particulate collection system must be designed with the utmost simplicity to reduce the possibility of mechanical / electrical malfunction or human error. Additionally, the size and weight constraints of the system are dictated by the UAV's payload capacities. In general, great effort was made to reduce the

system complexity while still maintaining the level of performance necessary for mission success.

The design goal was to develop a system that would collect 50cc of particulate material in a controlled testing environment, keeping in mind that only the top 5/8" thick layer of particulate is desired. While volumetric measurements of the material collected make it easier to compare the pneumatic sampler design with other designs, much of the testing in this thesis will evaluate sampling performance based on the mass of the material collected because sample density will affect the quality of the sample.

The UAV's modular payloads (pods) allow for smooth transitions between the different mission subtasks. The robot then must be contained within a pod that can be easily attached to the UAV by mounting it within the landing gear. Therefore, the pod must be able to fit within the landing gear, the robot must be able to fit within the pod, and the sampler must be able to fit onboard the robot; essentially, the UAV determines the size constraints of the sampler design.

Figure 1.5 illustrates the dimensions of the constraint envelope of the sampling system, seen in the figure as a blue rectangular prism. The constraint envelope is the available space onboard the mobility platform for implementation of the sampling system. Note that the sampling system will be allowed to protrude above the height of the robot, so long as it is contained within the robot pod. The payload tray of the robot provides a 10.5" × 10.5" × 5.5" available space.

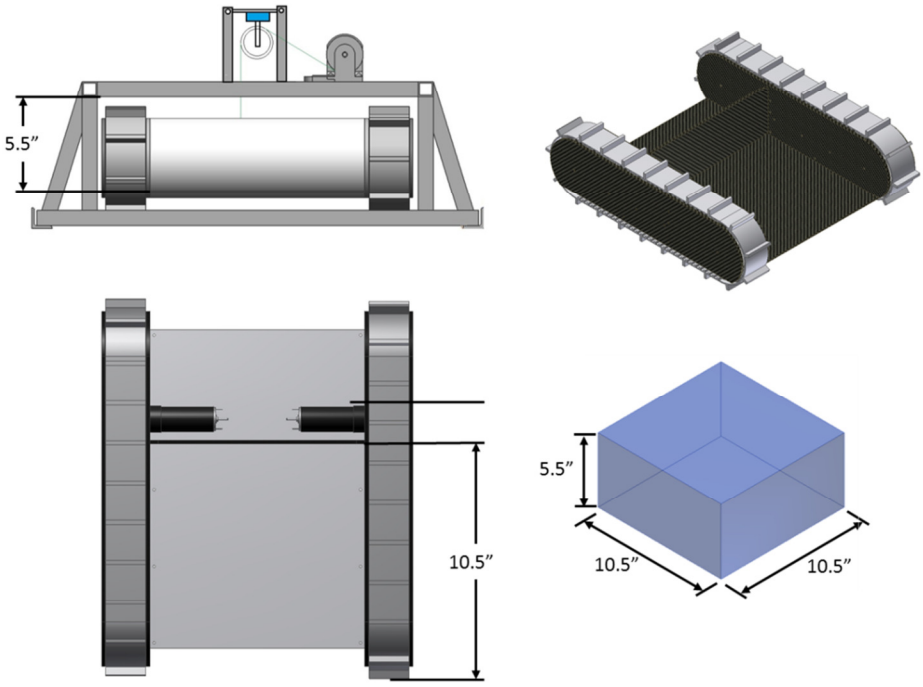

Figure 1.5: Constraint Envelope

In addition to the spatial constraints placed on the system, weight is a limiting factor as well because the RMAX's maximum payload is 48 lbs. A target design weight for the robot was determined to be 17.6 lbs after considering the weights of other onboard systems that will be added to the RMAX for this mission, i.e. vision systems, communication systems, etc[1]. In order to determine how much of the 17.6 lbs for the GSR is to be allocated to the sampling system, one must first consider the weight estimates for other necessary subsystems onboard the robot presented in Table 1.1.

Table 1.1: Ground Robot Component Weight Estimates

Item	Quantity	Unit Weight *(lb)*	Weight total *(lb)*
Mobility Platform	1	9.81	9.81
Radio	1	0.53	0.53
Batteries	2	0.73	1.46
Camera (w/ pan-tilt)	1	0.62	0.62
		Total:	12.42

Based on these estimates and the target design weight, the maximum allowable weight for a sampling system onboard is approximately 5.2 lbs. The spatial and weight constraints for the sampling system are summarized in Table 1.2.

Table 1.2: Sampling System Dimensional Constraints

Dimensional Constraints	
Max Length	10.5 in
Max Width	10.5 in
Max Height	5.5 in
Max Weight	5.2 lbs

Although an advantage of a pneumatic system is a significant decrease in electrical power consumption, some will be needed to actuate the release of the air and to move the sampler into contact with the ground when a sample is ready to be collected. The robot uses two Thunder Power 14.8V Lithium Polymer (LiPo) battery packs mounted inside the tracks as its onboard power source.

Chapter 2

Literature Review

The work contained within this thesis is unique; it combines an empirically based investigation of gaseous-solid flow with a direct application to unmanned material sampling. There is little that has been published on pneumatic particulate sampling, but findings from research in fields like sediment transport in riverbeds or sand dune erosion can be of use in understanding the logic behind the design to be presented. This chapter highlights some of the most relevant research already conducted as a means of providing a sufficient background to the theories used in the pneumatic sampler design.

2.1 Modeling of Particulate Transport

For our purposes the phenomenon of particulate transport can essentially be divided into two phases: incipient motion and saltation. The former is, as expected, the phase where particles just begin to break free from their sedentary state, while the latter refers to the phase in which particles are already suspended in a fluid. This section will give an overview of the force

balance approach to particulate transport modeling, and then will proceed to discuss each of these two phases in more detail.

2.2 Force Balance Overview

Newton's second law of motion can be used in our small scale application to understand the motion of an individual particle through a fluid. A particle is under the influence of a collection of forces that dictate its movement or lack thereof at all times. To date, the vast majority of work on particulate motion has involved trying to identify these forces on a single particle. Coleman and Nikora[2], for example, conducted a theoretical study on particle entrainment covering the particle scale all the way up to the larger stream reach scale. Recognizing that en masse movement is most applicable for the majority of engineering applications, they combined force balances with fluid and particle momentum equations, though realizing that a fuller understanding first stems from the particle scale. Even in the widely recognized work of Shields[3] in which en masse movement of bed-load in rivers was the topic of study, single particle force balances were used. Consider the equation Shields presents as the bed shear stress, or the force needed to entrain a particle, τ_w,

$$\tau_w = \alpha_p(\rho_p - \rho)gd_p \qquad \textbf{2.1}$$

where α_p is the tractive force coefficient, ρ_p and ρ are the particle and fluid densities, respectively, g is the acceleration due to gravity, and d_p is the particle diameter. The expression $(\rho_p - \rho)gd$ is essential the particle weight, and so one can see how this equation is a very basic force balance.

From Equation 2.1 it can be observed that the magnitude of a force needed to lift a particle, τ_0, is dependent upon properties of both the particle and the fluid. However, the tractive force coefficient is a parameter that is best determined experimentally for a particular particle bed due to the unpredictability resulting from the way in which particles lay in a bed at a given point.

Phillips[4] simplifies particle entrainment to a four term force balance, and although his work focused on incipient motion of various particle sizes, the equation also holds for saltation[1] as some forces cease to exist or become dominated by others. Equation 2.2 is the four term force balance with which Phillips was mainly concerned.

$$F_a + F_b = F_c \text{ or } F_d. \qquad \textbf{2.2}$$

Here, F_a represents the total adhesion and cohesion, the interparticle attraction due in one way or another to van der Waals' forces. F_b is the buoyancy-corrected net particle weight. F_c is the force due to an "updraft beneath a burst," a force characteristic of particles small enough to lie completely submerged in the viscous sub-layer of the flow. On the other hand, F_d is the force acting on particles that protrude into the inviscid core of a turbulent flow; it is the drag force due to the flowing fluid.

2.2.1 Incipient motion

The way in which particles lay in a bed of other particles is highly unquantifiable. Typically, smaller particles like dust and sand granules have highly irregular shapes. Although efforts could be made to measure the sphericity of particles, and in that way account for their

[1] Saltation refers to the state in which particles are suspended in the transporting fluid. Typically, when a particle is bouncing along a particle bed, it is considered in a state of saltation.

deviation from what one would expect the resistance of a sphere to an engulfing fluid would be, one would still be left with the random surface geometry of the particle bed as a whole, which results from the jagged shape of the particles. Because of this chaotic bed surface and because of the haphazard particle shapes, Fletcher[5] points out that no true velocity threshold exists for entrainment of a particular particle size. This observation has led most researchers to tackle this problem experimentally. Fletcher himself conducted wind tunnel testing on a variety of particle materials, as did Kalman et al[6]. Because their testing was conducted on a scale so close to the application for this thesis, the work of Kalman et al will be discussed in more detail later and even utilized for the direct determination of certain aspects of the sampler design.

The number or particles entrained in a flow can be viewed as a property of the bed[2]. To understand this, one must reconsider Equation 2.2. The bed properties dictate three of the four terms in some way. F_a is clearly dictated by the bed properties because it is an expression of the interparticle forces. F_c and F_d also depend on the bed properties in that they depend on how far into the flow a particle protrudes.

Phillips uses the force balance equation for three different regimes presented in Table 2.1 and Figure 2.1. The downward slope in Figure 2.1 represents the large particle regime, the flat region represents the intermediate regime, and the upward slop at the end represents the large particle regime.

Table 2.1: Phillips' Particle Regimes

Regime	Particle Diameter	Force Balance
Large particle	$d_p > 200\ \mu$m	$F_b = F_d$
Intermediate	$30\ \mu\text{m} < d_p < 200\ \mu$m	$F_b = F_c$
Small Particle	$d_p < 30\ \mu$m	$F_a = F_c$

Upon studying Phillips' results, one can see that large forces are needed to free extremely small particles because, in the case of smaller particles, adhesive and cohesive forces dominate. On the other extreme, large forces are needed to entrain large particles because, as one would have expected, in the case of larger particles, gravitational forces dominate.

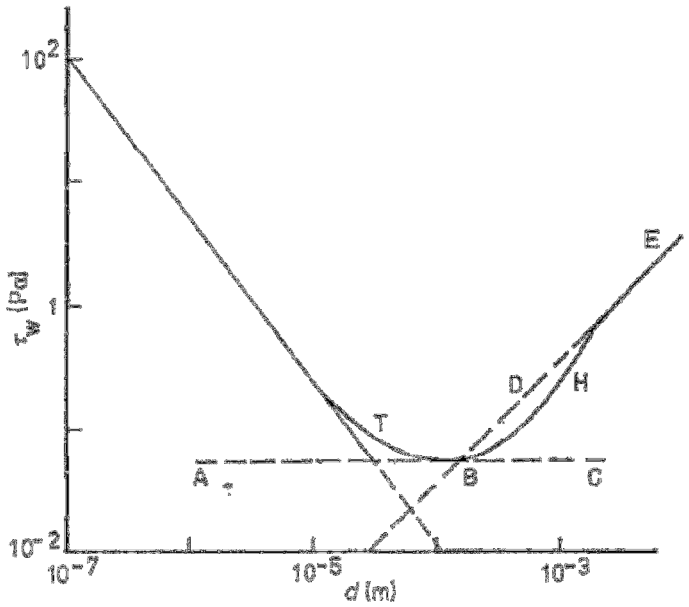

Figure 2.1: The wall shear stress $\boldsymbol{\tau_w}$ required to entrain a particle of diameter $\boldsymbol{d}$ into air [4].
Used by permission of IOP.

2.2.2 Saltation

Once the particle is set into motion along the bed, it will inevitably impact the bed such that it will bounce high—often several hundred grain diameters high—and will enter the air stream, thus entering the saltation phase[7]. When the particle is freed from the particle bed and enters the air stream, its streamwise velocity will increase because the air stream will enact a force on the particle, fighting against the drag force, until the particle's velocity reaches that of the air. However, at the same time, the particle will be falling to the ground due to the

dominating force of gravity, which also fights against the drag force[7]. Along with the initial velocity, these forces determine the particle's trajectory as shown in Figure 2.2. The particle's vertical velocity will go to zero when the particle eventually hits the ground, and it's streamwise velocity will also go to zero, though in reality there may be some bouncing and rolling due to momentum. Then, the particle will once again be subject to the forces discussed in the section on incipient motion.

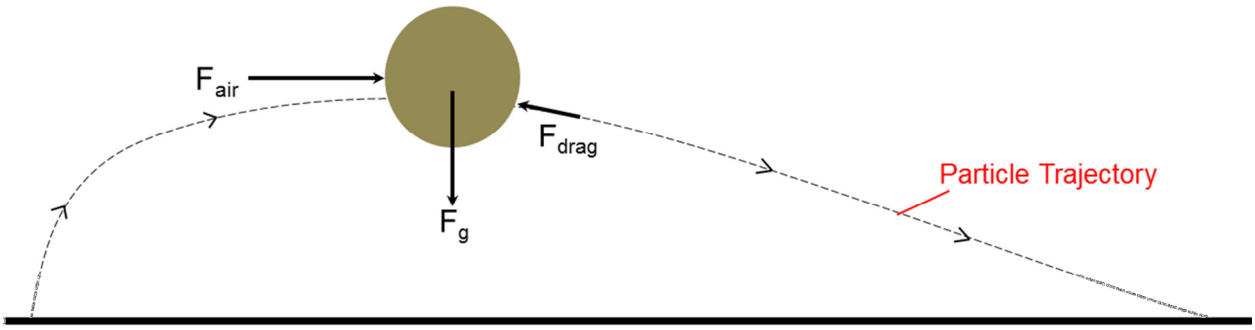

Figure 2.2: Saltation Force Balance

If the particle is being carried by the air stream and the air velocity suddenly goes to zero, the particle will have some streamwise momentum to carry it a little farther in that direction, but its streamwise travel has essentially ended, and the particle will begin falling to the ground acted upon only by gravity and the drag force.

The concept of saltation will become important especially when the pulse method is discussed. The pulse method is the intermittent release of air through the sampler in order to make the most efficient use of the limited amount of compressed air there is in the supply.

2.3 Sampler Cavity Design

The findings of this literature review greatly influenced key aspects of the final design. Much consideration was given to the sampling cavity of the particulate collection sample and how its geometry affects the flow of the air through it. The sampling cavity is the section of the final sampler design that actually makes contact with the debris to be collected. In this section, there will be a both a brief discussion of the work of Kalman et al, which presents a formula for predicting particle pick-up velocities, and an introduction to the Coanda Effect which was given consideration in the ramp design of the sampler.

2.3.1 Critical Velocities

The velocity of the air that entrains the particles is in part a function of the layout of the channel through which the air flows. Therefore, in order to achieve the velocity needed to collect enough particulate debris, the air channels in the sampler cavity had to be designed appropriately. With the velocity too high, the system wastes valuable energy, or more specifically, valuable air, and risks particle attrition[8]. If the particles are made too small from excessive impact forces during the sampling process, then fewer particles will be filtered in the systems exhaust ports, and the amount of material sampled is potentially decreased.

Kalman et al conducted a thorough experimental investigation of the critical particle velocities, the velocity of the gas flowing over a bed of particles at which particles begin to be picked up. In their study, a correlation is found between the particle's Archimedes number and its Reynolds number. Just as the Reynolds number represents the ratio of inertial forces to viscous forces associated with the particle, the Archimedes number, which describes fluid

motion resulting from differences in density, is the ratio of the gravitational forces to viscous forces. The Archimedes number and Reynolds number are defined as

$$\mathrm{Ar} = \frac{g\rho(\rho_p - \rho){d_p}^3}{\mu^2} \quad \textbf{2.3}$$

$$\mathrm{Re}_p = \frac{\rho U^* d_p}{\mu} \quad \textbf{2.4}$$

where U^* is the critical velocity for the particle, and μ is the fluid dynamic viscosity.

Kalman et al experimentally developed the following piece-wise function to relate the Archimedes and Reynolds numbers.

$$\mathrm{Re}_p^* = 5\mathrm{Ar}^{3/7} \text{ for } \mathrm{Ar} > 16.5 \quad \textbf{2.5}$$

$$\mathrm{Re}_p^* = 16.7 \text{ for } 0.45 < \mathrm{Ar} < 16.5 \quad \textbf{2.6}$$

$$\mathrm{Re}_p^* = 21.8\mathrm{Ar}^{1/3} \text{ for } \mathrm{Ar} < 0.45 \quad \textbf{2.7}$$

In their study, the Reynolds number is characteristic of a channel 50mm tall, so an asterisk is used to indicate a Reynolds number modified for use in any size flow channel. That is, Kalman et al have put forth the following modified Reynolds in order to use their correlations regardless of channel size,

$$\mathrm{Re}_p^* = \frac{\rho U^* d_p}{\mu\left(1.4 - 0.8e^{\frac{-D/D_{50}}{1.5}}\right)} \quad \textbf{2.8}$$

where D is the diameter or height of the flow channel, and the subscript 50 denotes that of a 50mm pipe or flow channel.

Thus, if Ar is known for a particular size particle, then one can calculate the velocity of air needed to pick that particle up by extracting it from the equation for the modified Reynolds number. These equations will be applied later to the particles used in this study in a discussion of the free jet used in the final sampler design.

2.3.2 The Coanda Effect

Discovered accidentally in 1910 by a Romanian engineer for whom it is named, the Coanda Effect causes fluid streams to cling to nearby surfaces[9]. It is most famously used in aircraft applications to maximize the amount of lift generated from air passing over an air foil, but a significant use has been found for it as a design feature in the pneumatic particulate sampler which will be discussed in future chapters.

When a jet of air races past a surface, a low pressure zone is created between the jet and the surface. The ambient air cannot fill the low pressure zone because the jet creates a fluid barrier, and so the low pressure zone collapses causing the jet to attach to the surface. The adhesion is strong enough that the jet will even follow the surface around bends. Figure 2.3 illustrates this phenomenon on a curved surface.

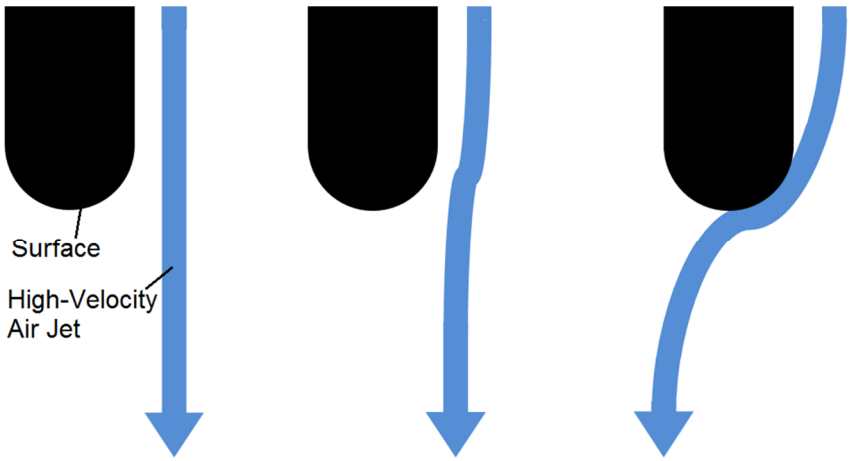

Figure 2.3: The Coanda Effect

Chapter 3

Air Supply Volume-Pressure Analysis

The pneumatic sampler uses the kinetic energy from the release of a volume of compressed air to transport the particulate into the collection area. That supply of compressed air is to be kept on the sampling robot along with the sampler itself, and since available space onboard the robot is limited, measures needed to be taken to ensure that the air supply was neither too large that it could not be contained within the constraint envelope, nor too small that there would not be enough air to entrain a sufficient amount of particulate.

In this chapter, the issue of the change in pressure over time, or the pressure transient, will be covered along with onboard considerations for the tank itself.

3.1 Pressure Transient

The flow through the air channels in the pneumatic sampler is driven by the pressure differential between the air supply and the atmosphere. As the air is released from the supply by the actuation of a set of valves, the tank will empty and the supply pressure will drop. Because

the supply is small, the drop in pressure over time is significant enough to warrant consideration of its effect on the flow.

3.1.1 Pressure Transient Model

When air is released from a pressurized volume, choked flow occurs at the outlet as long as the ratio of downstream pressure to upstream, or supply, pressure is less than the critical pressure ratio, r^*,[9]

$$r^* = \left(\frac{2}{k+1}\right)^{\frac{k}{k-1}} \quad \textbf{3.1}$$

where k is the specific heat ratio of the gas. For air, k=1.4, and thus the critical pressure ratio is 0.528.

If the downstream pressure is less than 52.8% of the supply pressure, then the flow is choked and the gas velocity is equal to the speed of sound. However, increasing the supply pressure beyond that point will have no effect on the velocity, but will still increase the mass flow rate. Because the mass flow rate is equal to the product of the velocity, the cross-sectional area of the flow, and the gas density, constant velocity with increasing mass flow rate means that the density will increase with the flow rate once critical (or choked) flow has been achieved.

Rasouli and Williams introduce a method for finding the pressure transient of an accidental release of methane gas from a pressurized storage container for the purposes of contaminant dispersion modeling[10]. Since their application deals with high upstream pressures, their model had to account for choked flow. Though their work did contain some errors, the theory was correct, and so an amended derivation is presented in 0, and the

generalized form for calculating the drop in pressure over time as air is released from a supply volume into the atmosphere is given in the following first order nonlinear differential equation,

$$P(t)^{\frac{1-3k}{2k}} \cdot \frac{dP}{dt} = \frac{CA}{V_s}\sqrt{\frac{k^3 R_g T_i P_i^{\frac{1-k}{k}}}{M}\left(\frac{2}{k+1}\right)^{\frac{k+1}{k-1}}} \qquad \textbf{3.2}$$

where P is the supply pressure expressed as a function of time, t, C is the discharge coefficient, A is the area of the supply outlet, V_s is the supply volume, R_g is the gas constant, T_i and P_i are the initial gas temperature and pressure, respectively, and M is the molecular weight of the gas.

As is outlined in Appendix A, this equation was generated by combining the ideal gas law and the equation for isentropic expansion of an ideal gas, solving for the mass of the gas, differentiating with respect to time to find the flow rate, and setting the resulting expression equal to the flow rate of the critical flow equation. The critical flow equation expresses the mass flow rate, $\dot{m}(t)$, as

$$\dot{m}(t) = CAP^{\frac{k+1}{2k}}\sqrt{\frac{kM}{R_g T_i P_i^{\frac{1-k}{k}}}\left(\frac{2}{k+1}\right)^{\frac{k+1}{k-1}}} \qquad \textbf{3.3}$$

when the fluid density has been eliminated from the equation.

3.1.2 Pressure Transient Application Simulation

In order to ensure that selected dimensions of the onboard air supply for the pneumatic particulate sampler would provide enough air at a high enough pressure for sufficient particle entrainment, the mass flow rate and pressure transient were simulated in MATLAB; the MATLAB script is provided in Appendix C. The parameters used in the simulation are summarized in Table 3.1 and are characteristic of the current application. The results are plotted

in Figure 3.1 and Figure 3.2 for an array of outlet orifice diameters from 1.0-4.0 mm, accounting for a design of five circular outlets.

Table 3.1: Pressure Tranisent Simulation Parameters

Variable	Definition	Value	Units
C	Discharge Coefficient	0.60	
V_s	Supply Volume, $\left(\frac{\pi}{4}d^2L\right)$	77	in^3
L	Length	8.0	in
d	Diameter	3.5	in
k	Specific Heat Ratio	1.4	
M	Gas Molecular Mass	28.966	$\frac{\text{kg}}{\text{kmol}}$
R_g	Gas Constant	8,314.5	$\frac{\text{N}\cdot\text{m}}{\text{kmol}\cdot\text{K}}$
T_i	Initial Gas Temperature	296	K
P_i	Initial Supply Pressure	125	Psi

Because the "nozzles" used in the pneumatic sampler design are actually machined as simple, square-edged orifices, the discharge coefficient is 0.60. The gas properties used are typical of air, and the initial supply pressure was selected from the results of the experimental testing covered in Chapter 4. The supply tank length and diameter were determined given the spatial constraints discussed in Section 1.2.

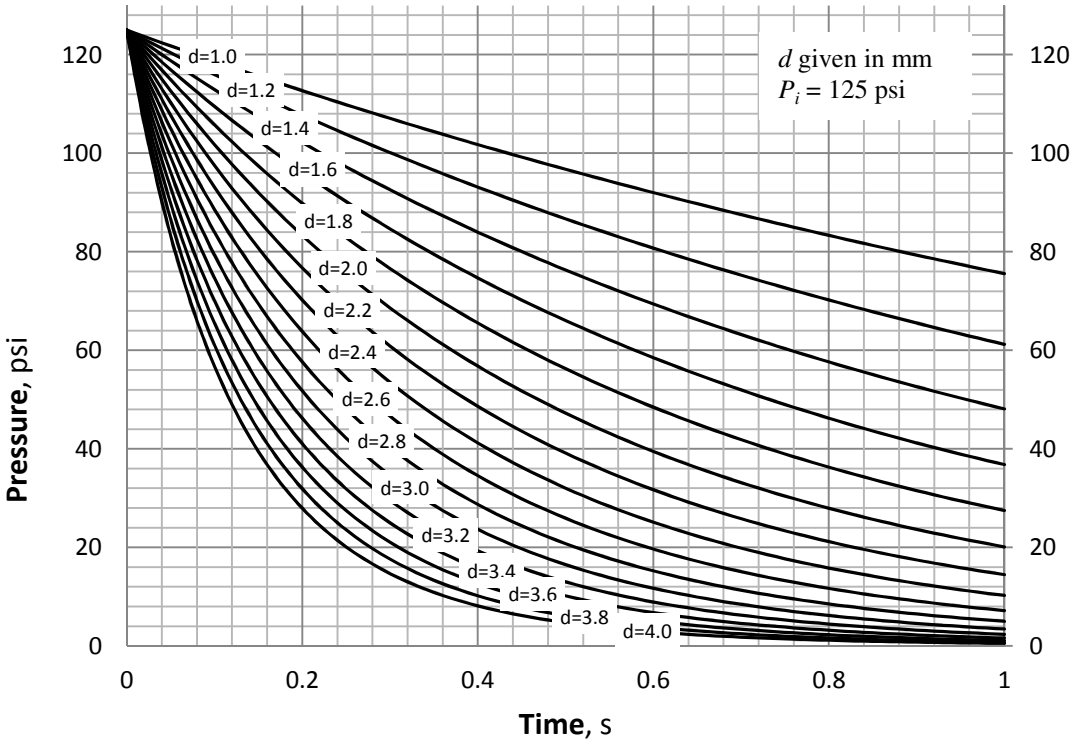

Figure 3.1: Pressure Transients for Different Orifice Diameters

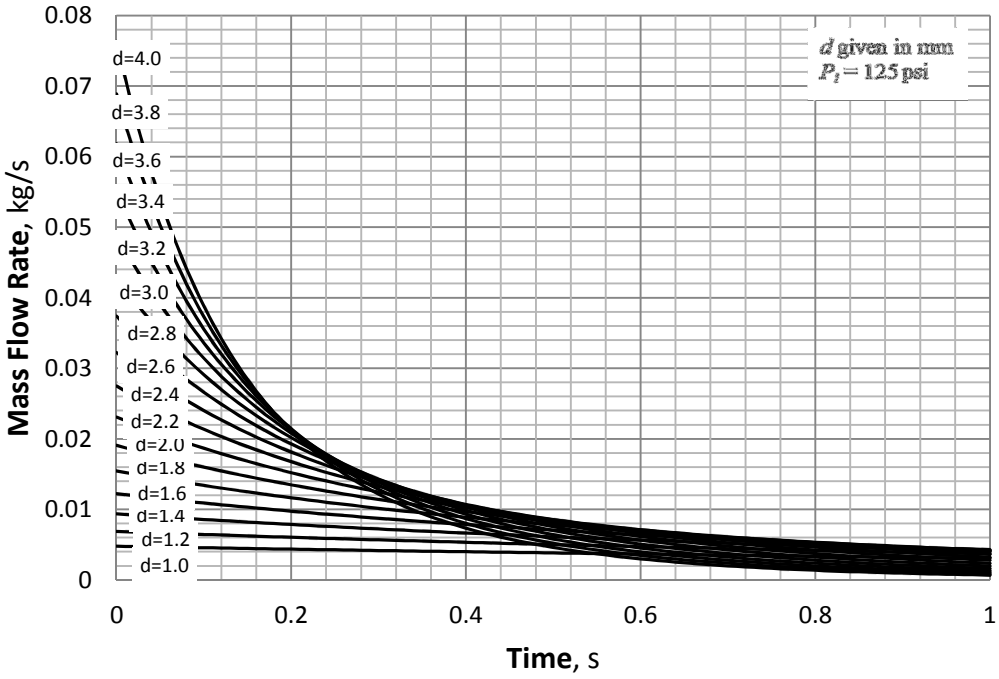

Figure 3.2: Mass Flow Rates for Different Orifice Diameters

Figure 3.1 shows the expected loss in pressure as time elapses for a total of one second of flow time. As the orifice diameter decreases, the pressure transient is less drastic—to the point that it seems almost linear for the short one second time frame. Figure 3.2 is an interesting plot that shows how larger outlet orifices can end in smaller flow rates than smaller outlet orifices despite their large initial flow rates.

In Figure 3.3 the drop in pressure after 1.0 second of air release is presented as a function of the outlet orifice diameter for various initial pressures. As would be expected, the greater the initial pressure, the greater the pressure drop. This linear relationship can also be seen in Figure D.1. Also, the pressure drops plateau as the outlet diameter increases because the supply empties faster with a larger outlet, and so the final pressures approach zero.

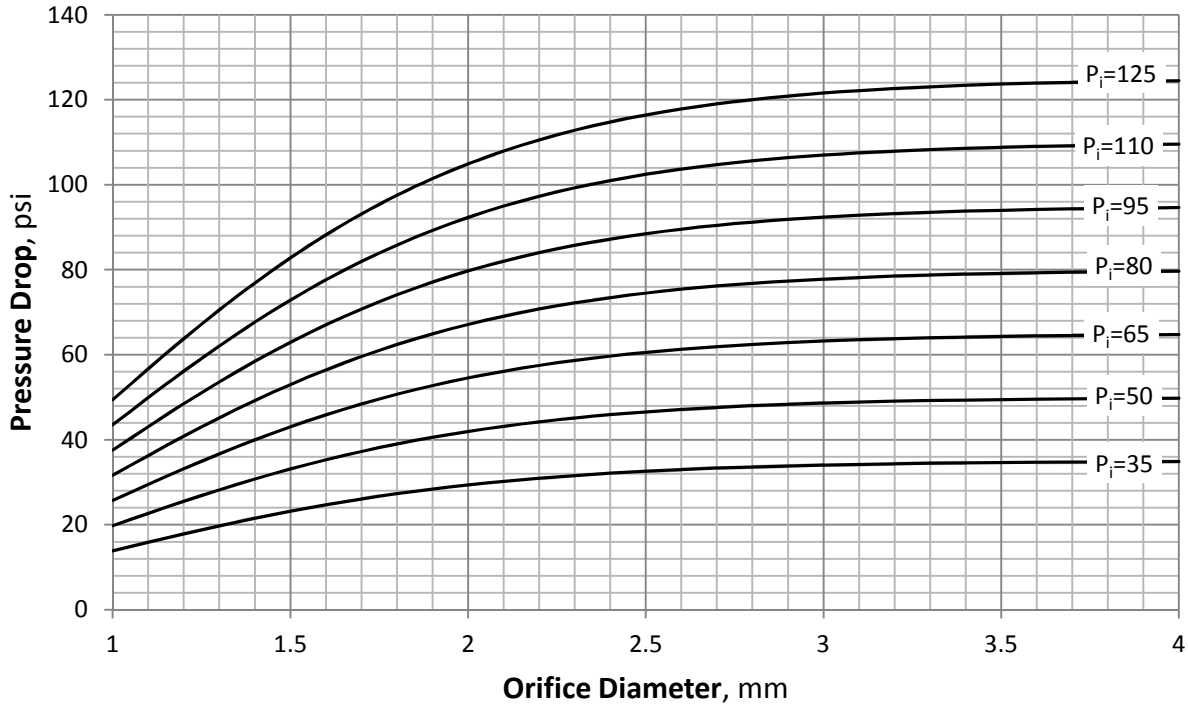

Figure 3.3: Pressure Drop After 1.0 Second of Flow

3.2 Onboard Air Supply

Once a solid understanding of the pressure transient concerns for the onboard air supply has been established, it is necessary to ensure that the final tank design is strong enough to withstand the stresses induced by the required air pressure. Both an existing prototype and final design possibility are covered in this section.

3.2.1 Air Supply Prototype

A prototype air tank, shown in Figure 3.4 was constructed out of Aluminum-6061 to prove the pneumatic sampler design concept. Although the no consideration was given to weight of the tank, the dimensions and internal pressure rating were designed to fit the current application.

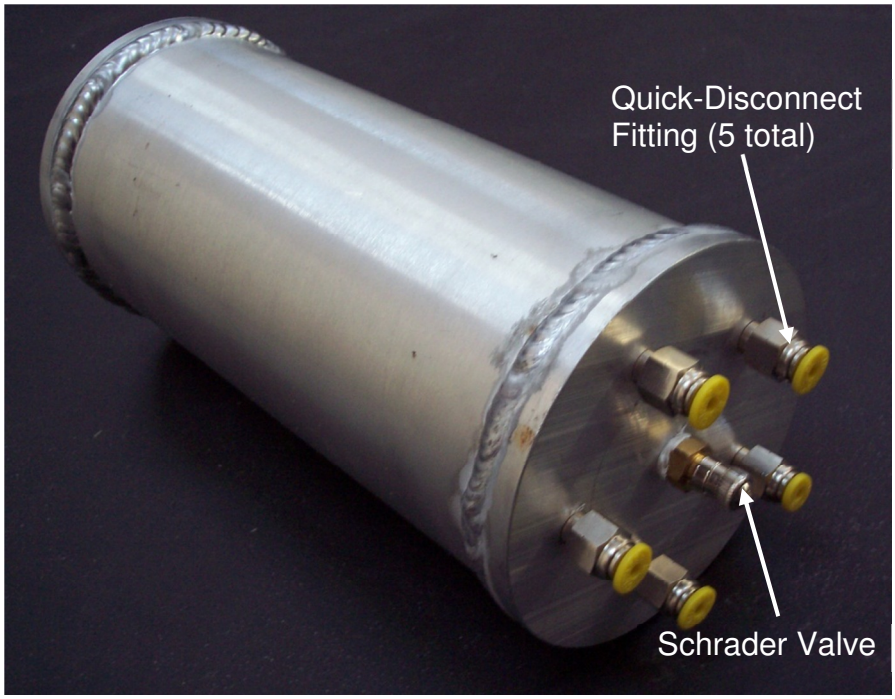

Figure 3.4: Air Supply Prototype

The tank is made of an Aluminum-6061 round tube of 1/8" wall thickness. For ease of manufacturing, the prototype has two flat, circular, ¼" thick Aluminum-6061 heads welded on with lap joints. One of heads has a single 1/8" NPT Schrader valve inlet encompassed by five evenly spaced 10-32 quick-disconnect fitting outlets that accept 1/8" O.D. tubing.

The tank was overdesigned for safety and given a maximum allowable pressure of 155 psi. Once the outlets are connected via flexible tubing to normally-closed valves, the tank can be filled with an air compressor to its capacity of $77in^3$ using the Schrader Valve. Similar to inflating a tire, the pressure is checked intermittently by connecting a pressure gauge to the Schrader valve during the filling process to achieve the desired supply pressure.

When filled to an initial pressure of 120psig (a limit placed upon the system by the valves to be discussed in Chapter 5), the tank has an estimated 2.8s of critical flow and takes roughly 4s to drop below 10psig. The estimates were generated using the MATLAB simulation from Section 3.1 and were validated experimentally using a stopwatch.

The tank fits snuggly in the rear of the constraint envelop in Figure 1.5, leaving ample room for the sampler itself in the front of the robot. While the prototype itself weighs 1.9 lbs, further design iterations could easily bring that weight down significantly.

3.2.2 Final Air Supply Design Recommendations

While convenient for manufacturing purposes, the flat heads on the prototype design ultimately significantly increase the weight of the tank. In order for a design with flat heads to achieve the same allowable pressure as a design with hemispherical or ellipsoidal heads, the head thickness must be greatly increased, thus adding more material and more weight[11]. The trade-

off, of course, is that hemispherical heads are much worse from a spatial efficiency stand-point; increasing the head ratio[1] will decrease the capacity of the air supply, and Figure 3.5 illustrates this point well. Given the square configuration of the robot's mobility platform, the 90° angles of the flat heads fit much more nicely.

The data summarized in Table D.1 and presented graphically in Figure 3.5, Figure 3.6, and Figure 3.7 is from a finite element analysis (FEA) simulation using Autodesk Algor Simulation Professional. To generate a useful comparison of the pressure vessel weights, capacities, and strengths, it was necessary to make some assumptions for the simulation. In this analysis a cylindrical pressure vessel with a constant outside length[2] of 10" and a constant outside diameter of 4.3" is assumed. The length of the supply was fit to the width of the constraint envelope of Section 1.2, and the diameter was fit to the height of the constraint envelope. No outlets were added to the pressure vessel, thus neglecting the effect of stress concentrations at the outlets, in order to better understand the effect of the heads. The supply material was assumed to be Aluminum 6061-T6 with ideal welds, and the internal pressure used in the simulation was 155psi, 30psi greater than the operating pressure[11]. The pressure vessel is a thin-walled structure, but solid brick elements were used to generate the mesh with two divisions along the wall thickness.

[1] The head ratio is defined as the ratio of the radius of the head to its height, R/H.
[2] The length is defined by the apex of the head on the positive side to the apex of the head on the negative side

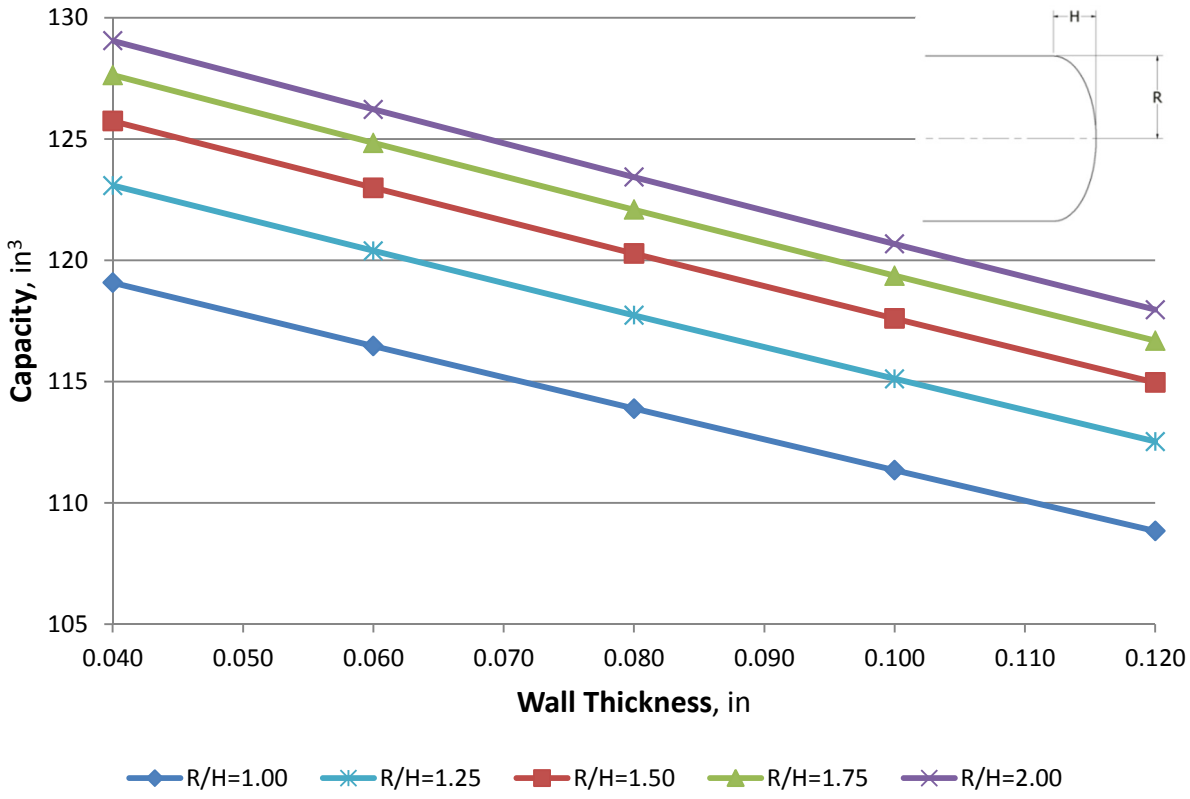

Figure 3.5: Effect of Head Ratio on Supply Capacity

Figure 3.5 shows that there is a very nearly linear relationship between the supply's wall thickness and its volumetric capacity. Note the relationships between the lines representing the different head ratios. As the head ratio is increased, approaching that of a flat head, the increase in supply capacity begins to diminish; while there is a significant increase in supply capacity when increasing the head ratio from 1.00 to 1.25, the benefit from increasing the head ratio from 1.75 to 2.00 is less so.

However, one must also consider the relationship between the air tank weight and strength. As with any pressure vessel, the tank used onboard the robot for the air supply must be designed to be strong enough to withstand internal pressure required for the application.

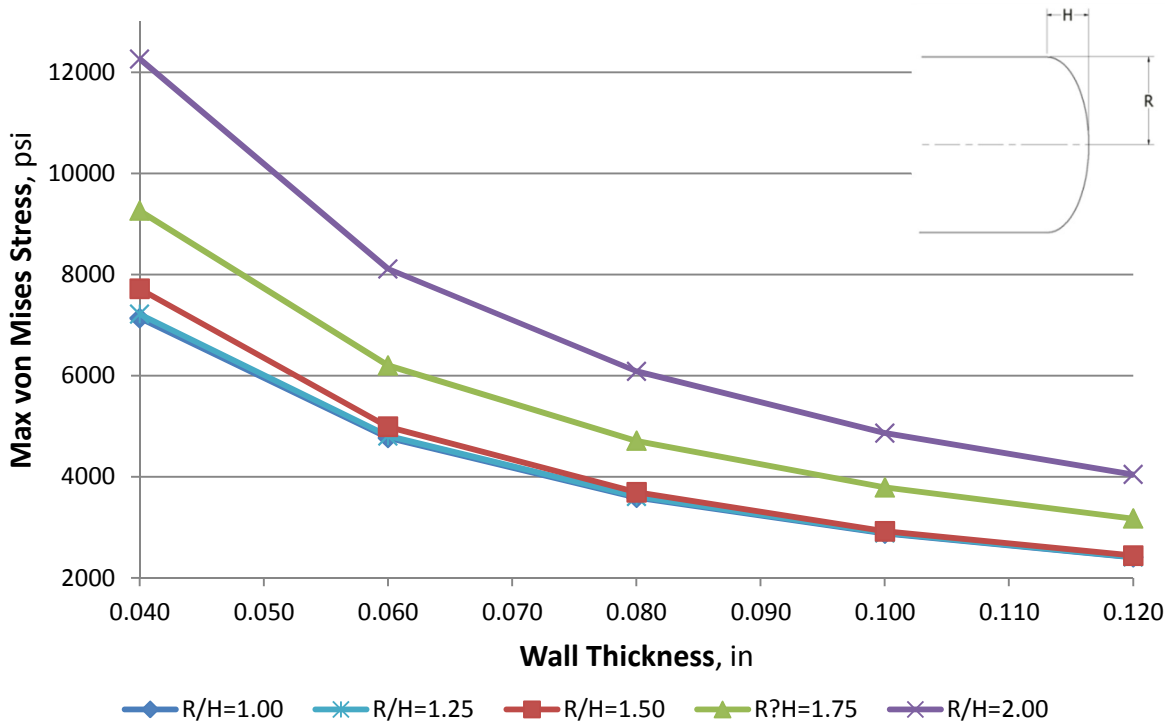

*Outlets were excluded from this simulation to allow for a more accurate comparison of the heads

Figure 3.6: Pressure Vessel Maximum von Mises Stress—Head Comparison

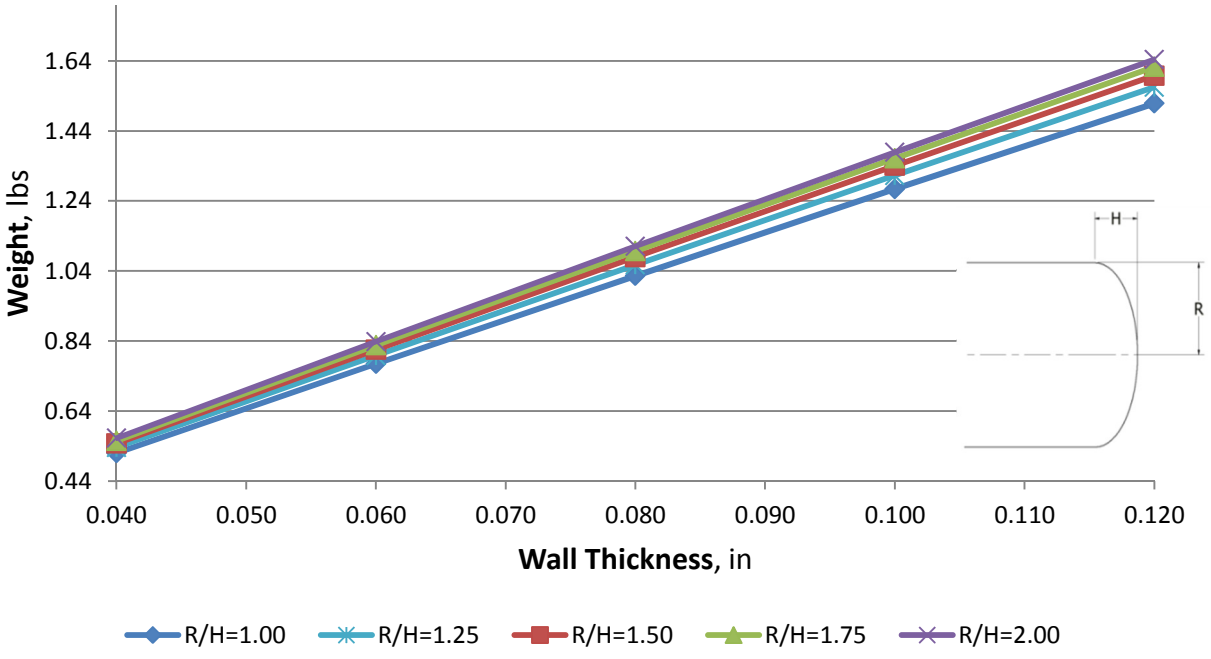

Figure 3.7: Pressure Vessel Weight—Head Comparison

Suppose the yield strength of the material used was 16ksi[1] and a factor of safety of 2 was desired, then the maximum von Mises stress of the tank should be 8ksi. By inspection of Figure 3.6 it is clear that all of the presented head configurations could meet this requirement, although with varying weights and capacities. For example, the ellipsoidal heat with a 2:1 head ratio would provide the largest capacity at 126 in^3, but since its wall thickness must be approximately 0.06" to meet the desired factor of safety, it would weigh 0.84 lbs. On the other hand, the spherical head configuration (R/H=1) could safely have a wall thickness of under 0.04", which corresponds to a 0.52 lb weight—a savings of 0.32 lbs, but the capacity would be only 119 in^3. The 7in^3 decreased air supply corresponds, however, to a mere 2psi increase in pressure drop over one second of total flow time through a 1.2mm orifice diameter, so the trade-off seems worthwhile.

Therefore, spherical heads are the preferred design for an onboard air supply because the significant weight savings justifies the small pressure loss. Although fabricating a pressure vessel with these heads requires more sophisticated fabrication techniques, companies can be found to make custom, lightweight pressure vessels[12].

A recommended air supply design is shown in Figure 3.8, utilizing spherical heads and placing the outlets on the cylinder rather than the heads. With the recommended placement of the outlets, the length of the supply can be expanded to match the width of the robot without having to leave from to attach tubing and fittings. The fittings are the same as the fittings on the air supply prototype.

[1] The actual yield strength for Aluminum 6061-T6 is 40ksi[13].

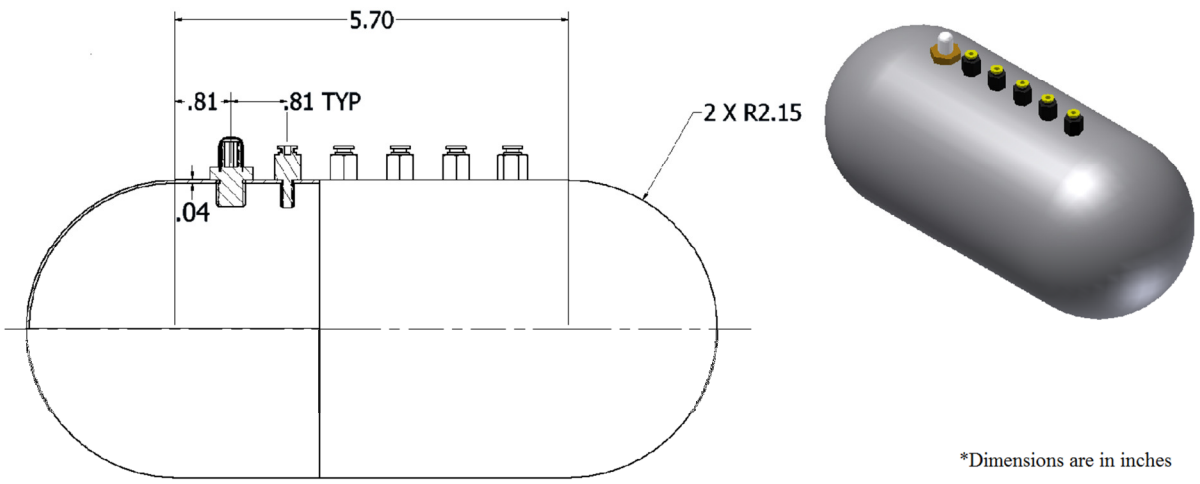

Figure 3.8: Spherical Head Air Supply

Figure 3.9 shows the FEA and where the stresses are concentrated in the pressure vessel. The strongest areas are the heads, while the maximum stress occurs at the outlets. Local mesh control was employed around each outlet to refine the mesh and is shown in the zoom window. Key supply design specifications are outlined in Table 3.2.

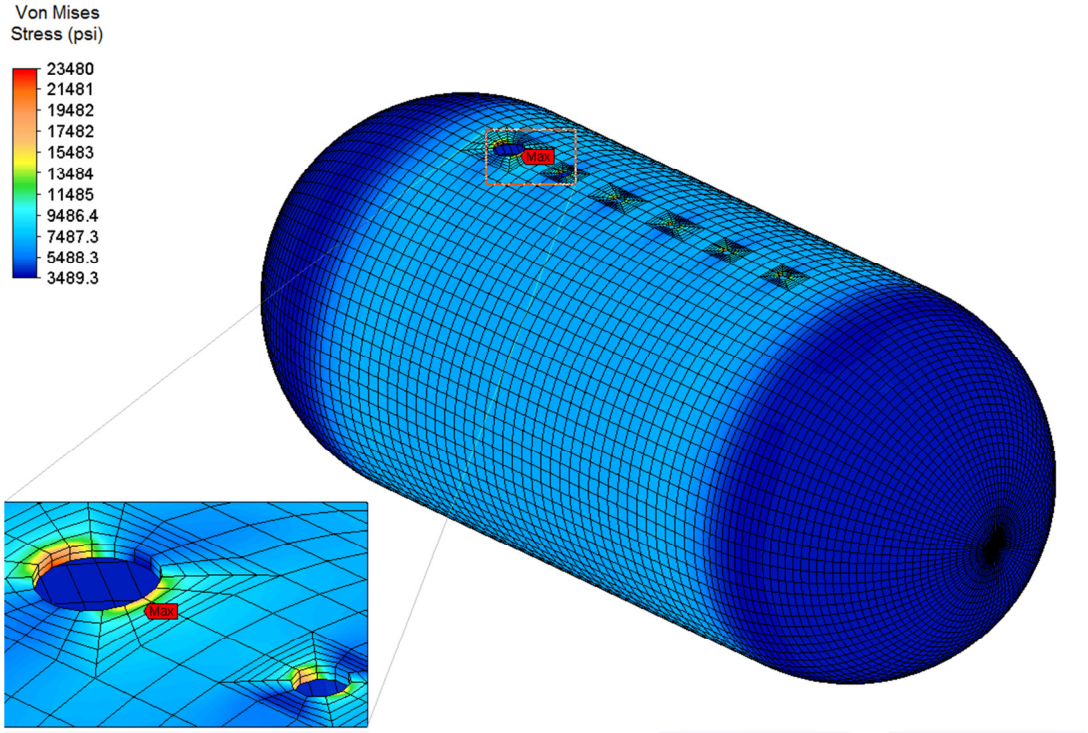

Figure 3.9: Stress Analysis of Spherical Head Pressure Vessel, t_w=0.04”

For validation of this FEA model, a simple thin-walled pressure vessel stress calculation can be performed. The hoop stress, σ_h, and longitudinal stress, σ_l, are given by

$$\sigma_h = \frac{P(D_o - 2t_w)}{2t_w} \quad \textbf{3.4}$$

$$\sigma_l = \frac{P(D_o - 2t_w)}{4t_w} \quad \textbf{3.5}$$

where d_o is the outer diameter of the pressure vessel, and t is it's wall thickness. The design parameters for the recommended pressure vessel are 155psi design pressure, 4.3" outer diameter, and 0.04" wall thickness. The results from these calculations,

$$\sigma_h = \frac{155\text{psi}\big(4.3\text{in} - 2(0.04\text{in})\big)}{2(0.04\text{in})} = 8{,}176\text{psi}$$

$$\sigma_l = \frac{155\text{psi}\big(4.3\text{in} - 2(0.04\text{in})\big)}{4(0.04\text{in})} = 4{,}088\text{psi}$$

can be input into the equation for planar von Mises Stress,

$$\sigma' = \sqrt{{\sigma_h}^2 - \sigma_h\sigma_l + {\sigma_l}^2} \quad \textbf{3.6}$$

to yield

$$\sigma' = \sqrt{(8176\text{psi})^2 - (8176\text{psi})(4088\text{psi}) + (4088\text{psi})^2} = 7{,}081\text{psi}.$$

A point on the cylinder wall of the pressure vessel model shown in Figure 3.9 has a von Mises Stress of 6,966psi, a value close enough to be validated by the 7,081psi von Mises Stress calculated above.

Table 3.2: Recommended Air Supply Design Specifications

Dimensions	
Outside Length	10in
Outside Diameter	4.3in
Wall Thickness	0.04in
Heads	
Positive	Spherical - Convex
Negative	Spherical - Convex
Material	Aluminum 6061-T6
Yield Strength	40ksi
Weight *(includes fittings)*	0.65 lbs
Supply Capacity	$119in^3$
Critical Flow Time*	3.4s
Maximum Von Mises Stress	23.5ksi
Factor of Safety**	1.70

*Time to drop to 28psi with 1.2mm orifice diameter and 125psi initial pressure
**Calculated as $FOS = S_y/\sigma_v$, where S_y is yield strength of material and σ_v is the maximum von Mises stress at 155psi of internal pressure

The outer dimensions of the air supply are dictated by the limited space available onboard the robot. To make the most of this space, a pressure transient analysis was conducted, showing that higher initial pressures with smaller outlet diameters could provide consistent flow rates. However, these higher initial pressures come with a cost; the wall thickness must be increased to withstand the stress induced on the supply tank, and thicker wall directly translate to higher weight. A sufficient supply design is recommended that uses spherical heads and outlets on the cylinder walls and is sized to take full advantage of the available space onboard the GSR.

Chapter 4

Experimental Results

Due to the highly desultory nature of particles flowing in a gaseous medium, a heuristic approach was taken to investigate pneumatic particulate collection for the current application. In this chapter, two methods of pneumatic particle collection are tested: jet impingement collection and particle entrainment collection. Jet impingement collection entails the air jet being aimed into the debris at an angle and using the reactionary force generated from the particles impacting the bed to transport the debris into the collection chamber. Particle entrainment, however, utilizes a jet of air flowing parallel to the particle bed. Although in particle entrainment the jet will impact the bed (albeit at a much lower velocity than in jet impingement) due to the jet's spread upon exiting the nozzle, the jet also utilizes the entrainment of the surrounding air to transport particles.

In addition to the methods of pneumatic particulate collection, a particular vacuum sampler is evaluated experimentally. Though not a form of particulate sampling considered as

an option for the final design presented in this thesis, consideration must be given to the effectiveness of the vacuum sampling method as a reference.

This chapter will present the composition of the particulate debris mixture used in testing and experimental results from a vacuum sampler evaluation, jet impingement testing, depth testing, and high-speed video testing.

4.1 Debris Sample Composition

The purpose of fabricating a representative debris mixture is to accurately simulate the debris one would desire to sample at a blast site, while still maintaining a certain level of order to the mixture's composition for controlled testing. The debris used in this study is a mixture of (by mass): 7 parts fine particulate—a sand-flour mixture[1], 6 parts metal BBs, and 1 part plastic BBs. The heavier chunks of the mixture, the metal BBs in particular, seem to fall to the bottom, which will be the case at the blast site. As noted by Bagnold[7], the average fall rate of particles will be smaller for finer particulate[2] after becoming airborne immediately following a blast, the finer particles will tend to fall to the ground slower than the larger ones causing them to sit more on top of the debris mixture when all has settled.

Particle characteristics for the mixture components used in this study are presented in Table 4.1. The absolute density is the density of the material alone, whereas the bulk density is the density of the particle material and the air that occupies the same between the particles in a particle bed, hence the lower values for the bulk density.

[1] The sand-flour mixture is composed of equal parts sand and flour by *volume*.
[2] Although, closer to his point, Bagnold's observation was that, even within a category of particle sizes, fall velocities would greatly vary due to irregular particle shapes.

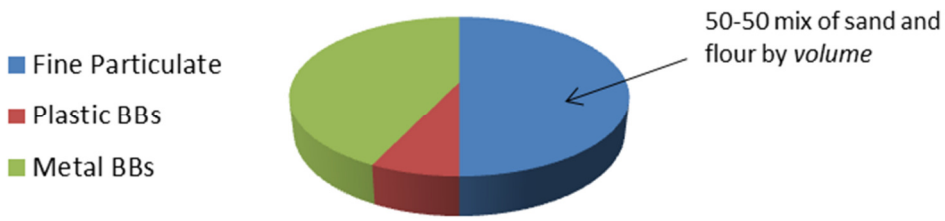

Figure 4.1: Debris Composition by Mass

Table 4.1: Particle Properties

Particle	Diameter	Mass (*g*)	Absolute Density (g/cm^3)	Bulk Density (g/cm^3)
Flour	1-100 µm	*N/A*	0.8	1.35
Sand	100-1000 µm	*N/A*	2.4	
Plastic BB	6.0 mm	0.12	1.1	0.6
Metal BB	4.5 mm	0.33	6.9	4.6

Although, the plastic and metal BBs are spherical in shape and are all identical, the flour and sand particles are certainly not. The diameters shown in this table are to be considered a characteristic length of the particle and are not meant to imply any level of sphericity. No attempt was made to quantify the sphericity of irregularly shaped particles.

Note that it is necessary to measure the individual components of the mixture during testing because the composition of the debris collected will be different from the initial composition as some types of particles are collected more easily than others. Later in this thesis, the volume-mass conversions of the collected samples will use the bulk density of the fine particulate and the absolute density of the BBs because the assumption is made that the fine particulate will fully fill the voids between BBs.

4.2 Vacuum Samplers

Some work has been done to develop particulate samplers for unmanned material sampling, and it is widely assumed that vacuum systems are the best designs. In order to present the novel pneumatic sampler design as a viable alternative, the vacuum design and its performance must be investigated thoroughly.

Sandia National Laboratories has developed the Atlas vacuum sampler to be used to collect particulate debris. Their design utilizes suction pressure to lift particulate off the ground and into a collection cup. The sampler is designed to be gripped by the end-effector (the Intelligent Gripper) of an articulating arm such that the Intelligent Gripper completes a circuit to power the vacuum motor and sends commands via an ASCII based protocol to control the vacuum sampler. The sampler uses a filtration screen with an opening size of approximately 700μm.

The vacuum sampler by itself weighs 2.4 lbs and has approximate dimensions of 6in × 3.25in × 14.5in (l × w × h), making it much too large for use on the ground sampling robot. Additionally, it was measured that the motor consumes 103W of power, drawing 7.5A during operation, meaning its electrical power requirement is well above what the ground sampling vehicle could realistically provide.

An experiment was designed to be comparable to the experiments to which the pneumatic sampler was subject. Because of fundamental differences in their collection method, the two designs could not be evaluated by identical tests, so consideration should be given to this fact in interpreting the tests results.

4.2.1 Performance Testing Overview

Two different tests were run to evaluate the performance of the vacuum sampler. First, the amount of total particulate and the amounts of each type of particulate collected was measured for a single touch down, along with the duration of the touch down[1]. In the next test, the number of touch downs it took to collect a target volume of debris was recorded.

The particulate debris mixture was modified slightly from debris mixture described in Section 4.1; instead of using a sand-flour mixture, only sand was used as the fine particulate. Since the vacuum sampler uses only a wire mesh screen as a filter, the flour particles were too fine to be collected in the collection cup. The rest of the mixture was the same, however. That is, a 70g sample was comprised of 35g of fine particulate (now just sand, not sand-flour mixture), 5g of the light plastic BBs, and 30g of heavy metal BBs.

To test the vacuum sampler, a test stand was constructed to simulate a controlled descent to the ground that an articulating arm would otherwise provide. Figure 4.2 shows the sampler in its test stand. The sampler can slide on low-friction linear bearings so that the intake would continue to be in contact with the debris as the debris level falls, just as if a robotic manipulator were to apply continuous force to keep the sampler in contact with the ground.

[1] A touch down refers to the single action of the sampler making contact with the ground in order to collect the debris.

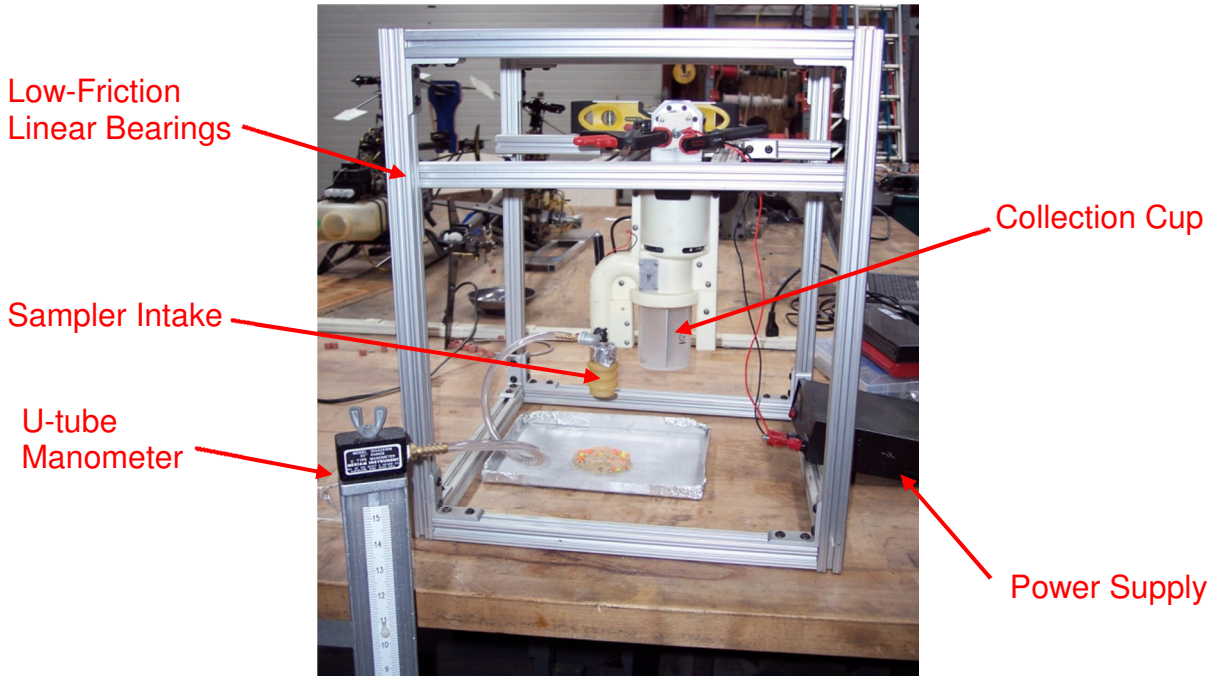

Figure 4.2: Vacuum Test Stand Overview

4.2.2 Single Touch Down Test

For the single touch down test, the 70g debris sample was placed in a small 8 fl oz Styrofoam cup as in Figure 4.3, so that the vacuum sampler would collect as much particulate as it was capable of collecting without the possibility of the debris spreading out and becoming harder to reach. The depth of the sample in the cup was 7/8in and is indicated in Figure 4.3 with a red arrow.

Figure 4.3: 70g Debris Sample

During the single touch down test, the vacuum pressure was measured with a U-tube manometer as shown in Figure 4.2. The sampler creates a suction pressure of up to 4.0 inches of water.

Five trials were run for the single touch down test, and the results can be viewed in the bar plot in Figure 4.4. Note that the vacuum sampler was unsuccessful in collecting the heavier metal BBs in all trials. Furthermore, the tests show a level of inconsistency. This lack of consistent collection can be attributed to the seal that the sampler intake makes with the ground. The intake is a short, flexible, rubber hose that compresses as the sampler pushes against the surface of the particulate debris. Often times, it was observed, the flexible hose would sink into the debris and suck up a small amount of particulate, but then stop. Since the intake was beneath the surface of the debris, there was no new air to replace the air that had been sucked up the intake, and therefore, there was no fluid flow to entrain the particles or break them free from whatever interparticle adhesive forces was holding them down. With the suction of the sampler so low, despite the massive power draw, the lifting forces on the particles were not enough to transport them into the collection cup.

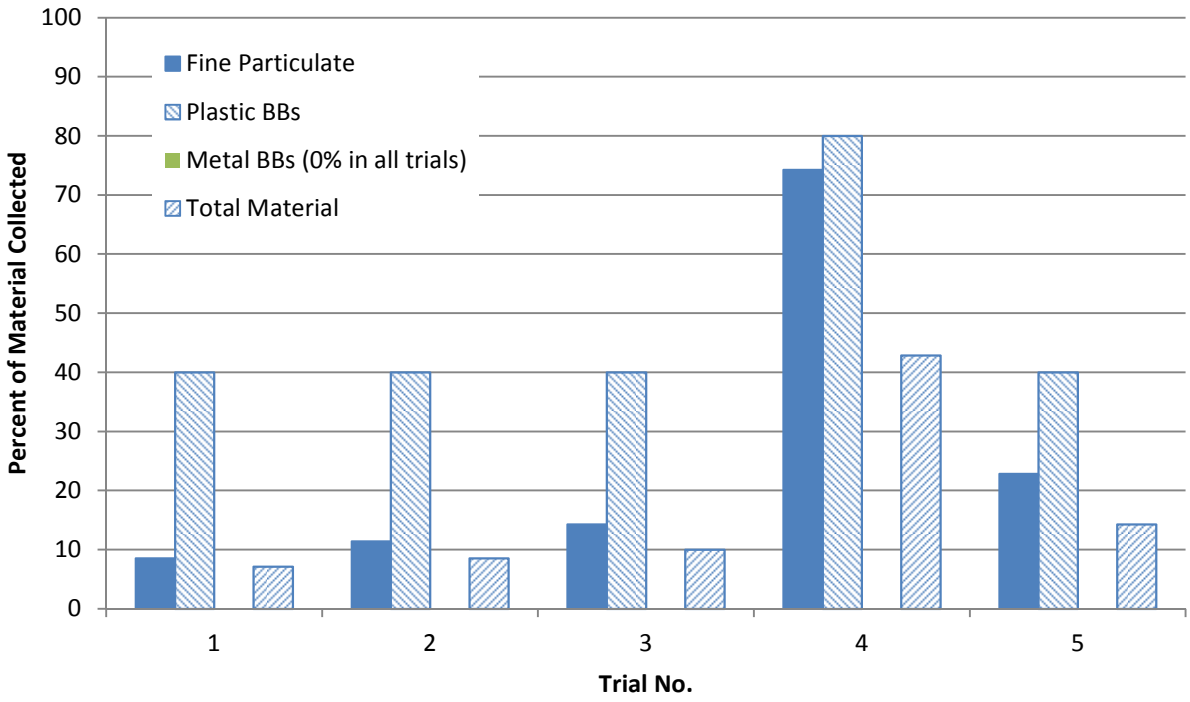

Figure 4.4: Single Touch Down Vacuum Sampler Test Results

The single touch down test was also needed to assess how much time the sampler took to collect all that it was going to collect on one touch down. Figure 4.5 also illustrates the lack of consistency in the design's performance by graphing the length of time it took to collect particulate as a function of the amount of material collected. Because there is no relationship between these two variables, the flow rate of particulate into the collection cup is clearly not consistent. Again, this variance can be attributed to the lack of constant fluid flow to entrain the particles.

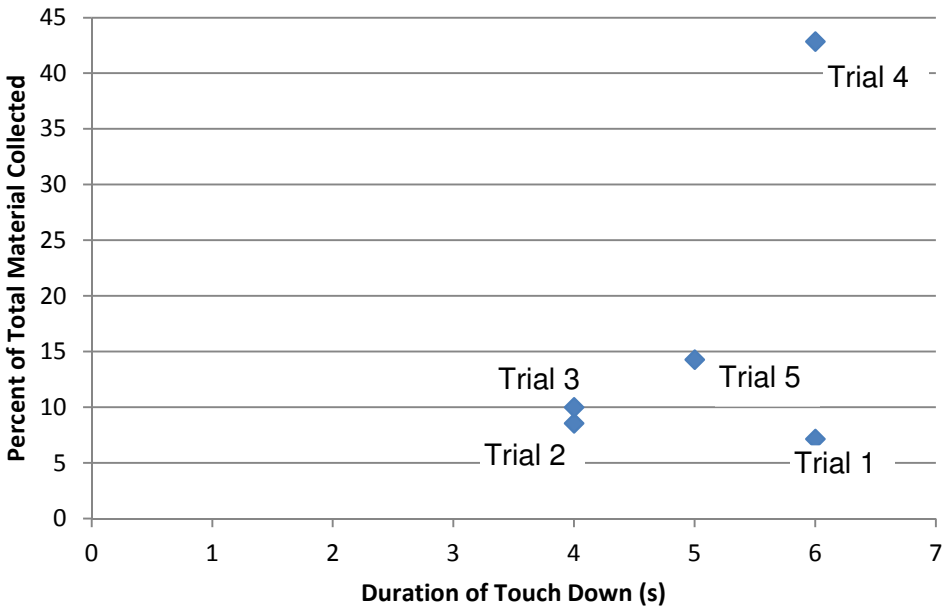

Figure 4.5: Vacuum Sampler Single Touch Down Duration

From the data collected in this test, and presented above, the average duration of a single touch down is 5s.

4.2.3 Multiple Touch Down Test

The second test was concerned with the number of touch downs necessary to collect the desired volume of debris. This volume is determined by a fill line on the collection cup provided by Sandia, which corresponds to 50cc of collected material. The test was conducted by laying out a 210g sample of particulate of proportional composition to the 70g sample described earlier, spread to a uniform depth of 5/8in. The sampler was then lowered to the particulate and left until it was done collecting debris at that point. Then, it was lifted, moved to a different point in the spread of debris, and lowered. This process was repeated until the desired volume had been collected. The results for three trials are shown in Table 1. The average number of touch downs required to collect 50cc of particulate is 3.7.

Table 4.2: Vacuum Sampler Multiple Touch Down Test Results

Trial (#)	Number of Touch Downs (#)
1	4
2	4
3	3

With multiple touch downs required to get such a small volume of debris, one must consider the operational cost of this design's method of collection. For every touch down the sampler must make, there is an extensive amount of effort and time that is required to reposition the sampler remotely using a cumbersome robotic manipulator. Additionally, each touch down requires a large amount of electrical power—103W as mentioned earlier. Assuming 4 touch downs, each 5s in duration, this design requires 20s of vacuum motor runtime to collect 50cc of debris. Certainly, drawing 103W for 20s, which equates to approximately 2,000J of electrical energy, would require a much heavier battery.

Figure 4.6 shows the debris spread before (left) and after (right) collection. Notice that in the photograph taken after collection, the points where the sampler had touched down are marked by an absence of sand and plastic BBs, but a concentration of heavier metal BBs. The sampler's inability to collect the heavier particles proved to be a limitation of the design caused by insufficient lifting forces on the particles from low suction levels as discussed earlier.

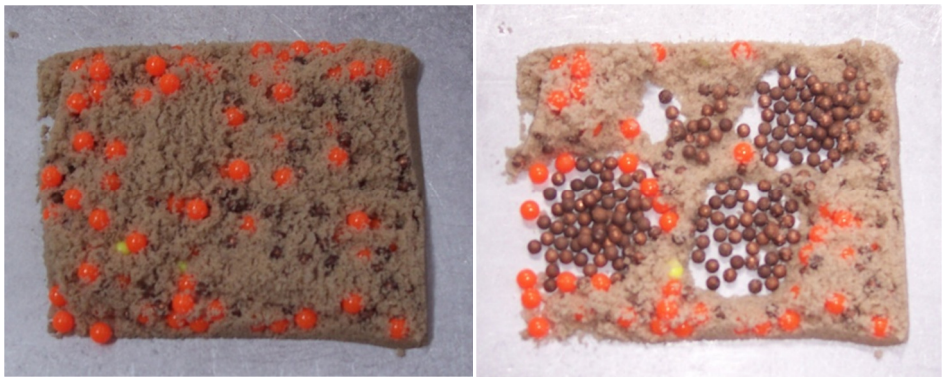

Figure 4.6: Vacuum Sampler Multiple Touch Down Test Debris Sample

From this investigation, the limitations of the vacuum sampler design become evident: its bulky size and high weight, its lack of consistency, its massive power draw, and its inability to pick up heavier particles.

4.3 Jet Impingement Testing

To experimentally explore the jet impingement method of particulate collection, a test procedure was created as a way of ensuring uniformity of all trials and iterations of the testing. The purpose of this testing is to evaluate the feasibility of jet impingement as a possible method of particulate collection and to gather data that will provide insight into the optimization of certain metrics of the pneumatic sampling method. Namely, there are five parameters to be investigated: *angle of attack*, *array angle*, *orifice diameter, nozzle pressure*, and timing parameters including *number of pulses* and *pulse duration*. These terms are all defined in the following section as part of the description of the experimental setup.

4.3.1 Experimental Setup

The test rig in Figure 4.7 and Figure 4.8 for the jet impingement testing consists of a body fabricated out of polycarbonate by a Stratasys Fused Deposition Modeling (FDM) system (see Appendix F for data sheets) and a clear, abrasion-resistant polycarbonate lid and side viewing window to allow flow visualization. The rig is divided into two chambers, a sampling chamber and a collection chamber, which are separated by a ramp. An array of three nozzles with two-axis angle adjustment capabilities is positioned in the end wall of the sampler rig. Air is released from an air compressor by actuating a solenoid valve. The air then flows through the nozzles into the sampling chamber where particles are impacted and transported up the ramp and into the collection chamber. An exhaust port is located above the collection chamber where air can escape, but particulate is filtered out and remains in the collection chamber or trapped in the filter.

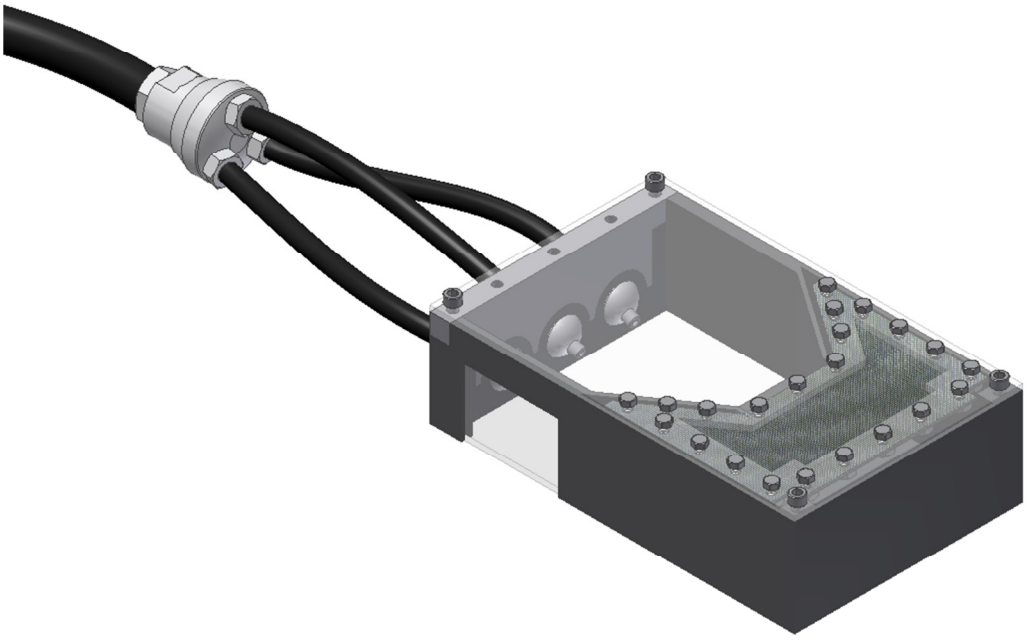

Figure 4.7: Jet Impingement Test Rig

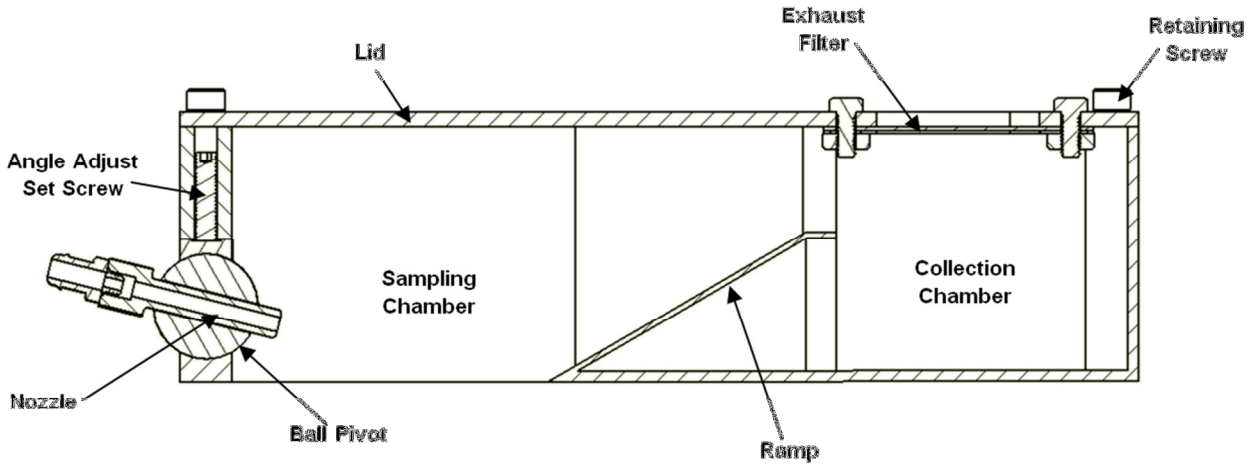

Figure 4.8: Jet Impingment Test Rig Diagram

As stated earlier, five parameters were investigated with this test setup: *angle of attack*, *array angle*, *orifice diameter, nozzle pressure*, and timing parameters including *number of pulses* and *pulse duration*. Angle of attack is the angle between the ground and the nozzle axis as in Figure 4.9.

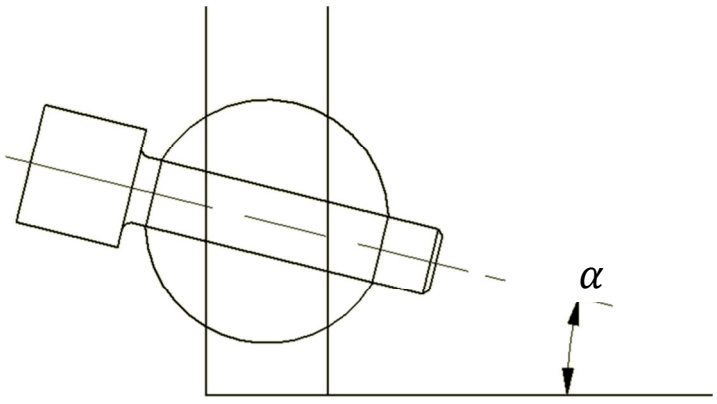

Figure 4.9: Angle of attack

Array angle is the angle between the outside nozzles and the center nozzle as in Figure 4.10. The center nozzle will be held constant at 0° for all trials.

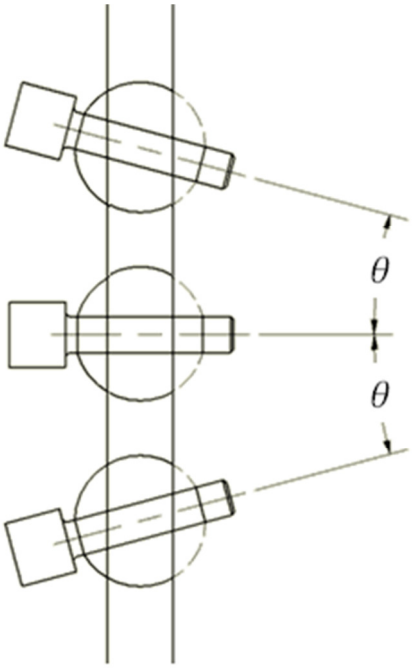

Figure 4.10: Array Angle

The above angles were adjusted and set using LabVIEW and a camera to position the nozzles in line with an overlaid leveling line. The nozzle alignment process is illustrated in Figure 4.11 and Figure 4.12.

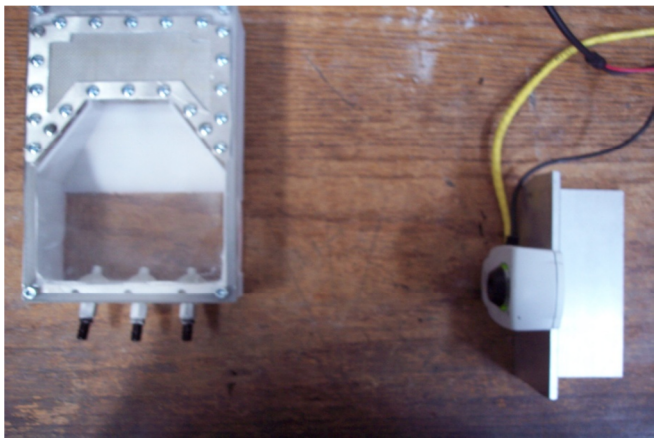

Figure 4.11: Nozzle Alignment Setup

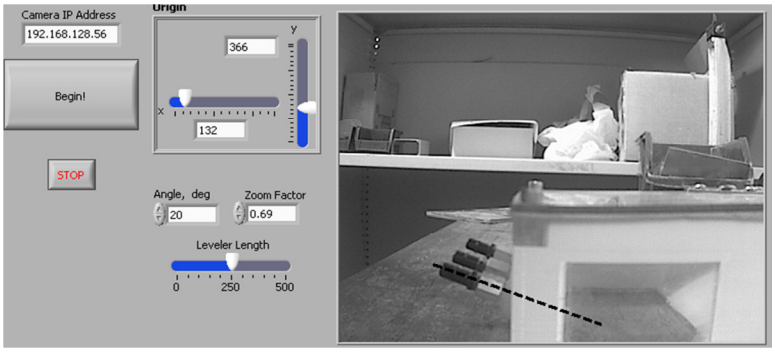

Figure 4.12: Nozzle Alignment Screenshot

Orifice diameter is the diameter of the hole in one of the 3 identical nozzles through which the air enters the sampling chamber. Although, it should be noted that the flow being studied is actually flow through a sharp-edged orifice, not a nozzle. The image below shows the orifice from which the flow emerges into the sampling chamber.

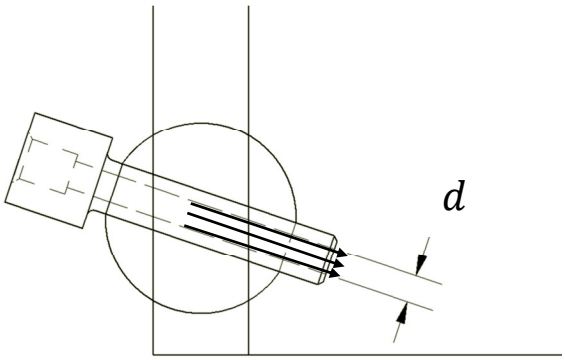

Figure 4.13: Orifice Diameter

Nozzle pressure is the pressure read by a gauge on the compressor that supplies the compressed air to the system, and there is a regulator connected to the outlet of the compressor to adjust the nozzle pressure. The pulse duration is the amount of time that the solenoid valve is held open and air is allowed to flow into the sampling chamber, and the number of pulses is the number of times the solenoid valve is opened and air is released into the sampling chamber.

LabVIEW was used to control the actuation and timing of the pulses by controlling a relay to switch the power supply to the solenoid valve on and off. To simulate the weight of a portion of the robot on top of the sampler during testing, a 5.5 lb weight was laid on top of the sampler to counter the force the jets apply on the ground that would otherwise result in lifting the sampler. Figure 4.14 is photograph of the jet impingement experimental setup.

Sampling was conducted after a 70g debris sample was placed in the sampling chamber. Once the sampling was complete, the amount of particulate collected was measured. The collected particulate was sorted into its individual components: the flour-sand mixture, the plastic BBs, and the metal BBs. The mass of each was measured and used to calculate the percentage that was collected of material initially available.

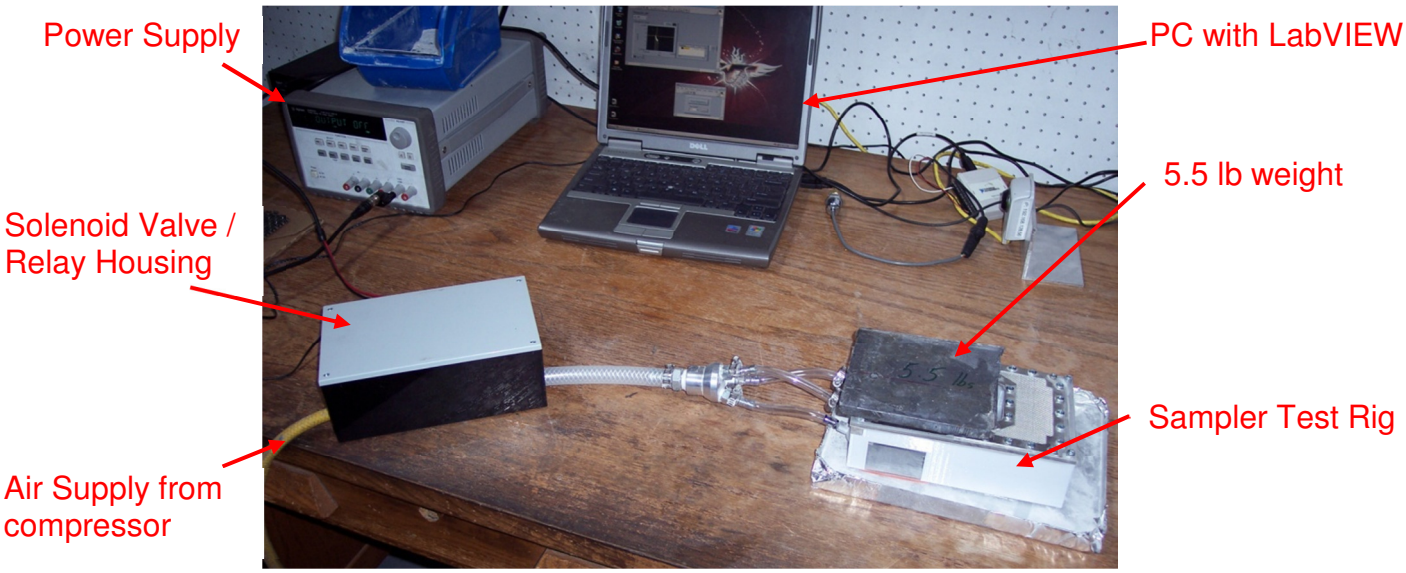

Figure 4.14: Photograph of Jet Impingement Experimental Setup

4.3.2 Jet Impingement Test Results

The first parameters to be investigated using the jet impingement test rig were the nozzle pressure and pulse duration / number of pulses. Because a limited volume of air is available onboard the robot, it is desired to know whether pulsing the air into the sampling chamber is more effective at collecting particulate than a constant flow of the same volume of air. To study these parameters, it was assumed that the effect of the timing parameters is independent of test rig geometric configuration, so an initial configuration was chosen arbitrarily and three timing sequences were tested, all of which result in the same final total flow time: ten 100ms pulses, three 333ms pulses, and one 1000ms pulse.

The following three figures each present the results of one of the aforementioned timing sequences with a 40° angle of attack, 20° array angle, and a 4.00mm orifice diameter. The plots show the percent of the initial amount of material that was collected for low, medium, and high nozzle pressures. The results are broken down to show how each timing sequence and nozzle pressure effected the collection of each type of particulate.

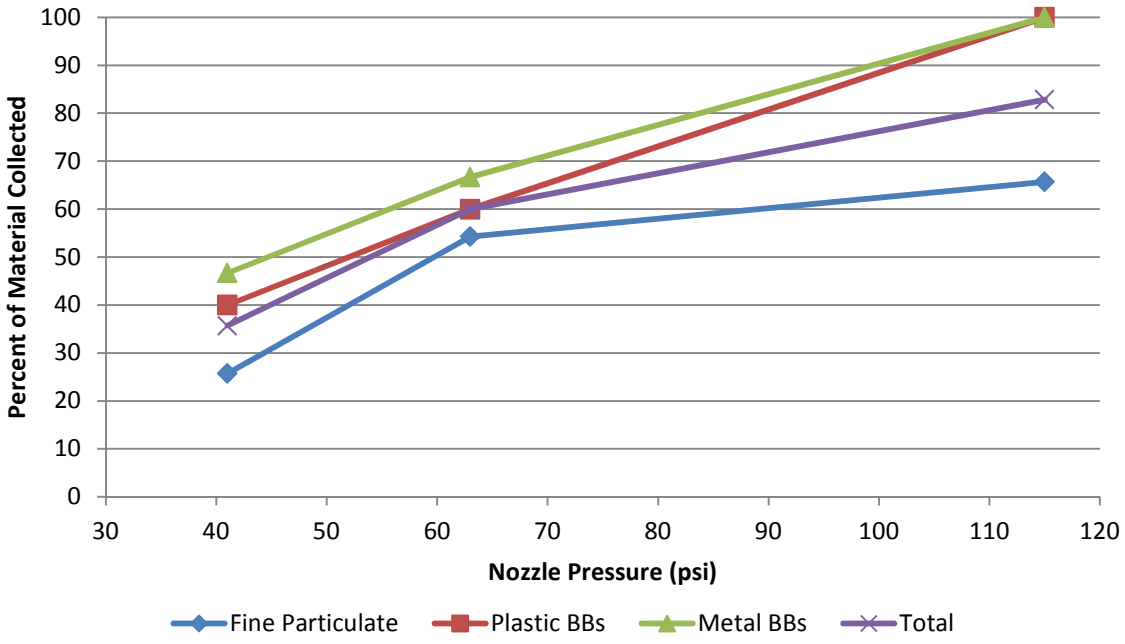

Figure 4.15: Jet Impingment – Ten 100ms Pulses

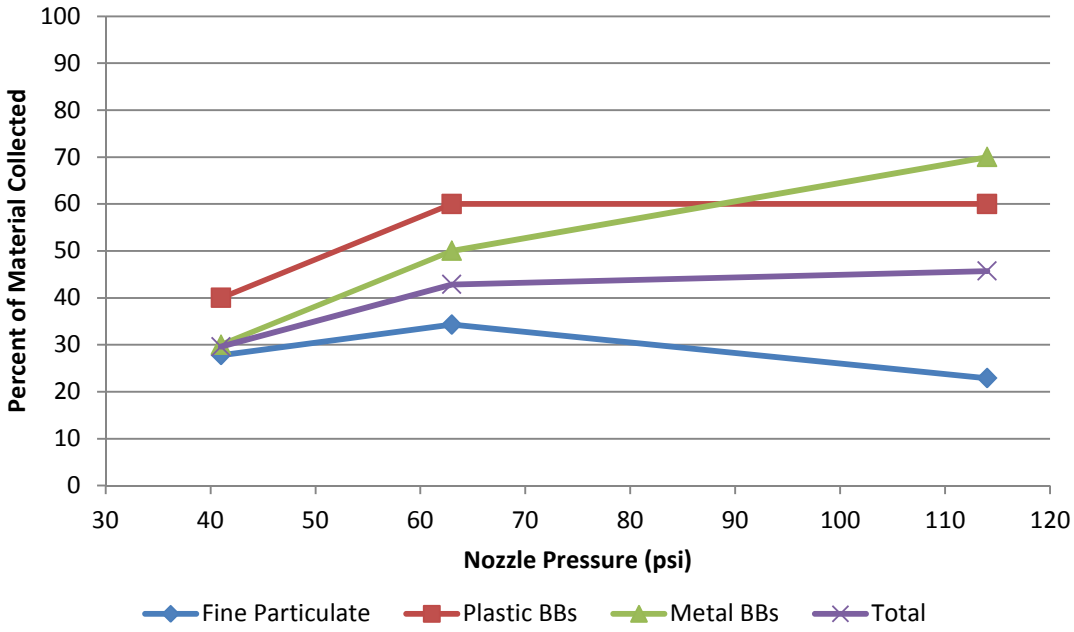

Figure 4.16: Jet Impingement – Three 333ms Pulses

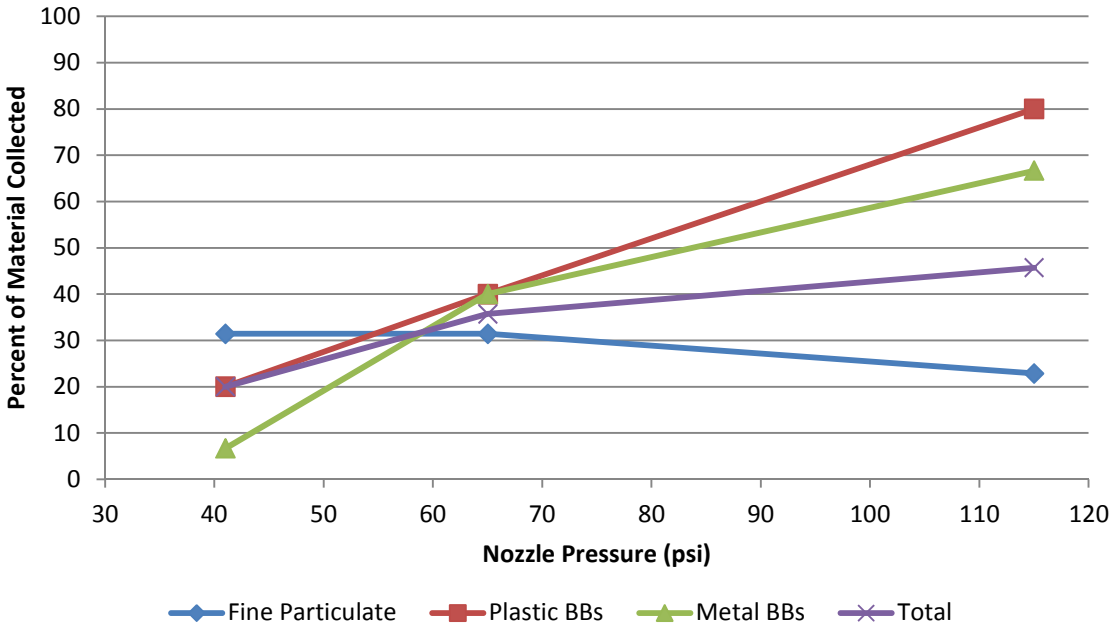

Figure 4.17: Jet Impingement – One 1000ms Pulse

The three plots look very similar in their trends. That is, in all cases, the amount of material collected increased as the pressure increased with the exception of the fine particulate. The slight decrease in fine particulate collection can be attributed to the fact that the test rig lifts off the ground from the reactionary force of the air jets impacting the ground, despite the weight on top of the rig to simulate the robot. The height above the ground that the rig reaches is on the order of millimeters, but it is enough that the fine particulate can escape. Since an increase in nozzle pressure would increase the thrust the air jets generate, the amount of fine particulate that escapes the sampling chamber increases as well.

Despite the similarity in trends demonstrated in these plots, the magnitude of the amount of material collected for each timing sequence does vary, and ten 100ms pulses seems to be the most effective. The percent of total material that was collected with high nozzle pressure and the ten 100ms pulses, three 333ms pulses, and one 1000ms pulse was 83%, 46%, and 46%, respectively.

Multiple short pulses collect more material than a single long pulse because of the concept of saltation that was introduced in Section 2.2.2. Once the particles have initially been made airborne by the impact of a preceding pulse of air, a second pulse will transport the particulate without having to fight the interparticle forces present in the particle bed. A single long pulse will tend to trap particles, whereas multiple pulses will break them free, so the remainder of the testing was conducted using a timing sequence of ten 100ms pulses for a total flow time of one second at high pressure (115psig).

The next set of parameters to explore using the jet impingement test rig are the orifice diameter, the array angle, and the angle of attack. Figure 4.18 shows the material collection data for the test rig with the nozzles all parallel to each other (0° array angle), using high pressure air released in ten 100ms pulses.

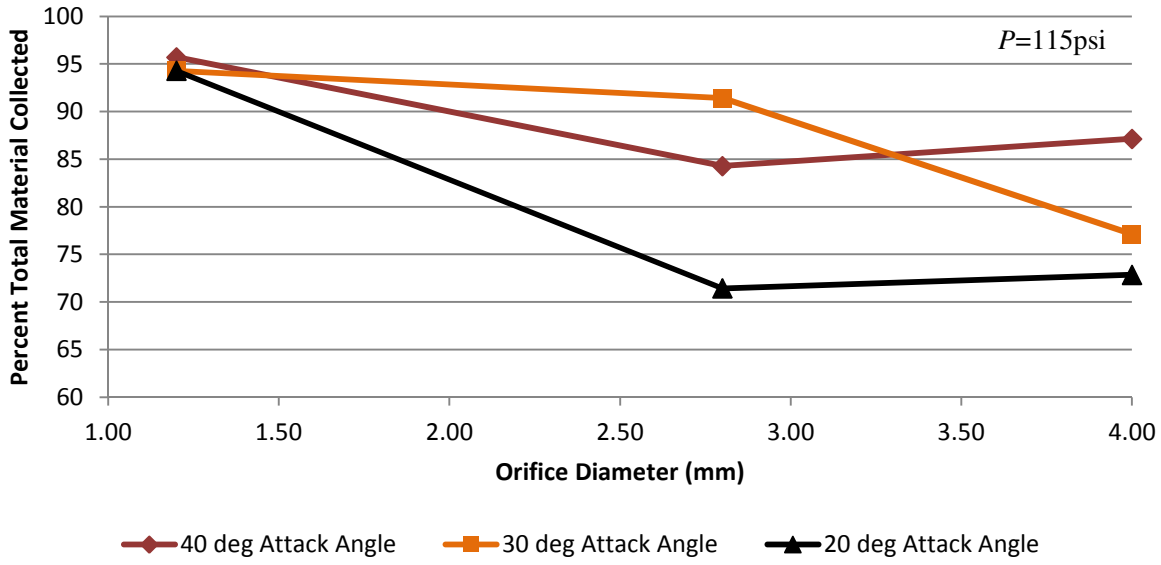

Figure 4.18: Jet Impingment – 0° Array Angle

The data show consistently high collection rates, around 95%, across all angles of attack at small orifice diameters. A trend is distinguishable that shows smaller orifice diameters will

collect more particulate material than larger orifices. Although the flow is choked in all cases and the air is therefore released into the sampling chamber with an initial velocity of Ma=1, the mass flow rate is greater for larger orifice diameters, so it is surprising to see that smaller diameters were more effective in collecting more material. However, since the air is in a more concentrated stream when it hits the particle bed for smaller diameters, it impacts the particles harder and sends them higher off the bed surface, thereby giving them a better push up the ramp into the collection chamber. With larger diameters, a greater number of particles are initially impacted, but with a significantly smaller force, and thus, those particles are not sent high enough off the bed surface to climb the ramp.

Figure 4.19 presents the empirical data for 1.2mm orifice diameters using high pressure air released in ten 100ms pulses. Again, a trend is visible that indicates greater particle collection when the nozzles are pointed more parallel to each other.

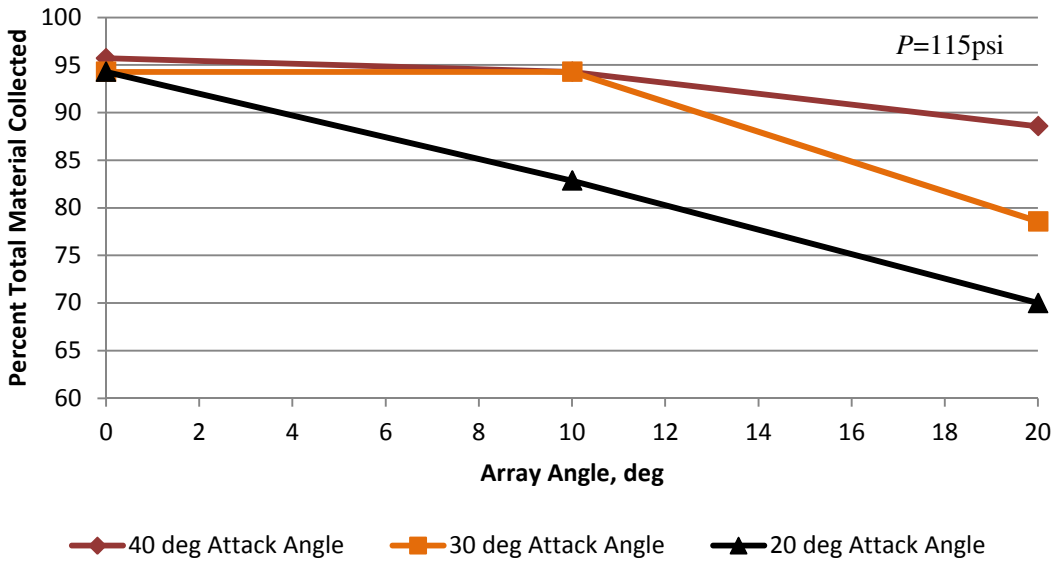

Figure 4.19: Jet Impingment – 1.2mm Orifice Diameter

When the array angle is greater, the air jets will interfere with one another causing more particle collisions in the turbulence generated in the sampling chamber. The jet interferences will also prevent each air jet from impacting the bed surface with as high a force as it otherwise would have, causing fewer particles to climb the ramp into the collection chamber.

From observing Figure 4.18 and Figure 4.19, one can see that, with the exception of one data point in Figure 4.18, a steeper angle of attack collects more material. Again, this can be attributed to the increased impact force on the particles.

From the jet impingement testing, it was found that methods with multiple pulses at high nozzle pressure with small orifice diameters, steep angles of attack, and small array angles will collect the most particulate material. However, consideration must be given to the quality of the sample collected because, as mentioned before, only the top 5/8" of the particle bed is desired.

4.4 Depth Testing

The jet impingement test rig was used to find the depth to which particles were sampled in the jet impingement sample collection process. This depth testing was performed by placing the sampler on a bed of sand which had been layered such that each ¼" of sand was a different color. The setup for the depth testing is depicted in Figure 4.20.

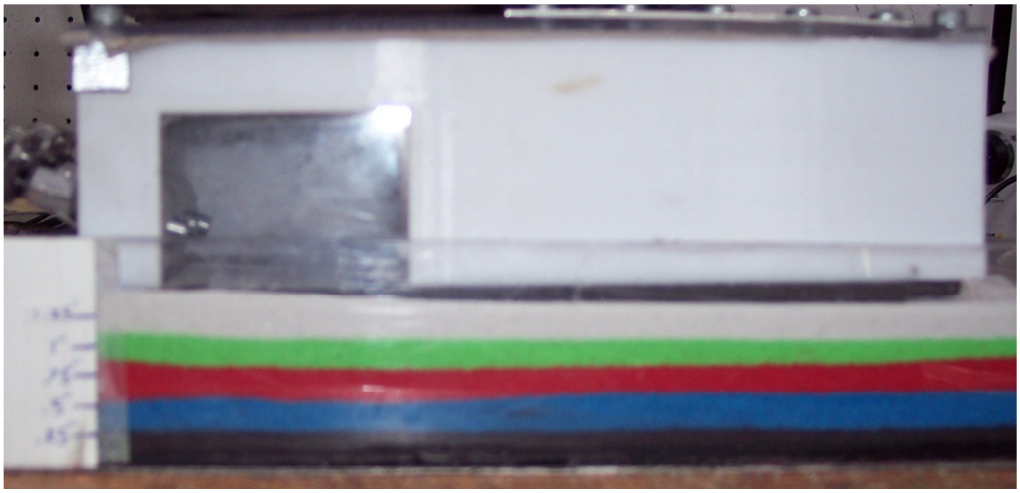

Figure 4.20: Depth Testing Setup

Using this setup, it is possible to determine a range of the depth at which the deepest particle that was sampled initially laid. The test rig was run using the most effective configuration determined in Section 4.3.2 at various angles of attack: ten 100ms pulses with a 1.2mm orifice diameter, 115psig pressure, and 0° array angle.

Table 4.3 summarizes the results of the depth testing and shows that only a 0° angle of attack, where the nozzles are pointed parallel to the particle bed surface, will sample from an appropriate depth.

Table 4.3: Depth Testing Results

Angle of Attack *(°)*	**Maximum Depth Sampled** *(in)*
40	$D \geq 1$
30	$D \geq 1$
20	$D \geq 1$
10	$3/4 \geq D \geq 1$
0	$1/2 \geq D \geq 3/4$

When the nozzles are adjusted to an angle of attack of 0°, the nozzles are parallel to the bed surface, and the sampling method is no longer considered jet impingement, but rather particle entrainment. Therefore, the depth testing has shown that particle entrainment is the preferred method of material collection given that only the top 5/8" layer of debris is desired to be collected.

4.5 High-Speed Video Testing

A Photron FASTCAM APX-RS mono was used to capture video of the flow through both the side and top viewing windows of the test rig at 6,000fps. Using high-speed imaging made it possible to visualize the incredibly fast sampling process that was occurring within the sampler test rig. Without the proper equipment, flow characteristics were indistinguishable because each pulse of air caused an explosion of particles within the sampler, and a plume of fine particulate that had escaped the sampler formed outside its walls.

The high speed video was used to visualize both particle entrainment sampling and jet impingement sampling, and several useful observations were made from the data.

4.5.1 Jet-Impingement High Speed Video Testing

A sequence of frame captures of the jet impingement flow taken from the top view of the rig are presented in Figure 4.21. The angle of attack was set to 40° for this run, and the nozzle pressure is set to 115psig. Note that the flow is from left to right in each image; that is, the sampling chamber is shown with the particle bed on the left, the black trapezoid in the center is the ramp, and the collection chamber is directly beneath the exhaust filter on the right.

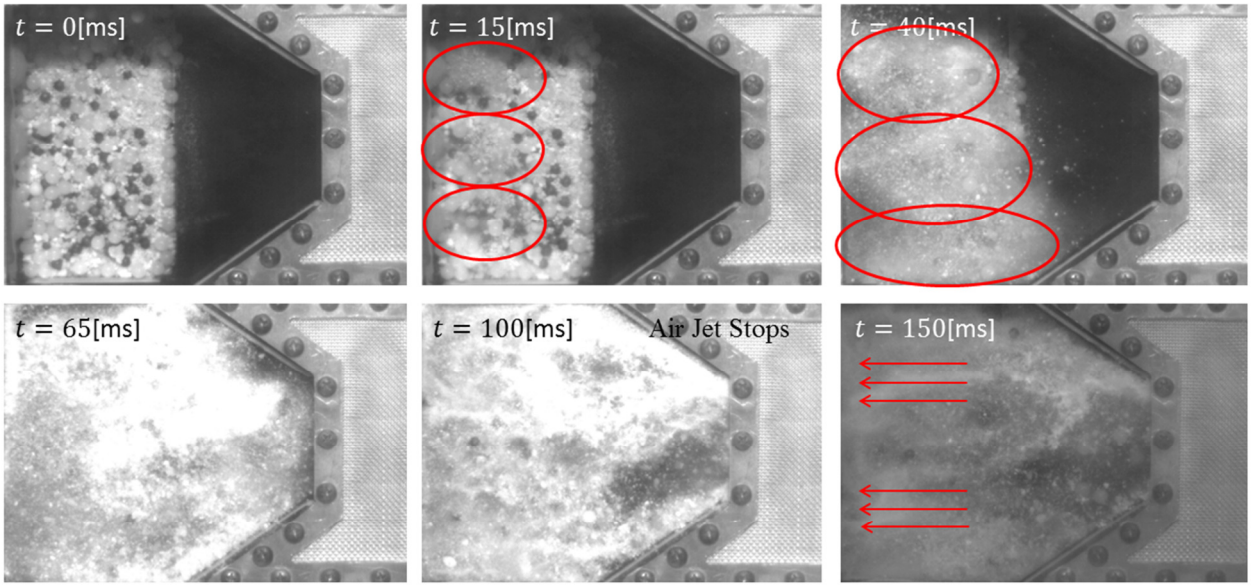

Figure 4.21: Jet Impingment High-Speed Frame Captures

At t=15ms plumes start to form where each jet impacts the particle bed. As time elapses the plumes begin to metastasize, converging with one another causing innumerous particle collisions. When t=65ms, the particles have begun to gather and press against the top of the chamber as is evident from the intense white clouds of particles reflecting the light back to the camera. Soon thereafter a divide is seen where many particles do begin flowing along the top of the chamber toward the right and into the collection chamber, but many of the particles are forced in the opposite direction and recirculate back over top of the nozzles; by t=150ms, streamlines begin to form in that direction.

Interestingly, the test rig configuration in Figure 4.21 was the most effective configuration in terms of total particulate collected as described in Section 4.3.2, collecting 95% of the total material consistently, and a similar result was observed in the trial where these images were taken as well. Despite the chaotic nature of this flow, a desired outcome was achieved.

These images illustrate well how jet impingement works because it is easy to see how the particles are impacted and bounce high, traveling toward the camera, and collide with the top of the chamber and even become pinned there by the air. In this scenario, however, it is easy to see how the particles may react differently than if this were a particle bed much deeper. The particle bed in this test is only about ½" deep, and so the air jet impacts the particles driving them down and bouncing them off of a hard surface instead of more particles.

Figure 4.22 and Figure 4.23 present frames captures of a single burst of air for particle entrainment flow from the side and top views, respectively, for the entirety of the en masse particle motion. The angle of attack is set to 0° (as is characteristic of the particle entrainment method) and the nozzle pressure is 115psi. Note that the above figures depict two separate trials of the same flow configuration, so specific information about a 3rd dimensional component of the flow cannot be gathered based on a comparison.

Using these images, however, it is possible to estimate about how long the debris remains airborne in a state resembling a colloidal suspension after the pulse of air has stopped—information which is useful in ultimately taking advantage of saltation as discussed in Section 2.2.2. Note that the sixth frame in each of the figures below corresponds to the time at which the 100ms pulse or air stops and that the final frame corresponds to the time at which the particulate has completely settled back to the particle bed. In Figure 4.22 the settling time is equal to 475ms whereas in Figure 4.23 the settling time is 565ms. Therefore, with the jet impingement method of material sampling, releasing the pulses of air 200ms after the previous has ended will not only entrain particles on the particle bed at that time, but will also more easily transport the particles still suspended from the previous pulse.

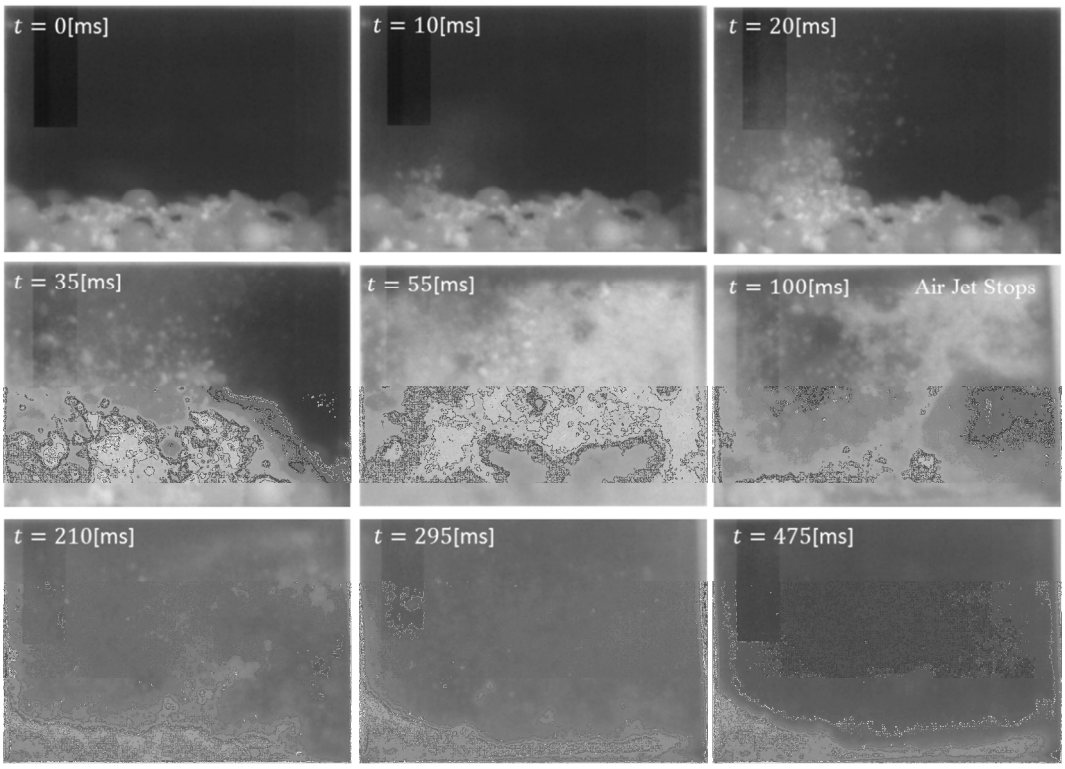

Figure 4.22: Jet Impingement High-Speed Frame Captures – Side View

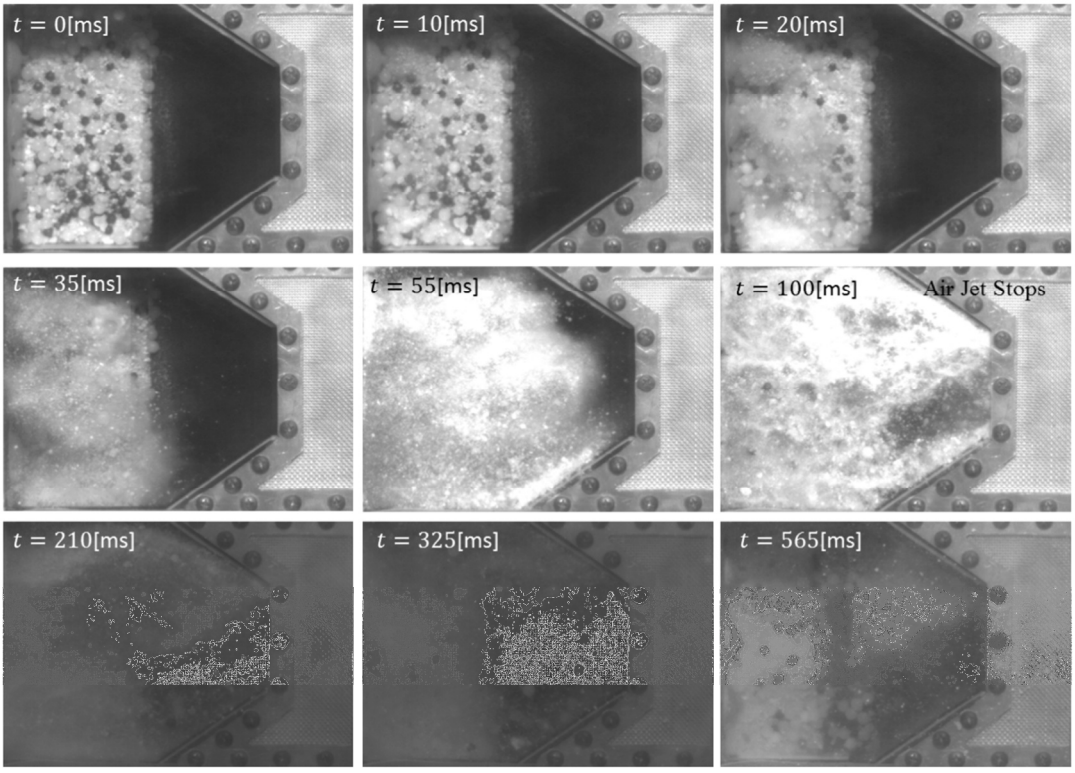

Figure 4.23: Jet Impingement High-Speed Frame Captures – Top View

4.5.2 Particle Entrainment High-Speed Video Testing

Though much less chaotic then the jet impingement, the particle entrainment sampling method would have been impossible to accurately visualize without the use of the high-speed video. Several of the observations made of the jet impingement high-speed testing can also be made from viewing the video of the particle entrainment as well, namely, the issues of jet interferences and recirculation[1][13]. In addition, adverse effects of the ramp geometry of the test rig were also discovered.

The ramp was initially designed as a converging throat with the idea that a decrease in cross-sectional area would accelerate the flow toward the collection chamber, thereby more effectively carrying particulate up the ramp. This idea is why the ramp is bounded by walls that angle inward giving it the trapezoidal shape seen when viewing it from above. However, with such a low flow rate into the chamber, the flow never fully fills the chamber before reaching the ramp, and therefore is not accelerated by the change in area, but rather deflected backward.

Consider the highlighted particle in Figure 4.24, whose direction of motion is indicated by an arrow. The particle is approaching the collection chamber when it strikes the wall of the ramp that was intended to accelerate the flow, and the particle along with it, into the collection chamber. Instead, the wall deflects the particle backward, causing it to be entrained into a recirculating streamlines such that the particle is now accelerating in the wrong direction.

[1] A similar behavior is observed in Panitz and Wasan's experiment, having a detrimental effect on entrainment—in their case—of a secondary fluid.

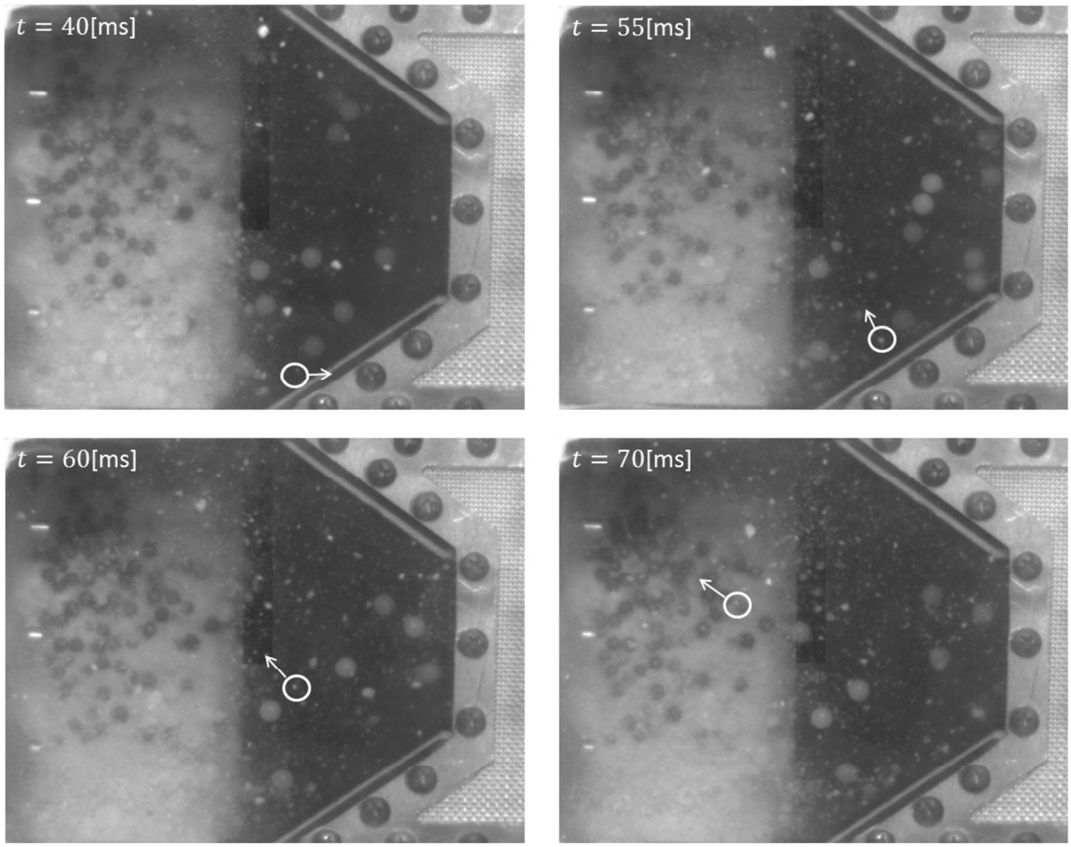

Figure 4.24: Ramp Wall Particle Deflection

The high-speed visualization of the sampling methods allowed for helpful observations which will be addressed in the final design of the sampler. First, an oversized sampling chamber combined with a converging throat feature promotes unwanted recirculation. Additionally, even, with a 0° nozzle array angle, the air jets will interfere with each other causing a myriad of particle collisions that are detrimental to particle collection. Finally, the high-speed video testing presented in this section can be used to provide for a good estimate of the duration of the pause between pulses that will take advantage of the saltation of particles in the jet impingement method of sampling.

Chapter 5

Pneumatic Sampler Design

The novel pneumatic particulate sampler design is composed of four subsystems: the air supply (covered in Chapter 3), the valves, the sampler tool, and the articulation system. With these systems properly integrated, the pneumatic sampler uses the kinetic energy of the expansion of compressed air to transport particulate debris into a collection area. This chapter will cover how that feat is accomplished in this design.

First, key design features of the pneumatic sampler employed based on observations and data from Chapter 4 are outlined. Then, calculations based on previous work in gas dynamics and particulate entrainment studies will be used to characterize the performance of the system. Next, the performance of the sampler will be evaluated experimentally. Finally, a short overview of how the design meets up to the initial design requirements will be presented.

5.1 Key Design Features

The pneumatic particulate collection system is shown in Figure 5.1. It is composed of the air supply prototype discussed in Section 3.2.1 along with the valve assembly and sampler tool, both of which will be presented here.

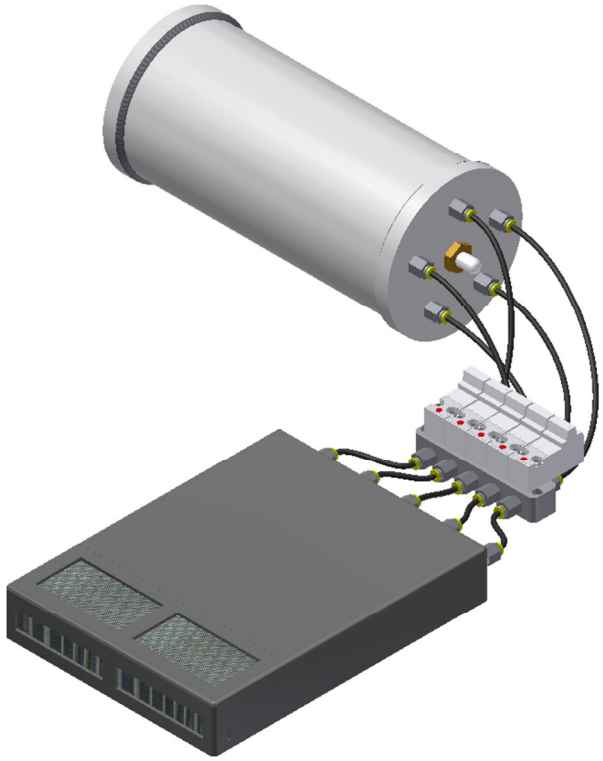

Figure 5.1: Pnuematic Particulate Sampler

5.1.1 Valve Selection

For lab testing purposes the air is contained with the air supply prototype, while a spherical head air supply tank design was recommended in Section 3.2.2 for final product implementation. Actuating the release of the air from the supply tank, though, is achieved with proper valve selection.

The valve assembly is placed in line between the air supply tank and the sampler as in Figure 5.2. The valve assembly is made up of five valves connected to a manifold with 10 quick-disconnect connectors, one for the inlet and outlet of each valve. The valves selected are direct acting solenoid valves from Clippard's 15mm Miniature series and have a 10ms energizing and 12ms de-energizing response time[14]. The manifold to which the valves connect is customized (see Appendix E for drawings) because Clippard does not make an off-the-shelf five-port manifold.

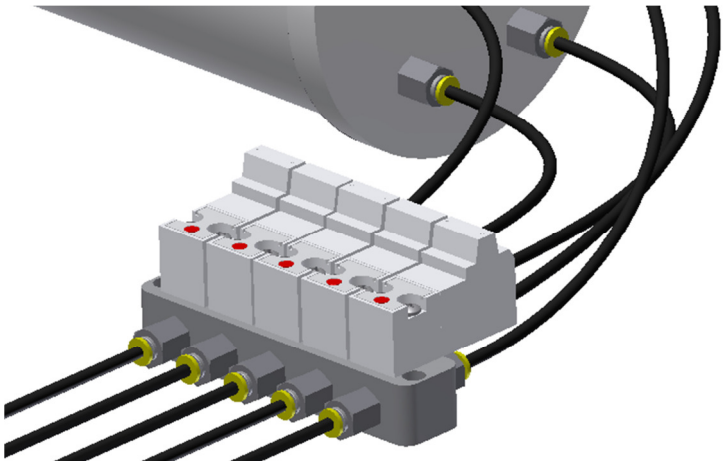

Figure 5.2: Valve Assembly

This design utilizes five individual valves rather than one large valve in order to release the air into the five nozzles of the sampler tool. By using five valves, each valve can be significantly smaller and lighter and the need for a bulky manifold is eliminated. Table 5.1 presents a weight comparison of three different valve assemblies found to provide the desired flow rates as shown in Appendix B. Note that the single valve assembly is heavier than both of the five-valve assemblies, the current and recommended. For the final product implementation, the ASCO 411 Series valves are recommended because they are comparable to the current Clippard valves, but do not use a manifold—rather, they can be line mounted—allowing for a 44% reduction in weight.

Table 5.1: Valve Assembly Weight Comparison

	Quantity	Part Description	Individual Weight *(lbs)*	Total Weight *(lbs)*
Current Valve Assembly	5	Clippard E215F-2W012 15mm Miniature Valve (12VDC - 2.5W)	0.088	0.44
	1	Five Inlet – Five Outlet Manifold	0.150	0.15
	10	10-32 Quick Disconnect Fitting	0.018	0.18
			Total:	**0.77 lbs**
Single Valve Assembly	1	ASCO 8262H014 General Service Solenoid Valve(12VDC - 10.6W)	0.410	0.41
	1	Single Inlet - Five Outlet Manifold	0.203	0.20
	3	1/8" NPT Fitting	0.049	0.15
	5	10-32 Quick Disconnect Fitting	0.018	0.09
			Total:	**0.85 lbs**
Recommended Valve Assembly	5	ASCO 411L2112HV 2-Way Miniature Solenoid Valve (12VDC - 2.0W)	0.050	0.25
	10	10-32 Quick Disconnect Fitting	0.018	0.18
			Total:	**0.43 lbs**

* Note: Weight totals do not include tubing

The valves are operated by providing a 12V signal for the duration of the desired air pulse. The recommended valves have a 2.0W power rating, so five valves would require 10W of power for the four seconds of flow time it takes to purge the air supply. Comparing this power consumption to the 103W for 20s of run time for the operation of the vacuum sampler of Section 4.2, the benefit of using a pneumatic system onboard the lightweight robot becomes clear.

5.1.2 Sampler Tool

The sampler tool, shown in Figure 5.3, is made up of two subassemblies: the sampler tool body assembly and the filter cap assembly. The sampler tool body assembly consists of the polycarbonate-ABS sampler tool body fabricated using Stratasys FDM technology, five aluminum nozzles, and five rubber grommets to hold the nozzles. The filter cap assembly

completes the enclosure of the sampler tool body and is composed of the filter cap made of the same material as the sampler tool body, four optional filters fit to the filter cap windows, and four filter retaining screens.

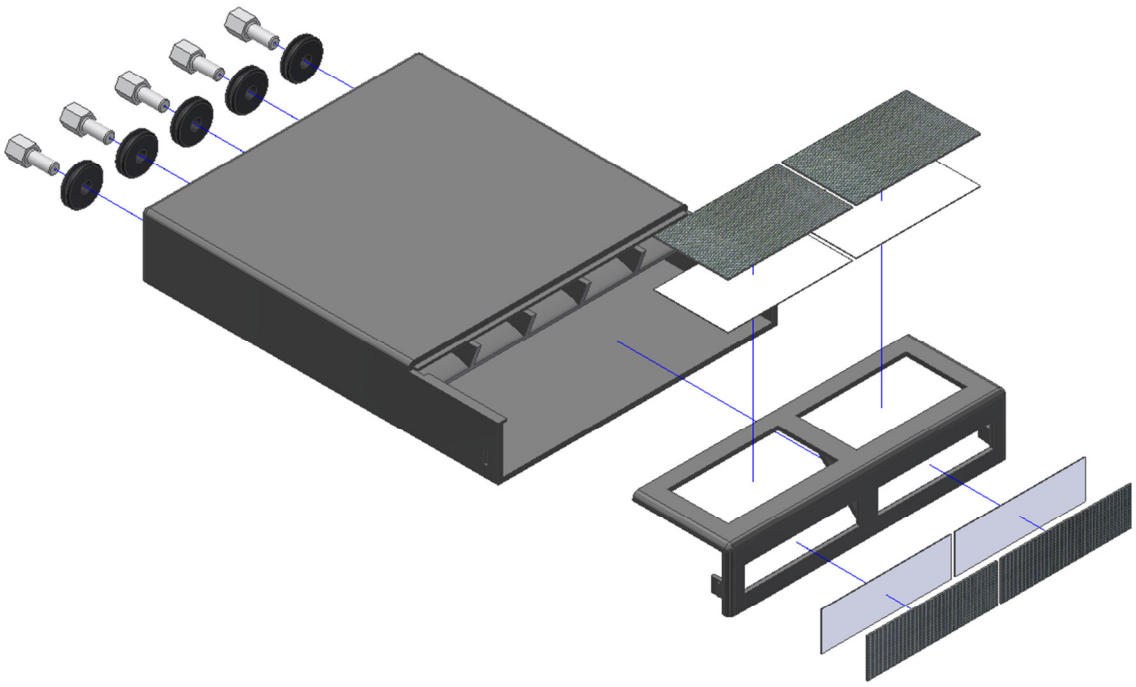

Figure 5.3: Sampler Tool – Exploded View

Like the jet impingement test rig, the sampler tool can be broken into three sections that are labeled in Figure 5.4: the sampling chamber, the ramp, and the collection chamber.

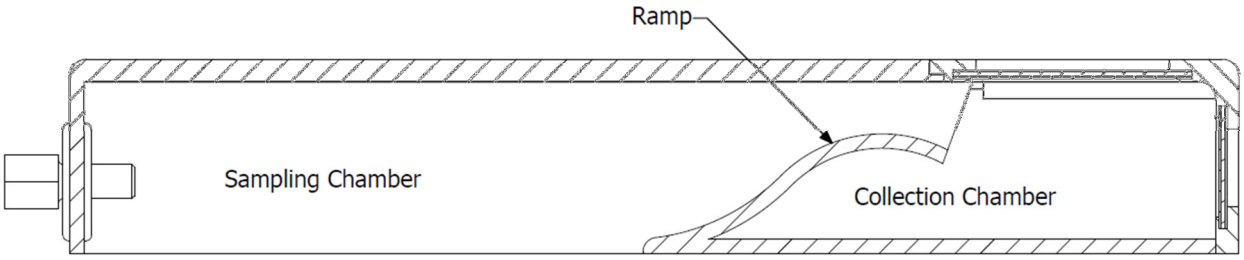

Figure 5.4: Basic Sampler Tool Diagram

The sampling chamber is where the particle entrainment actually occurs, so its geometry plays an important role. From the observations made in Section 4.5 regarding jet interferences, it

was decided to design each nozzle with its own channel as illustrated by Figure 5.5, where the top of the sampler tool body has been removed in order to show the separated flow channels. By dividing the sampling chamber into five separate flow channel, the air jets will be isolated from one another, eliminating jet interferences and, therefore, reducing interparticle collisions and unwanted recirculation.

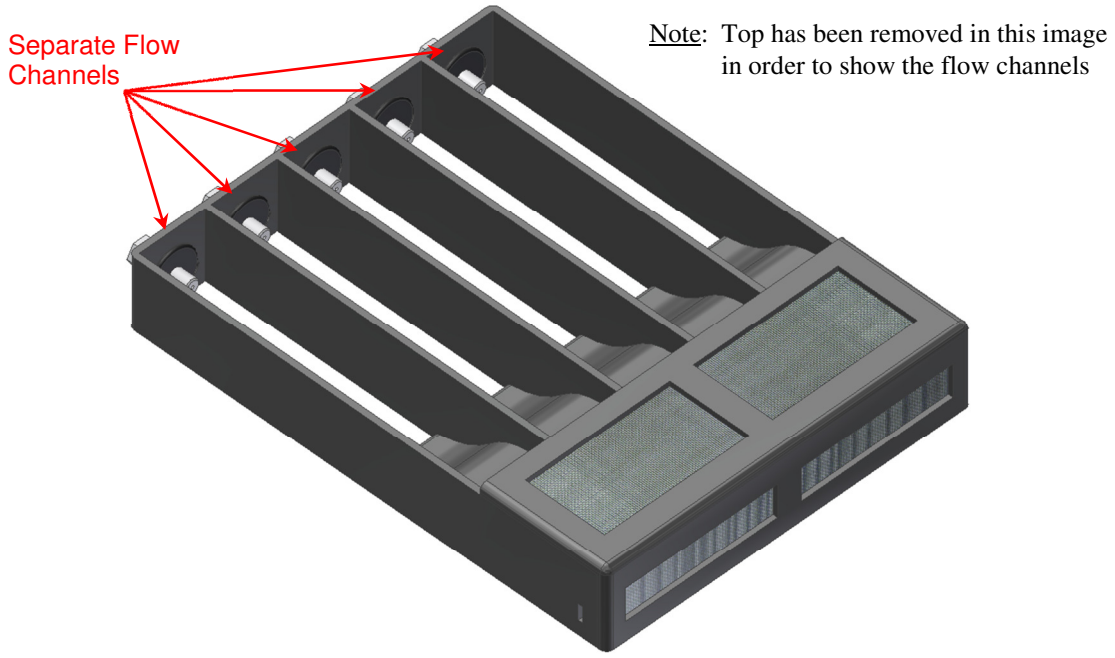

Figure 5.5: Sampler Tool Flow Channels

The sampler body also utilizes supplemental intakes beneath each of the nozzles to aid in particulate entrainment. Shown in Figure 5.6, the supplemental intakes are designed to utilize the Venturi effect[15] and pull air into the chamber, thereby causing an in-rush of air that will entrain particles directly beneath the nozzle where the air jet would otherwise miss.

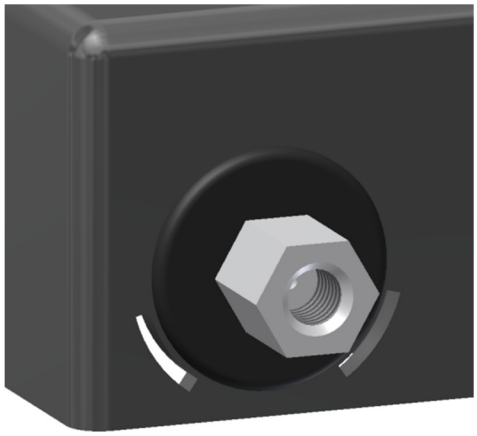

Figure 5.6: Supplemental Intakes

Once the particle is entrained in the flow, it will be transported up the ramp and into the collection chamber. Because of the observation made during the high-speed video testing, the ramp walls that angled inward as in the jet impingement test rig were eliminated, so the flow channel is straight all the way up the ramp. Additionally, the ramp was redesigned to facilitate sustaining particle entrainment. In the jet impingement test rig, a inclined flat plane was used to separate the sampling and collection chambers, and this resulted in particles hitting the ramp then slowly rolling along the surface propelled by the moving air, fighting both friction and gravity the entire way. It was hypothesized that a concave ramp would deflect the particle back into the air stream, as in Figure 5.7, so that it could more easily be transported while only having to fight gravity, and not the friction from the ramp surface. The particle is forced to bounce its way up the ramp instead, reentering a stream of higher velocity fluid with every bounce, rather than rolling up the ramp.

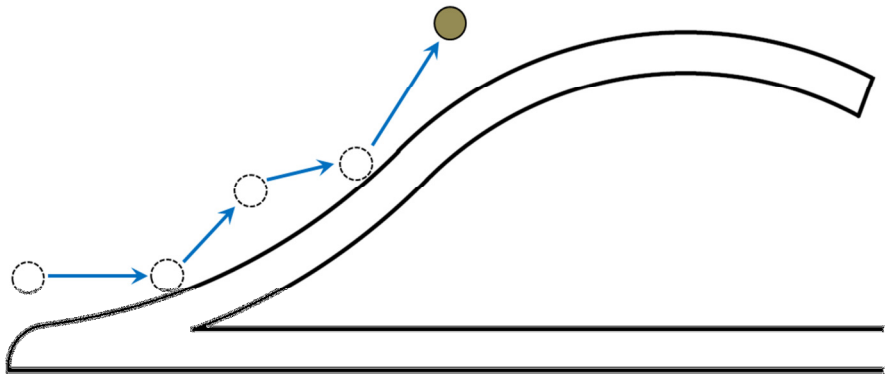

Figure 5.7: Curved Ramp Design

The ramp was also given this curvature in order to utilize the Coanda Effect discussed in Section 2.3.2. The Coanda Effect allows the fluid to cling to the curved ramp, even over the apex, and into the collection chamber.

Though the flow channels are separated in the sampling chamber, they all flow into a common collection chamber capable of holding 160cc of collected material. Placing the only downstream outlets over the collection area is what allows the air to transport the particulate to the desired location. Four exhaust ports designed to release air at a rate of 11.2scfm[1] while filtering particles larger than 5µm line the walls of the collection chamber when the filter is installed. It should be noted that, theoretically, the mass flow rate out of the sampler will be affected by the debris clogging the filter, but since the mass flow rate into the sampler will diminish over time, this affect is assumed to be negligible. The sampler can also be used without the filter paper, such that only the filter retaining screen is used to filter the particulate at the exhaust ports. The filter retaining screen has a 46.2% open area and 860µm openings (slightly larger than the vacuum sampler's 700µm openings), so the level of filtration is much lower, but the allowable flow rate is much higher.

[1] When operated with an initial pressure of 125psi, the flow rate into the sampler is 13scfm, although this flow rate decreases significantly as the air supply empties.

Currently, the filter cap uses a snap fit connection to connect to the sampler tool body enclosing the collection chamber, requiring a manually applied force to retrieve the material sample. However, a magnetic release system could easily being implemented in future design iterations.

5.2 Air Velocities

When the air is released from the nozzle into the flow channel, a compressible free-jet is formed as the high pressure air meets the low pressure atmosphere. Particles are entrained in the flow when the jet spreads and ultimately contacts the bed at a point downstream on the bed surface which can determined geometrically. Other particles are pulled into motion by the secondary fluid, the atmospheric air, entrained underneath the jet.

Two velocities then are of interest: the critical velocity of the particle and the air jet velocity, both of which will be covered in this section.

5.2.1 Critical Velocities

Recall from Section 2.3 that if the Archimedes number is known for a particle, than the critical velocity for that particle can be calculated using the equations presented by Kalman et al[6] (Equations 2.5, 2.6, and 2.7), which are based on correlations found experimentally. The equation below is Equation 2.8 solved for the critical velocity,

$$U^* = \frac{\mathrm{Re}_p^* \mu \left(1.4 - 0.8 e^{\frac{-D/D_{50}}{1.5}}\right)}{\rho d_p} \qquad \textbf{5.1}$$

Applying the findings of Kalman et al to the particles used in this study results in the critical velocity estimates shown in Table 5.2. Note that the metal BB is by far the most difficult particle to pick up because its critical velocity is more than twice that of any other particle.

Table 5.2: Estimated Particle Critical Velocities

Particle	Diameter (μm)	Density (kg/m^3)	Archimedes Number	Modified Reynolds Number	Critical Velocity (m/s)
Flour	$1< d_p <100$	800	$2.72\times10^{-5}<$ Ar <27.2	$0.660 <$ Re$_p^*$ <20.6	$2.88< U^* <9.16$
Sand	$100< d_p <1000$	2400	$81.5<$ Ar $<8,150$	$33.0<$ Re$_p^*$ <637	$4.61< U^* <8.90$
Plastic BB	6000	1100	807,000	4,560	10.6
Metal BB	4500	6900	21,400,000	6,920	21.5

There is a significant amount of variation in the values calculated for flour and sand particles which result from the significant amount of variation in their particle diameters. While incipient motion can likely be observed at very low velocities, the maximum velocity in the calculated range should be considered the target velocity to pick up that type of particle in order to ensure entrainment.

It should also be noted that in their study, Kalman et al regulated the gas velocity by increasing or decreasing the cross-sectional area of the flow while maintaining a constant flow rate, and were therefore observing the average velocity of the gas in the channel, not the velocity precisely at the particle bed surface. This critical velocity, then, is an average critical velocity across the profile of the flow.

With the critical velocity of each type of particle known, it is necessary to ensure that the velocity of the air jet will be high enough to match.

5.2.2 Air Jet Velocity

The air exits the air supply and enters the sampler's flow channels through a 1.2mm diameter circular square-edged orifice. As mentioned earlier, the flow is choked because of the high upstream to downstream pressure ratio, thus the jet velocity is equal to that of the speed of sound until the upstream pressure drops to roughly twice the downstream pressure. The Reynolds number at the nozzle exit is approximately 26,000, indicating a highly turbulent free jet.

Although the air velocity is sonic at the jet exit, the jet velocity will decay rapidly further away from the exit. Because the same mass of air is spreading in a conical geometry, the air velocity must decrease to maintain the same mass flow rate. At any given point in the streamwise direction of the jet, the centerline will have the highest velocity and the velocity profile will be theoretically axisymmetric about that centerline.

The centerline velocity, U_c, is a function of the distance, x, from the nozzle exit in the streamwise direction for a compressible jet with $\mathrm{Ma} = 1$. It is a fraction of the exit velocity as shown by the equation[16]

$$U_c(x) = U_j \left[1 - \exp\left(\frac{-1}{0.1344\bar{\rho}^{0.28}\frac{x}{d} - 0.7} \right) \right] \qquad \textbf{5.2}$$

where $\bar{\rho}$ is the ratio of the density of the air at the jet exit to the atmospheric air, which is unity for the current application. The jet velocity, U_j, is the local speed of sound because it is choked, and is calculated by

$$U_j = c = \sqrt{\frac{kP_{atm}}{\rho}} = \sqrt{\frac{(1.40)(94{,}180\text{Pa})}{1.11\,\frac{\text{kg}}{\text{m}^3}}} = 345\text{m/s}$$

The distance, x, from the jet exit at which the air jet cone will impact the particle bed can be computed geometrically. The jet divergence angle is generally assumed to be 20°, or 10° from center, for a turbulent free jet[17]. Therefore, the distance from the jet exit at which the jet will first contact the particle bed for a jet ½" above the surface of the bed is

$$x = \frac{0.50\text{in}}{\tan 10^\circ} = 2.8\text{in or } 0.072\text{m},$$

and the geometry of the jet in the flow channel is depicted in Figure 5.8. It should be noted, however, the clean spread of the jet shown in Figure 5.8 is not characteristic of a turbulent free jet. In actuality the jet would be lined with eddies and a boundary line would be virtually impossible to distinguish. The jet's divergence cone is shown as it is in order to quantify the dimensions of interest within the chamber.

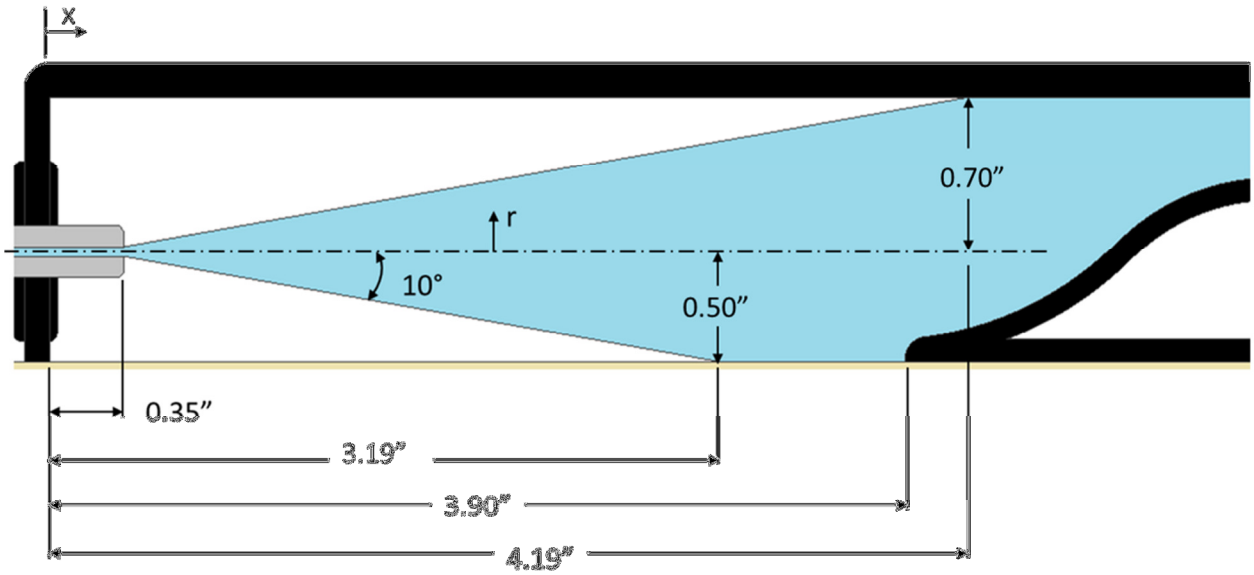

Figure 5.8: Jet Divergence and Flow Channel Geometry

Then, in order to calculate the velocity at the centerline of the jet, Equation 5.2 is used with a 1.2mm orifice diameter, such that

$$U_c(x) = (345\text{m/s})\left[1 - \exp\left(\frac{-1}{0.1344(1)^{0.28}\frac{(0.072\text{m})}{(0.0012\text{m})} - 0.7}\right)\right] = 44\text{m/s}\ .$$

The radial distribution of the velocity, $U(r)$, at a distance, x, from the jet exit is then in turn expressed as a fraction of the centerline velocity dependent upon the radial distance from the centerline, r,[17]

$$U(r) = \frac{U_c}{10^{40\left(\frac{r}{x}\right)^2}} \qquad \textbf{5.3}$$

so that at the point at which the jet first impacts the particle bed, $x = 2.8$ in, the velocity profile is as shown in Figure 5.9.

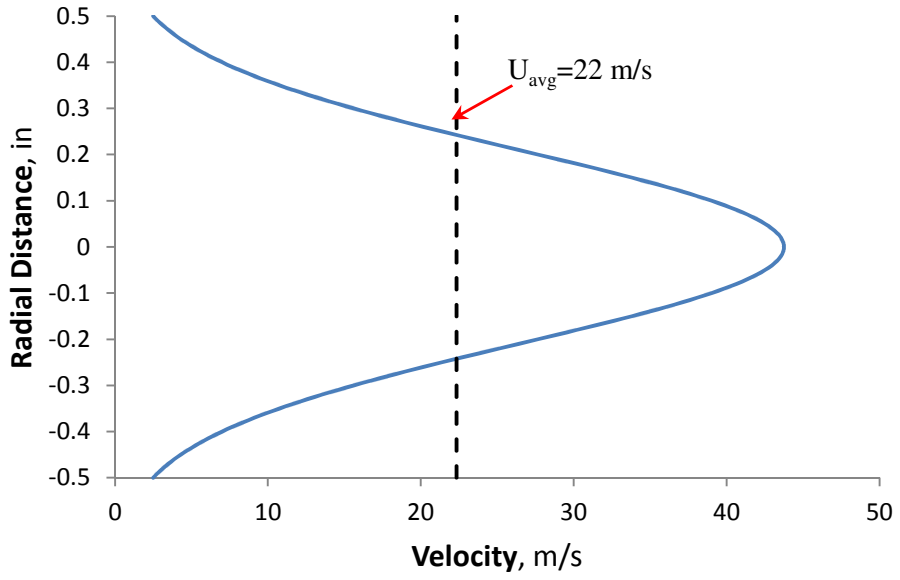

Figure 5.9: Air Jet Velocity Profile

In order to correlate this theoretical velocity profile to the critical velocities calculated in Section 5.2.1, an average air velocity was found because, as noted previously, the velocities

observed in the experiments of Kalman et al were average velocities based on flow rate measurements. The average velocity at a distance of 2.8" (0.072m) from the jet exit, which is just before where the jet will impact the particle bed, is 22 m/s. A key assumption made here is that the turbulence and effects of secondary fluid entrainment will cause the velocity profile in Figure 5.9 to more closely resemble that of the flow used in work of Kalman et al, from where the ciritical velocity correlations come.

Additionally, the Venturi effect will cause the surrounding atmospheric air to be entrained along into the jet as a secondary fluid. The volumetric rate of entrainment, Q_{sf}, of the secondary fluid is quantified by the equation[17]

$$Q_{sf} = \left(0.32\left(\frac{x}{d}\right)\cdot Q_j\right) - Q_j \qquad \textbf{5.4}$$

where Q_j is the flow rate of the air in the jet which is calculated to be 1.25×10^{-3} m^3/s by

$$Q_j = \frac{\dot{m}}{\rho} \qquad \textbf{5.5}$$

where $\dot{m}$ is the mass flow rate found using Equation 3.3.

Considering the area occupied by the jet to be negligible will provide a conservative estimate for the velocity of the secondary fluid as it is entrained, so the area of the entire flow channel was used to extract the velocity from the secondary fluid entrainment flow rate. The linear relationship between the distance in the streamwise direction and the secondary fluid entrainment velocity is illustrated by the plot in Figure 5.10. The velocity is only plotted up to a distance of 1.5" from the jet exit which is well short of where the jet contacts the particle bed because Equation 5.4 assumes the jet is a completely free jet and no obstructions will limit the air

entrainment rate, and therefore, error would increase with distance when used in a bounded volume like the sampler's flow channel.

A line indicating the minimum critical velocity of all the particles used in this study, that of the smallest flour particles, is overlaid on the plot in Figure 5.10 in order to show the point at which particles will begin to be picked up by the motion of the atmospheric air resulting from secondary fluid entrainment. It indicates that the smallest of the flour particles will begin to be entrained as early as 0.3" downstream of the jet exit. Furthermore, because the velocity of the secondary fluid increases linearly with distance, this plot demonstrates that it is possible that some of the sand and plastic BBs are being picked up before the jet ever even impacts the bed.

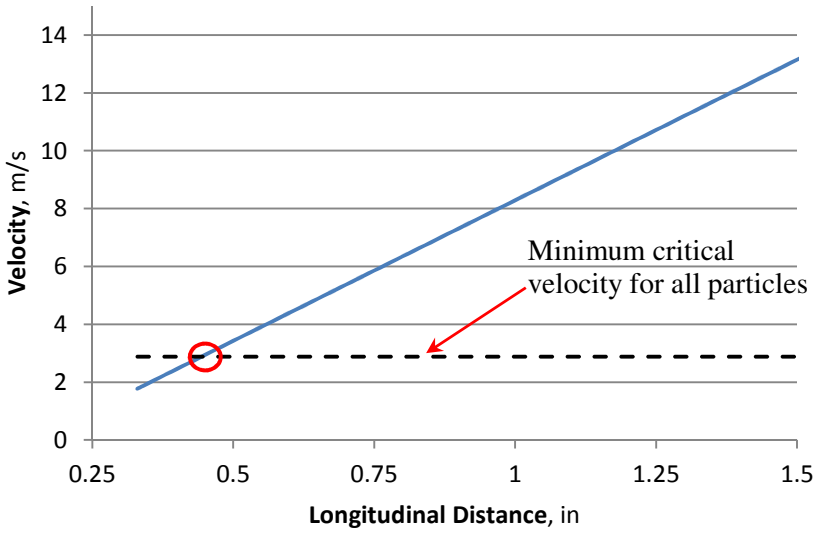

Figure 5.10: Average Velocity of Secondary Fluid Entrained by the Air Jet

Since this air velocity right before the jet impacts the particles is 22 m/s and is greater than the critical velocity of each particle used in this study (recall from Table 5.2 that the metal BB had the highest critical velocity at 21.5 m/s), it is expected that the sampler is capable of collecting each type of particle. Additionally, with the implementation of the supplemental

intakes, secondary fluid entrainment allows the pickup of smaller particles before contact with the particle bed is even made. Certainly, testing of the final design is necessary to confirm this hypothesis and to evaluate its performance.

5.3 Final Design Evaluation Testing

This section will first present the test setup used to conduct a laboratory evaluation of the sampler. Then, the results of the evaluation will be presented and discussed. General observations made during the evaluation will be organized in the final subsection.

5.3.1 Bench Test Evaluation

To evaluate the final design of the pneumatic particulate sampler, a particle bed was created by filling a 7.5" × 10.5" box with a 1.68kg of the debris sample mixture outlined in Section 4.1, an amount equivalent to 24 of the 70g samples used in the jet impingement testing. The depth of the particle bed is approximately 0.75". Figure 5.11 shows a photograph of this particle bed.

Figure 5.11: Particle Bed

The sampler tool was placed on top of the particle bed as in Figure 5.12 and situated into the bed such that no crevices were left under the sampler walls for air to leak out. Next, the air supply was filled to 120psi because the valves were found to be unable to retain a pressure any higher. Once filled, a power supply was used to trigger the five valves simultaneously by providing them each with a 12V signal until the entire air supply tank had been purged.

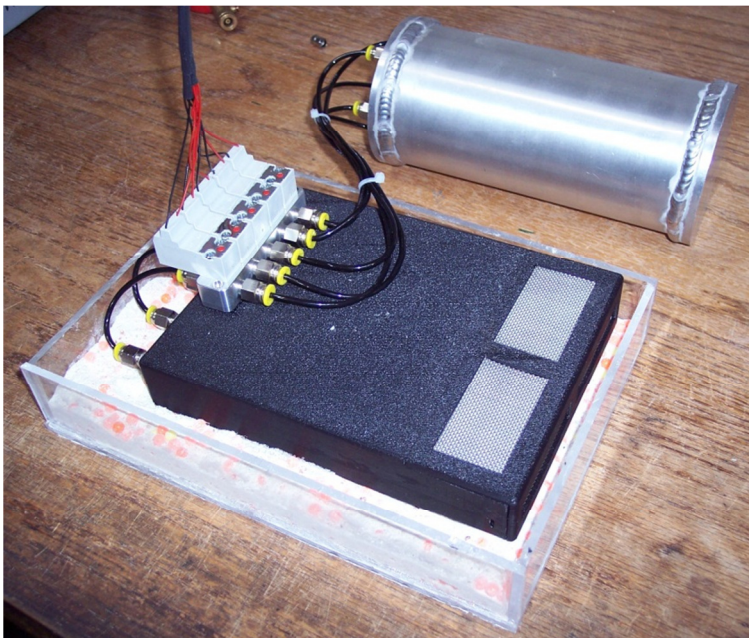

Figure 5.12: Final Design Evaluation Testing

After a single trial was run, the collected sample was sorted into fine particulate, plastic BBs, and metal BBs. To eliminate the error in volume measurement, the volume of the sample collected was determined by measuring the mass of the each sample and converting to volume with the materials' known densities. The mass of the fine particulate was divided by the bulk density to determine the volume, while for the plastic and metal BBs, the mass collected was divided by the absolute density because it was assumed that the fine particulate is small enough to completely fill the space between the BBs.

The sampler's performance was tested both with the filter paper and with only the retaining screen installed in the four rectangular exhaust ports. The smaller particles composing the fine particulate mixture are unable to be collected without the filter, but a significant increase in total material collected is observed as seen in Figure 5.13.

After five trials with the filter installed and five trials with just the screen, the average volume of material collected when using only the screen is 54cc of total material with a standard deviation of 5.7cc, while the filter provided for an average total material collection of 35cc and a 4.1cc standard deviation. With the filter in place, air flow out of the flow channel is restricted through the exhaust ports, so air leaks at a higher rate out of the sides of the sampler before having a chance to transport particles into the collection chamber. However, the advantage to having the filter in place is that smaller particles which can easily pass through the screen are held in the filter. Depending on the application, finer particles may be desirable, in which case a filter would be necessary.

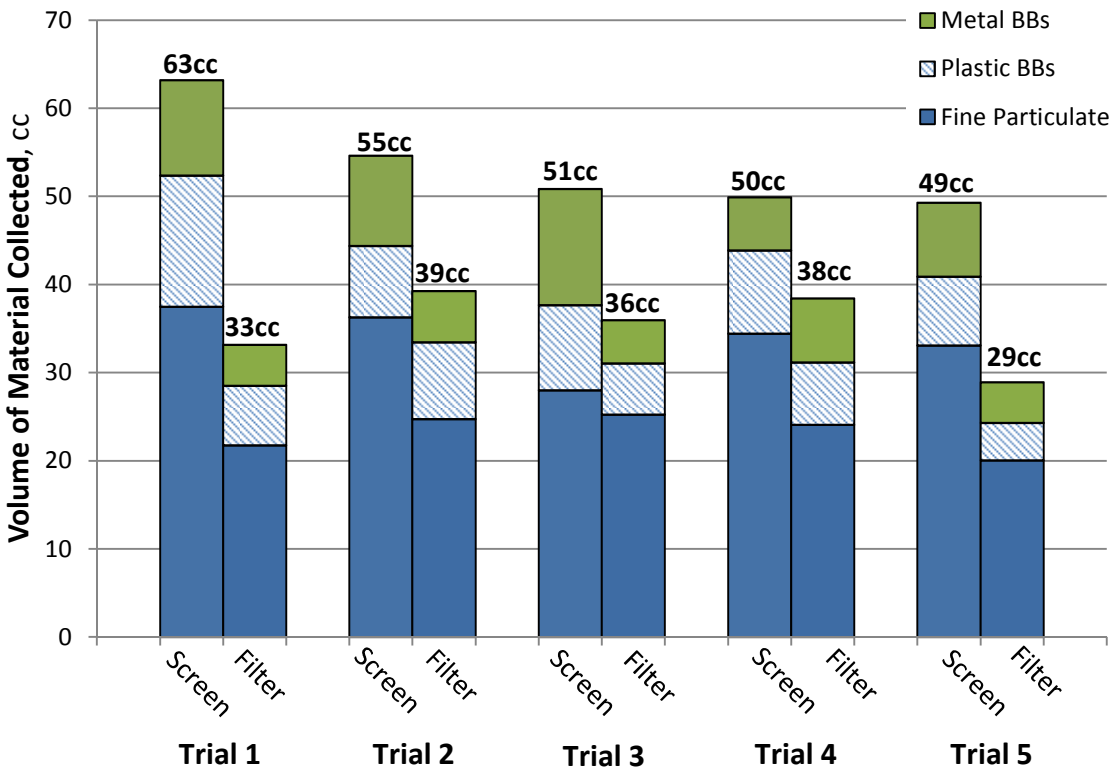

Figure 5.13: Bench Test Results

Recall the material composition used in this study is outlined in Figure 4.1.

A simple conversion between volume and mass can be performed for the debris mixture to find the mass of a particular volume collected or the volume of a particular mass collected. To do this, one must simply use the density of the material, but more accurately, one must use the absolute density of the plastic and metal BBs, 1.1 g/cm^3 and 6.9 g/cm^3, respectively, and the bulk density of the fine particulate mix, 1.35 g/cm^3. The absolute density is used as the conversion factor for the BBs because it is assumed that the fine particulate will completely fill the voids between them when mixed.

A depth test was also performed just as described in Section 4.4 for the final design, and it was found that the sampler collects only trace amounts from greater than ½" deep.

5.3.2 Field Test Evaluation

As seen in Figure 5.14, the pneumatic sampler was then tested without the filter on two surfaces likely to be found in an urban environment: the hood of a car (left) and flat concrete (right). A 1/16" thick layer of *fine particulate only* was spread onto the surface to be used as the particle bed. Five trials with a gasket adhered to the bottom of the sampler, as seen in Figure 5.15, and five trials without it were conducted at each test setting. The results of the testing are summarized in Table 5.3.

Figure 5.14: Field Test Setups

Table 5.3: Field Testing Results

	Car Hood		Concrete	
Trial	w/ Gasket *(g)*	w/o Gasket *(g)*	w/ Gasket *(g)*	w/o Gasket *(g)*
1	11.6	10.4	11.0	12.1
2	10.6	12.2	12.2	10.7
3	11.4	10.8	14.2	11.4
4	14.6	10.0	12.4	11.5
5	11.0	10.4	13.3	12.9
Average:	**11.8**	**10.8**	**12.6**	**11.7**
Std Dev:	**1.6**	**0.9**	**1.2**	**0.8**

It can be observed that on each test surface the gasket provides a slight improvement in performance. Furthermore, one would expect that a rougher surface would make it more difficult to collect particles because particles would be caught in the crevices that cause the roughness, but this is not the case according to the data. It is likely that sampler performed better on the concrete surface because, though much rougher, it was more level than the car hood. Even at its flattest point, the car hood has a notable curvature that makes it difficult to lay the flat surface of the bottom of the sampler squarely on it.

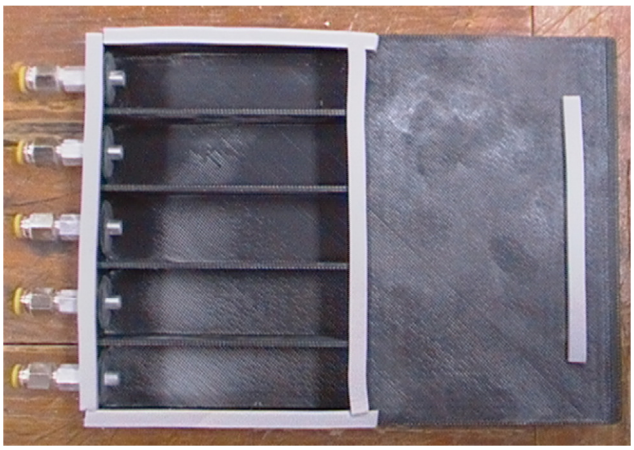

Figure 5.15: Gasket Adhered to Bottom of Sampler Tool

The mass measurements from Table 5.3 correlate to 8.7cc average collection from the car hood with the gasket and 8.0cc without it, and 9.3cc on the concrete with the gasket and 8.7cc without it. It is important to remember that this testing was conducted with only fine particulate and a very thin particle bed, approximately 1/16" deep, so the results vary significantly from the results presented earlier from the bench testing on the thick particle bed.

The amount of particulate material exposed to the sampling chamber in this testing was 22.5cc or 30.3g, so he sampler consistently collected more than a third of the material that it possibly could have.

5.3.3 Observations During Testing

The pneumatic particulate sampler was successful in the bench and field testing, although it has not yet been tested onboard the robot. One recurring issue during testing was the quality of the seal the sampler makes with the particle bed. In the bench testing, the particle bed was so thick that the sampler could be dug down into it easily, thereby creating an ideal seal such that no air from the jets leaked out of its respective flow channel or the sides of the sampler altogether. In the field tests however, the particle bed was much thinner, and so a good seal was more difficult to achieve.

Consider the photograph taken after a test on the car hood with the gasket installed on the bottom of the sampler. Where the air jet escaped the sampler is highlighted in red. Even with the foam gasket installed to improve the seal with the particle bed, air is able to escape, greatly diminishing the efficiency of the system.

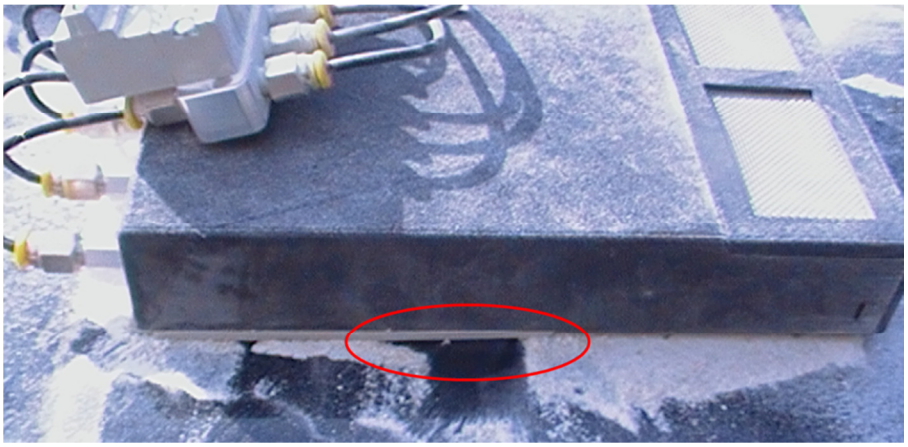

Figure 5.16: Poor Seal with Particle Bed

5.4 Final Design Specifications

The pneumatic sampler meets the design goal of collecting 50cc of particulate material from the top 5/8" debris. In addition, it is sized to fit on the robot's payload tray, so robotic implementation is feasible. Recall from Section 1.2 that the robot's payload tray constrains the sampler design to a 10.5" × 10.5" × 5.5" envelope. Figure 5.17 shows the layout for the payload tray with the particulate sampler installed. It involves a cutout on the carbon fiber plate when this sampling system is installed to allow for the sampler tool to drop conveniently to the ground to sample.

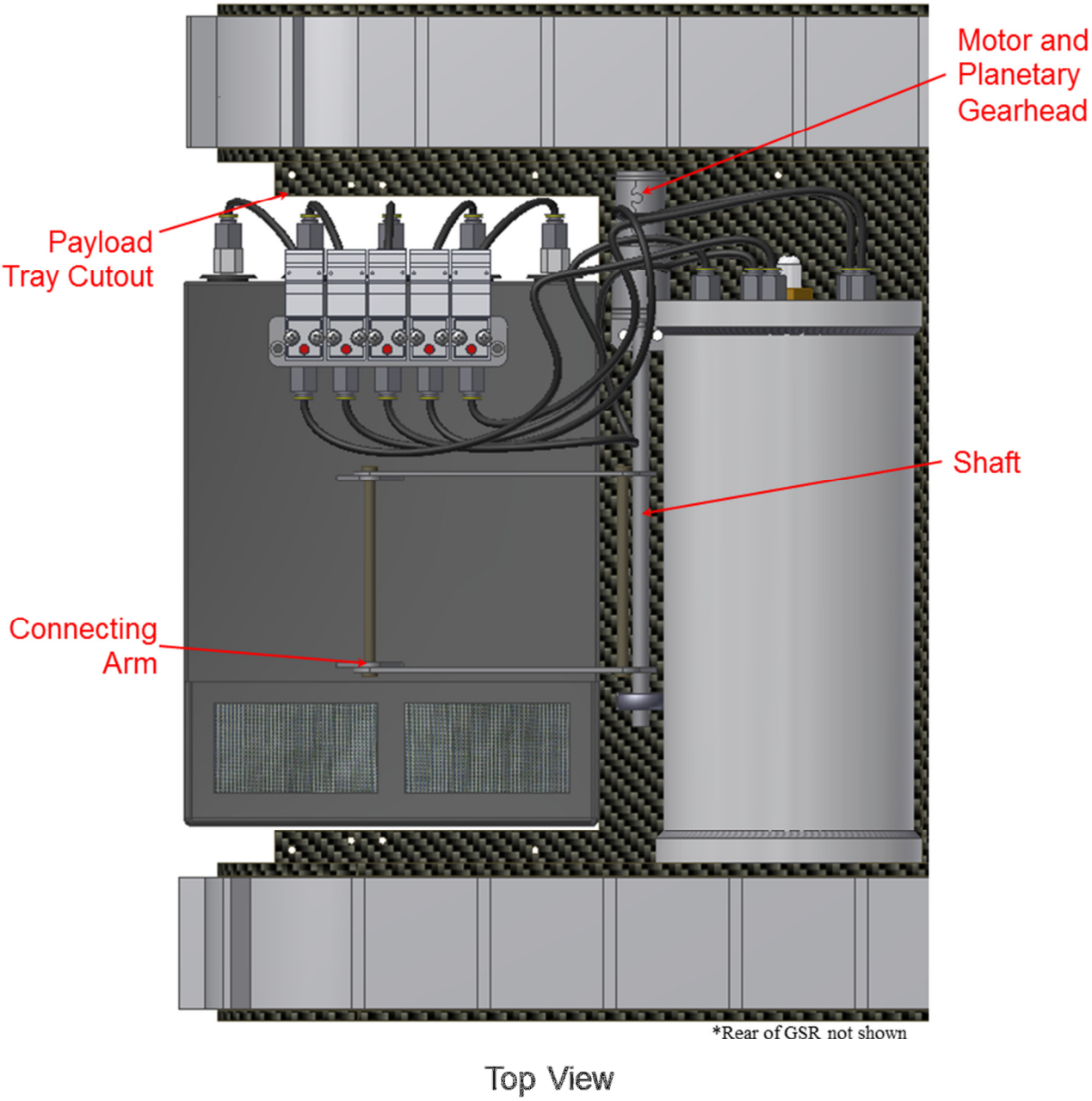

Figure 5.17: Onboard Layout

A small motor and gearhead assembly with a shaft extension to the output is shown between the air supply and the sampler tool. Connecting arms links the sampler to the shaft to allow the system to lower the sampler as the motor is turned as seen in Figure 5.18.

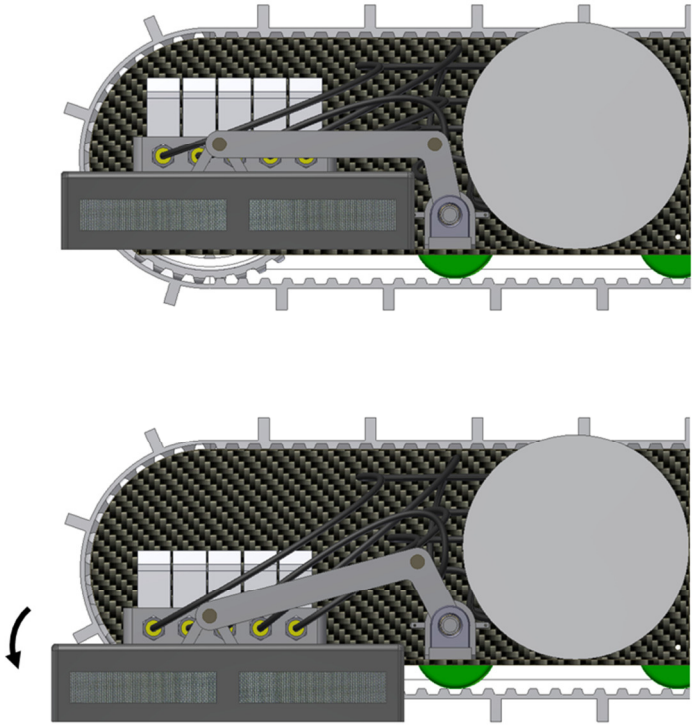

Figure 5.18: Articulation of Pnuematic Sampler Tool

Also recall from Section 1.2 that the target weight of the system is 5.2 lbs.

Table 5.4 lists the weights of the current prototyped and recommended systems. While both allow for a sufficient weight allotment to the articulation system, the recommended system, which has been shown feasible in this thesis, offers a 46% reduction in total weight. The recommended design involves the recommended air supply from Section 3.2.2 and the recommended valves from Section 5.1.1.

Table 5.4: Final Design Weight

	Weight	
	Current System *(lbs)*	Recommended System *(lbs)*
Air Supply	1.90	0.65
Valve Assembly	0.77	0.43
Sampler	0.75	0.75
Total:	3.42	1.83

Chapter 6

Conclusions and Recommendations

Presented in this thesis is the work and research performed to develop a novel pneumatic particulate collection system. The current application placed a unique set of criteria on the design of this system, and a feasible solution has been set forth. It has been shown in this thesis that a pneumatic sampler design can effectively collect heavier particles than a vacuum design with a fraction of the electrical power consumption. The pneumatic sampler is much simpler from a user standpoint in that, a simple sequence must be activated to lower the sampler to the ground and release the air that entrains the particles, whereas with a vacuum sampler, great effort is required on the user's part to control a robotic manipulator to move the vacuum intake into position. With the pneumatic design, particulate from only the top 5/8" of a layer of a particle bed is able to be collected.

A detailed summary of the work completed and suggestions for future work are laid out in this chapter.

6.1 Summary of Work

A demand exists for a system to be implemented onboard a lightweight robot to be used to collect particulate debris from a hazardous environment. A set of design specifications for the collection system were established based on mission objectives and the dimensions and weight limitations of the robot on which the system is to be implemented. These specifications were that the system was to weigh less than 5.2 lbs and fit within the 10.5" × 10.5" × 5.5" available space in the payload tray of the GSR. It was to be capable of collecting from the top 5/8" thick layer of debris in a particle bed, and it was to be capable of collecting 50cc of particulate.

It is proposed in this thesis that pneumatic system could be a viable alternative to a vacuum sampler design. The pneumatic system offers the benefit of decreased onboard electrical power consumption by using the kinetic energy associated with the release of compressed air to transport particles to a collection area, rather than using valuable battery power to run a motor that turns an impeller creating suction as in a vacuum sampler. Specifically, a vacuum sampler was found to consume 2,000J of electrical energy to collect 50cc of material, while the pneumatic sampler collected the same amount of material using only 40J of electrical energy.

To achieve this functionality with this novel design, it was necessary to investigate previous work in order to understand particle motion in a gaseous medium, and so a literature review of particle entrainment was conducted. A force balance method of modeling was investigated for both incipient motion and saltation of particles. It was discovered the bed-load statics, how particles are situated in the bed and the forces that hold them there, is a significant factor in particulate transport. Experimental work was discovered in the literature that closely pertains to the work being done in this study. Equations found from this experimental work were

used to calculate the velocity of a gas flowing over a particle bed at which the particles would be entrained. This velocity is called the critical velocity of the particle.

Next, in order to design a completely portable pneumatic system, an air supply tank needed to be designed to provide the pneumatic system with the compressed air it needed. To accomplish this, the pressure transient of the air supply was first modeled by combining the ideal gas law and the equation for isentropic expansion of an ideal gas, solving for the mass, differentiating with respect to time to find the flow rate, and setting the resulting expression equal to the flow rate of the choked flow equation. Then, with a thorough understanding of how the changing pressure in the supply will affect the flow over time, an appropriate tank volume and pressure were selected and a prototype of the air supply was fabricated. From there, FEA was conducted on theoretical air supply designs to demonstrate the effect of pressure vessel head ratios on supply volume and weight. A final recommended air supply tank design able to contain $119in^3$ of air (an increase of more than 50% over the prototype that was proven to work) and weighing only 0.65 lbs was presented.

Then, a summary of the heuristic approach taken to investigate pneumatic particulate collection for the current application was given. The composition of the particulate debris used in the experimentation was described in detail, and experimental evaluation of an existing vacuum sampler design was conducted. Given two general forms of pneumatic particulate collection, jet impingement and particle entrainment, the former was investigated experimentally and deemed highly effective at collecting particulate debris in a laboratory test environment. A configuration was discovered in which 95% of the debris within its reach was successfully collected, but it was determined that this method was too aggressive, sampling too deep into the particle bed and lifting the sampler off of the ground allowing air and finer material to escape.

Thus, the particle entrainment method of particle collection is preferred because this method involves directing jets overtop of the particle bed rather than into it, thereby reducing the depth of sampling and eliminating the reactionary forces that lift the sampler off the ground. A high speed video analysis of the two collection methods exposed design flaws in the experimental test rig that created jet interferences and recirculation that had an adverse effect on particle collection. These issues would ultimately be addressed in the final sampler design.

Finally, a pneumatic sampler was developed that utilizes the particle entrainment method. The air jets' velocities were quantified using equations for free jet velocity decay over distance and divergence. The velocity at which the jet impacts the particle bed was manipulated to match the critical velocity of the particles by positioning the jet outlet appropriately. The prototyped design weighs only 3.42 lbs, and a recommended system design is presented that would reduce the weight to only 1.83 lbs. The system performs very well in thick particle beds, collecting an average of 54cc with a standard deviation of only 5.7cc when the sampler tool can be situated snuggly in the particle bed. When tested in field environments with thinner particle beds, the sampler still collected sufficient amounts of particulate, but air was found to leak out the bottom of the flow channels, taking valuable particulate with it.

6.2 Suggestions for Future Work

This thesis has collected a great deal of useful information regarding particulate sampling and has proved the feasibility of a novel approach to particulate sampling in lightweight applications. However, there are still some areas in which future work is needed to ready the system for field deployment. During the field and bench testing of the final design, a number of

design deficiencies showed themselves, the first of which is the seal that the sampler makes with the particle bed. While the inconsistencies in the particle bed are an unavoidable obstacle in particulate collection, an effort could be made to reduce the effect they have on the sampler's performance. The addition of a gasket around the bottom of the sampler tool did improve the performance of the sampler, but evidence of air escaping out the bottom was still present. Eliminating completely the possibility of air escaping the sampler anywhere but through the exhaust ports will greatly increase the system efficiency.

Another deficiency in the sampler design was the roughness of the rapid prototyping material. FDM systems inherently produce rough surfaces on the parts they produce because of the very method by which they produce them. While FDM is an extremely convenient and viable option for low quantity production, the sampler would likely perform even better with smoother flow channel surfaces, namely the ramp surface. Currently, the ramp surface in laden with ridges from the FDM process, which not only traps fine particulate before it reaches the collection chamber, making those particles inaccessible later, but also provide unwanted friction, further reducing the velocity of the fluid passing over them and therefore impeding particle collection.

Relating closely to this point is the issue of an optimal ramp design. While the ramp was given curvature in the final sampler design as opposed to the incline flat plane design of the jet impingement test rig, further work could be done to optimize the ramp design. The steeper the ramp is, the more difficult it will be to transport particles up it. However, if it is not steep enough, then there will not be enough height to the collection chamber to contain a sufficient debris sampler volume.

Filter selection is another area in which future work would benefit the performance of the pneumatic sampler. The pneumatic sampler was tested with filter paper rated to trap particles larger than 5 microns, as well as with a screen that would not trap particles smaller than 860 microns. Somewhere in between these two filters lies a solution that could provide ample thru-flow while still restricting the release of very fine particles.

Because it was found that jet impingement sampling dove too deep into the particle bed to be considered an option for the final sampler design, particle entrainment was investigated and found to work well. However, when the particle bed is not thicker than 5/8", it can be assumed that all the material in the bed is desirable, and, assuming enough force can be applied to the sampler to resist lifting, jet impingement again becomes an attractive sampling method. Therefore, it is suggested that a system be researched in which the angle of attack of the jet array can be adjusted via servo manipulation. By adjusting the angle of attack slightly, the jet would impact the particle bed farther from the ramp, increasing the material available for collection. Although, along with this added feature comes a series of design issues to tackle. For example, the force to apply to avoid the sampler being lifted from the surface would need to be determined. Also, the appropriate angle of attack be adjusted in a given scenario is necessary to be known.

Finally, one must recall that the nozzles in this thesis were actually fabricated and modeled as simple square edged orifices. It is strongly recommended that an effort be made to investigate the impact of various nozzle designs on particle entrainment. With improved nozzle designs, the air could be used more efficiently in the current application, such that more of the air released is used to transport the particulate. For example, air knives may be an interesting device

to consider as a replacement for the current orifice configuration because they create wide streams of high velocity air with minimal spread in the radial direction.

Currently, the pneumatic particulate sampler is an effective tool for use in lightweight robotic material sampling. By exploring and implementing these changes in a calculated manner, the pneumatic sampler design can be made more efficient and ready for field deployment.

Bibliography

1. Rose, M.S., *Design of a Helicopter Deployable Ground Robotic System for Hazardous Environments*, in *Mechanical Engineering*. 2010, Virginia Polytechnic Institute and State University: Blacksburg, VA. p. 140.
2. Coleman, S.E. and V.I. Nikora, *A unifying framework for particle entrainment.* Water resources research, 2008. **44**(4): p. W04415.
3. Shields, A., *Anwendung der Aehnlichkeitsmechanik und der Turbulenzforschung auf die Geschiebebewegung*. 1936.
4. Phillips, M., *A force balance model for particle entrainment into a fluid stream.* Journal of Physics D: Applied Physics, 1980. **13**(2): p. 221-33.
5. Fletcher, B., *The incipient motion of granular materials.* Journal of Physics D: Applied Physics, 1976. **9**(17): p. 2471-8.
6. Kalman, H., et al., *Pickup (critical) velocity of particles.* Powder Technology, 2005. **160**(2): p. 103-113.
7. Bagnold, R.A., *The Physics of Blown Sand and Desert Dunes*. 1941, London: Methuen and Co. Ltd. 265.
8. Kalman, H., *Attrition of powders and granules at various bends during pneumatic conveying.* Powder Technology, 2000. **112**(3): p. 244-250.
9. Munson, B.R., D.F. Young, and T.H. Okiishi, *Fundamentals of Fluid Mechanics*. 5th ed. 2006, USA: John Wiley & Sons, Inc. 770.
10. Rasouli, F. and T.A. Williams, *Application of Dispersion Modeling to Indoor Gas Release Scenarios.* Air & Waste Management Association, 1995. **45**(3): p. 191-5.
11. Megyesy, E.F., *Pressure Vessel Handbook*. 6th ed. 1983, Tulsa, OK: Pressure Vessel Handbook Publishing, Inc. 469.
12. *KIBOKO® Lightweight Pressure Vessels and Cryogenic Tanks*. 2008 [cited 2010 Sept. 2]; Available from: http://www.ctd-materials.com/products/tanks.htm.
13. Panitz, T. and D.T. Wasan, *Flow attachment to solid surfaces: The Coanda effect.* AIChE Journal, 1972. **18**(1): p. 51-57.
14. Clippard Instrument Laboratory, I., *Minimatic Catalog*. 2006, Clippard Instrument Laboratory, Inc. p. 211-6.
15. Casalmir, D.P., S. Kumar, and F. Higuchi, *Particle Entraining Eductor-Spike Nozzle Device for a Fluidized Bed Jet Mill*. 2005, Xeros Corporation: US.

16. Witze, P.O., *Centerline Velocity Decay of Compressible Free Jets.* AIAA Journal, 1974. **12**(4): p. 417-8.

17. Perry, R.H. and D.W. Green, *Perry's Chemical Engineers' Handbook (7th Edition)*. 1997, McGraw-Hill.

18. ASCO Valve, I., *2 and 3-Way Minature Solenoid Valves*. 2010, ASCO Valve, Inc. p. 31-4, 57-59.

Appendices

Appendix A

Pressure Transient Derivation

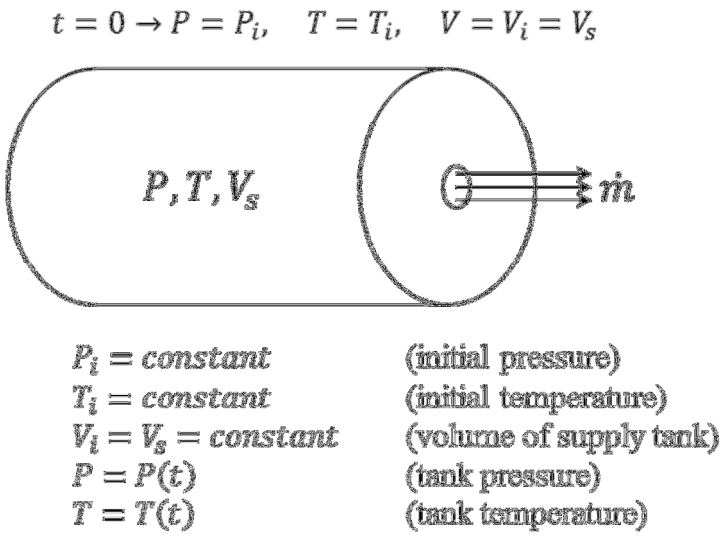

Figure A.1: Pressure Transient Problem Definition Diagram

Ideal gas law:

$$PV_s = m\frac{R_g}{M}T \qquad \textbf{A.1}$$

$$\Rightarrow m = \frac{PV_sM}{R_gT}$$

Equation for isentropic expansion of an ideal gas:

$$\frac{T_i}{T} = \left(\frac{P_i}{P}\right)^{\frac{k-1}{k}} \qquad \textbf{A.2}$$

Writing $T(t)$ as $T\big(P(t)\big)$ gives

$$\Rightarrow T = T_i P_i^{\frac{1-k}{k}} P^{\frac{k-1}{k}}$$

Combining Equations A.1 and A.2 yields $m = f(P)$,

$$m = \frac{PV_sM}{R_gT_iP_i^{\frac{1-k}{k}}P^{\frac{k-1}{k}}} = \frac{V_sM}{R_gT_iP_i^{\frac{1-k}{k}}}\left(\frac{P}{P^{\frac{k-1}{k}}}\right) = \left(\frac{V_sM}{R_gT_iP_i^{\frac{1-k}{k}}}\right)P^{\frac{1}{k}}$$

$$\Rightarrow m = const \cdot P^{\frac{1}{k}}$$

Differentiating the mass of the air inside the tank with respect to time yields,

$$\dot{m}(t) = \frac{const}{k} P^{\frac{1-k}{k}} \cdot \frac{dP}{dt}$$

so, from the Ideal Gas Law and isentropic expansion,

$$\dot{m}(t) = \left(\frac{V_sM}{kR_gT_iP_i^{\frac{1-k}{k}}}\right)P^{\frac{1-k}{k}} \cdot \frac{dP}{dt} \qquad \textbf{A.3}$$

Now, consider the critical flow equation

$$\dot{m}(t) = CA\sqrt{k\rho P\left(\frac{2}{k+1}\right)^{\frac{k+1}{k-1}}} \qquad \textbf{A.4}$$

Since $\rho = f\big(P(t)\big)$,

$$\rho = \frac{m}{V} = \frac{PM}{ZR_gT} = \frac{PM}{ZR_gT_iP_i^{\frac{1-k}{k}}P^{\frac{k-1}{k}}} = \frac{P^{\frac{1}{k}}M}{ZR_gT_iP_i^{\frac{1-k}{k}}}$$

Equation A.3 becomes

$$\dot{m}(t) = CA\sqrt{\frac{kP^{\frac{1}{k}}M}{ZR_gT_iP_i^{\frac{1-k}{k}}}P\left(\frac{2}{k+1}\right)^{\frac{k+1}{k-1}}}$$

Simplifying, and noting that the real gas compressibility factor, Z, is unity for air,

$$\dot{m}(t) = CAP^{\frac{k+1}{2k}}\sqrt{\frac{kM}{R_g T_i P_i^{\frac{1-k}{k}}}\left(\frac{2}{k+1}\right)^{\frac{k+1}{k-1}}} \qquad \textbf{A.5}$$

Both Equation A.3 and Equation A.5 are expressions of the same mass flow rate, so setting the right hand side of these equations equal to each other yields

$$\left(\frac{V_s M}{kR_g T_i P_i^{\frac{1-k}{k}}}\right)P^{\frac{1-k}{k}}\cdot\frac{dP}{dt} = CAP^{\frac{k+1}{2k}}\sqrt{\frac{kM}{R_g T_i P_i^{\frac{1-k}{k}}}\left(\frac{2}{k+1}\right)^{\frac{k+1}{k-1}}}$$

which can be solved for P,

$$P^{\frac{1-3k}{2k}}\cdot\frac{dP}{dt} = CA\sqrt{\frac{kM}{R_g T_i P_i^{\frac{1-k}{k}}}\left(\frac{2}{k+1}\right)^{\frac{k+1}{k-1}}}\left(\frac{kR_g T_i P_i^{\frac{1-k}{k}}}{V_s M}\right)$$

and simplifies to

$$\boxed{P^{\frac{1-3k}{2k}}\cdot\frac{dP}{dt} = \frac{CA}{V_s}\sqrt{\frac{k^3 R_g T_i P_i^{\frac{1-k}{k}}}{M}\left(\frac{2}{k+1}\right)^{\frac{k+1}{k-1}}}}$$

as presented in Section 3.1.

Integrating this equation from t_1 to t_2,

$$\int_{t_1}^{t_2}\left(P^{\frac{1-3k}{2k}}\cdot\frac{dP}{dt}\right)dt = \int_{t_1}^{t_2}\left(\frac{CA}{V_s}\sqrt{\frac{k^3 R_g T_i P_i^{\frac{1-k}{k}}}{M}\left(\frac{2}{k+1}\right)^{\frac{k+1}{k-1}}}\right)dt$$

$$= \left(-\frac{2k}{1-k}P^{\frac{1-k}{2k}}\right)\Bigg|_{t_1}^{t_2} = \Delta t\cdot\frac{CA}{V_s}\sqrt{\frac{k^3 R_g T_i P_i^{\frac{1-k}{k}}}{M}\left(\frac{2}{k+1}\right)^{\frac{k+1}{k-1}}}$$

where $\Delta t = t_1 - t_0$.

Denote $P(t_j)$ as P_j

$$= \frac{2k}{k-1}\left(P_2^{\frac{1-k}{2k}} - P_1^{\frac{1-k}{2k}}\right) = \Delta t \cdot \frac{CA}{V_s}\sqrt{\frac{k^3 R_g T_i P_i^{\frac{1-k}{k}}}{M}\left(\frac{2}{k+1}\right)^{\frac{k+1}{k-1}}}$$

$$P_2 = \left(\Delta t \cdot \frac{k-1}{2k} \cdot \frac{CA}{V_s}\sqrt{\frac{k^3 R_g T_i P_i^{\frac{1-k}{k}}}{M}\left(\frac{2}{k+1}\right)^{\frac{k+1}{k-1}}} + P_1^{\frac{1-k}{2k}}\right)^{\frac{2k}{1-k}}$$

Appendix B

Valve Selection Calculations

Maximum flow rate occurs at $P = P_i = 125\text{psi} = 861{,}844.66\text{Pa}$. The coefficient of discharge from a square-edged orifice is $C = 0.60$, and A is calculated by

$$A = \frac{\pi}{4} d^2$$

where $d = 1.2\text{mm}$, so that

$$A = \frac{\pi}{4}(0.0012\text{m})^2 = 1.131 \times 10^{-6}\text{m}^2$$

The local atmospheric air properties used are $k = 1.40$, $M = 28.966 \frac{\text{kg}}{\text{kmol}}$, $R_g = 8{,}314.5 \frac{\text{N·m}}{\text{kmol·K}}$, $T_i = 296\text{K}$, $\rho = 1.10 \frac{\text{kg}}{\text{m}^3}$, and $P_{atm} = 13.66\text{psi}$.

Using Equation A.5, the mass flow rate is calculated as

$$\dot{m} = CAP^{\frac{k+1}{2k}} \sqrt{\frac{kM}{R_g T_i P_i^{\frac{1-k}{k}}} \left(\frac{2}{k+1}\right)^{\frac{k+1}{k-1}}}$$

$$= (0.60)(1.131 \times 10^{-6}\text{m}^2)(861{,}800\text{Pa})^{\frac{1.40+1}{2(1.4)}} \sqrt{\frac{(1.40)\left(28.966 \frac{\text{kg}}{\text{kmol}}\right)}{\left(8{,}314.5 \frac{\text{N} \cdot \text{m}}{\text{kmol} \cdot \text{K}}\right)(296\text{K})(861{,}800\text{Pa})^{\frac{1-1.40}{1.40}}} \left(\frac{2}{1.40+1}\right)^{\frac{1.40+1}{1.40-1}}}$$

$$\dot{m} = 1.37 \times 10^{-3} \frac{\text{kg}}{\text{s}} = 8.24 \times 10^{-2} \frac{\text{kg}}{\text{min}}$$

$$Q = \frac{\dot{m}}{\rho} = \frac{8.24 \times 10^{-2}\,\frac{\text{kg}}{\text{min}}}{1.10\,\frac{\text{kg}}{\text{m}^3}} = 0.075\,\frac{\text{m}^3}{\text{min}} = 2.6\text{scfm}$$

The Clippard 15mm Miniature Valves selected (Part No. E215F-2W012) have a maximum flow rate of 2.6scfm, which matches the above calculations.

Most suppliers rate their valves using a flow coefficient, C_v, which is calculated for air undergoing critical flow by

$$C_v = \frac{Q\sqrt{T}}{11P}$$

where Q is in scfm, T is in °R, and P is in psia, so

$$C_v = \frac{Q\sqrt{T}}{11P} = \frac{(2.6\text{scfm})\sqrt{(533°\text{R})}}{11(125\text{psi} + 13.66\text{psi})}$$

$$C_v = 0.039$$

The ASCO 2-Way Miniature Valves selected (Part No. 411L2112HV) have a C_v value of 0.038[18], and so, based on the above calculations, they would fit the system well.

To find the flow coefficient necessary for a single valve assembly, Q, and therefore C_v, is simply increased by a factor of five because the outlet area now consists of five 1.2mm diameter orifices. That is,

$$(C_v)_{5-\text{valve}} = 5 \cdot (C_v)_{1-\text{valve}} = 5 \cdot (0.039)$$

$$= 0.195$$

The ASCO General Service Solenoid Valve selected (Part No. 8262H014) has a C_v value of 0.21[18], and so, based on the above calculations, it would fit the system well.

Appendix C

Pressure Transient MATLAB Code

```
 % This m-file will compute the pressure transient (the drop in
pressure
% over time) and the mass flow rate transient of a tank filled with
air
% with five square-edged orifice outlets for an array of orifice
diameters

clear all
close all

%  Inputs
d=input('\n Enter the inner diameter of the vessel in inches: ');
L=input('\n Enter the inner length of the vessel in inches: ');
P0=input('\n Enter the initial pressure in the vessel in psig: ');

% Convert inputs to SI units
d=d*0.0254;   % convert inches to meters
L=L*0.0254;   % convert inches to meters
P0=P0*6894.75728;    % convert psi to Pa

C=0.6;
V_T=pi/4*(d)^2*(L);
k=1.4;     % specific heat ratio of air
R=8314.5;    % universal gas constant
M=28.966;   % molecular weight of air
T0=296;    % initial temperature in kelvin

% Set the timeframe (t is given in seconds)
tmin=0;
tmax=1;

nstep=100;
tstep=(tmax-tmin)/nstep;

% Initialize vectors
t=tmin:tstep:tmax;
orif_dia=1:0.2:4;

% Initialize pressure and flow rate arrays
P_coll=zeros(101,16);
```

```
m_dot_coll=zeros(101,16);

% Run Simulation for different Orifice Diameters
for j=0:15;
    jj=j+1;
    A(jj)=5*((pi/4)*(orif_dia(jj)/1000)^2);

    % Initialize pressure and flow rate vectors
    P=zeros(nstep+1, 1);
    m_dot=zeros(nstep+1, 1);

    % Initial Conditions
    P(1)=P0;
    m_dot(1)=C*A(jj)*P(1)^((k+1)/(2*k))*sqrt((k*M)/(R*T0*P0^((1-
k)/k))*(2/(k+1))^((k+1)/(k-1)));


    % Run pressure tranisent
    for i=2:nstep+1
        P(i)=((t(i)-t(i-1))*((k-
1)/(2*k))*(C*A(jj)/V_T)*sqrt(((k^3)*R*T0*P0^((1-
k)/k))/(M)*(2/(k+1))^((k+1)/(k-1)))+P(i-1)^((1-k)/(2*k)))^((2*k)/(1-
k));
        m_dot(i)=C*A(jj)*P(i)^((k+1)/(2*k))*sqrt((k*M)/(R*T0*P0^((1-
k)/k))*(2/(k+1))^((k+1)/(k-1)));
    end
    P=P/6894.75728;     % Convert Pa back to psi
    P_coll(:,j+1)=P;    % compile all pressure transients
    m_dot_coll(:,j+1)=m_dot;    % compile all flow rate transients

    Pdrop(jj)=P(1)-P(length(P));
end

% Plotting and exporting data to Excel

B=[t',P_coll];
xlswrite('Pressure Transient Data.xlsx', B, 'Pressure Transient Data',
'A5:Q105')
plot(t,P_coll)
xlabel('Time t, s')
ylabel('Pressure P, psi')

figure(2)
BB=[t',m_dot_coll];
xlswrite('Pressure Transient Data.xlsx', BB, 'Mass Flow Rate Data',
'A5:Q105')
plot(t,m_dot_coll)
xlabel('Time t, s')
ylabel('Mass Flow Rate, kg/s')

figure(3)
```

```
plot(orif_dia, Pdrop)
xlabel('Orifice Diameter, mm')
ylabel('Pressure Drop, psi')
xlswrite('Pressure Transient Data.xlsx', [orif_dia', Pdrop'],
'Pressure Drop Data','A3:B18')
```

Appendix D

Supporting Figures

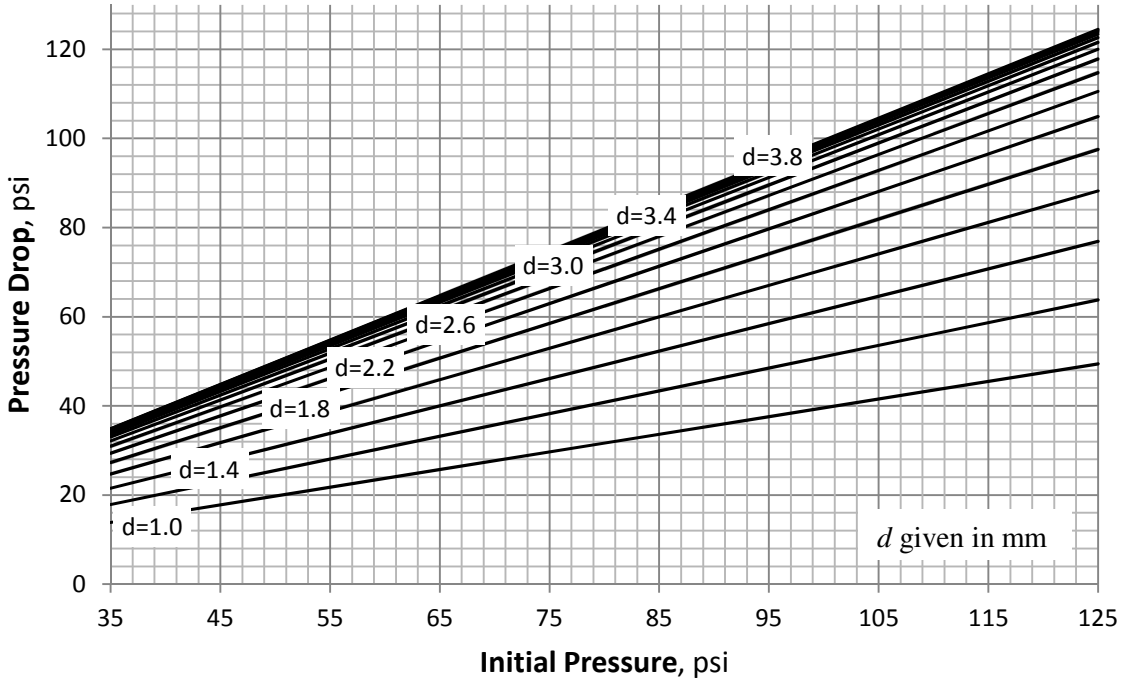

Figure D.1: Pressure Drop After 1.0 Second of Flow

Table D.1: Pressure Vessel Head Ratio Effects

Head Ratio R/H	Wall Thickness *(in)*	Max Von Mises Stress *(psi)*	Capacity *(in^3)*	Weight *(lbs)*
1.00	0.120	2406	109	1.52
	0.100	2879	111	1.27
	0.080	3588	114	1.03
	0.060	4769	116	0.77
	0.040	7135	119	0.52
1.25	0.120	2413	113	1.56
	0.100	2891	115	1.31
	0.080	3611	118	1.06
	0.060	4808	120	0.80
	0.040	7216	123	0.54
1.50	0.120	2441	115	1.60
	0.100	2924	118	1.34
	0.080	3693	120	1.08
	0.060	4989	123	0.81
	0.040	7714	126	0.55
1.75	0.120	3172	117	1.62
	0.100	3790	119	1.36
	0.080	4708	122	1.10
	0.060	6200	125	0.83
	0.040	9260	128	0.55
2.00	0.120	4047	118	1.64
	0.100	4866	121	1.38
	0.080	6086	123	1.11
	0.060	8112	126	0.84
	0.040	12263	129	0.56

Notes: Cylinderical Pressure Vessel with identical positive and negative heads. No outlets were included in this analysis in order to show the maximum von Mises stress in the heads. Simulated with internal pressure of 155psi. *Material: Aluminum 6061-T6.*

Table D.2: Pressure Vessel Mesh Definition

Element-Type	8-Noded Brick
Cylinder	
Axial Direction	40 elements
Sweep Direction	80 elements
Heads	
Radial Direction	40 elements
Sweep Direction	80 elements
Wall Thickness	2 elements

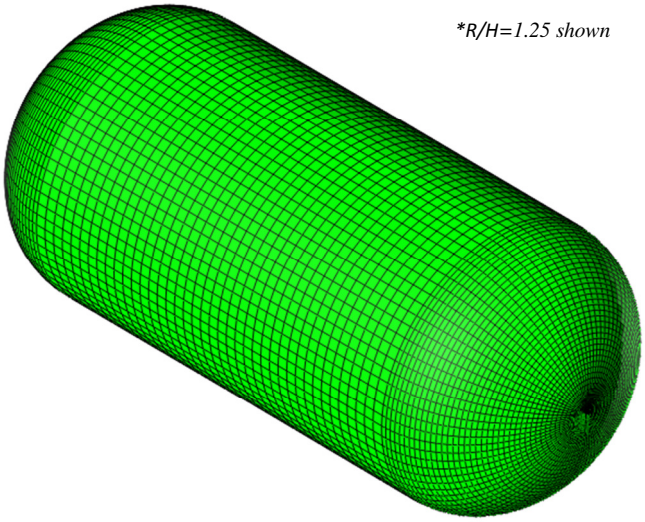

Figure D.2: Mesh Used in Pressure Vessel FEA – No outlets

Appendix E

Fabricated Part Drawings

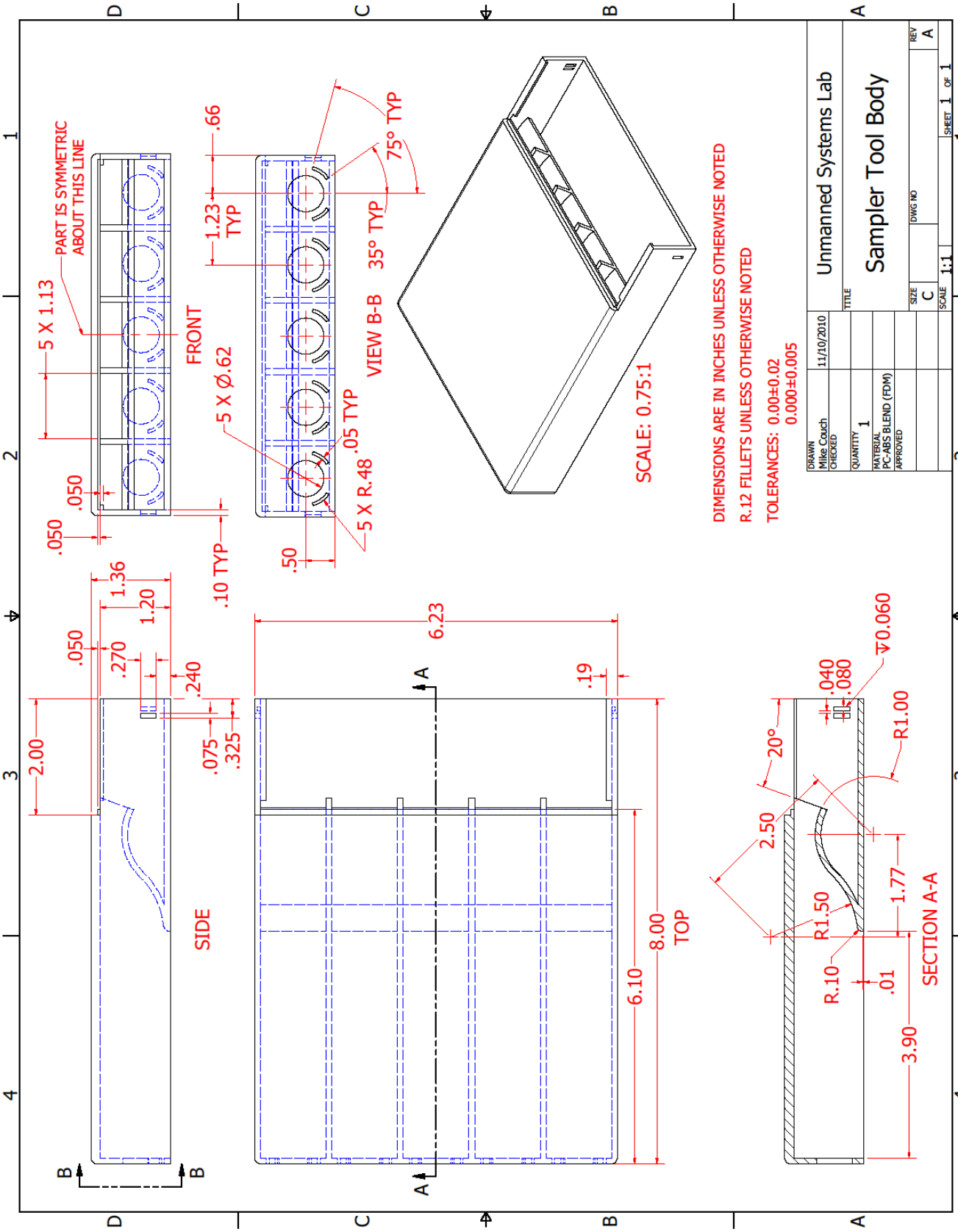
PART IS SYMMETRIC ABOUT THIS LINE
5 X 1.13
FRONT
.050
.050
.10 TYP
.66
1.23 TYP
75° TYP
35° TYP
VIEW B-B
5 X Ø.62
.05 TYP
5 X R.48
.50
SCALE: 0.75:1
DIMENSIONS ARE IN INCHES UNLESS OTHERWISE NOTED
R.12 FILLETS UNLESS OTHERWISE NOTED
TOLERANCES: 0.00±0.02
0.000±0.005
DRAWN Mike Couch 11/10/2010
CHECKED
QUANTITY 1
MATERIAL PC-ABS BLEND (FDM)
APPROVED
TITLE
Unmanned Systems Lab
Sampler Tool Body
SIZE C
DWG NO
REV A
SCALE 1:1
SHEET 1 OF 1
1.36
1.20
.050
.270
.240
2.00
.075
.325
SIDE
6.23
.19
8.00
6.10
TOP
A
A
B
B
.040
.080
⌀0.060
R1.00
20°
2.50
R1.50
R.10
1.77
.01
3.90
SECTION A-A

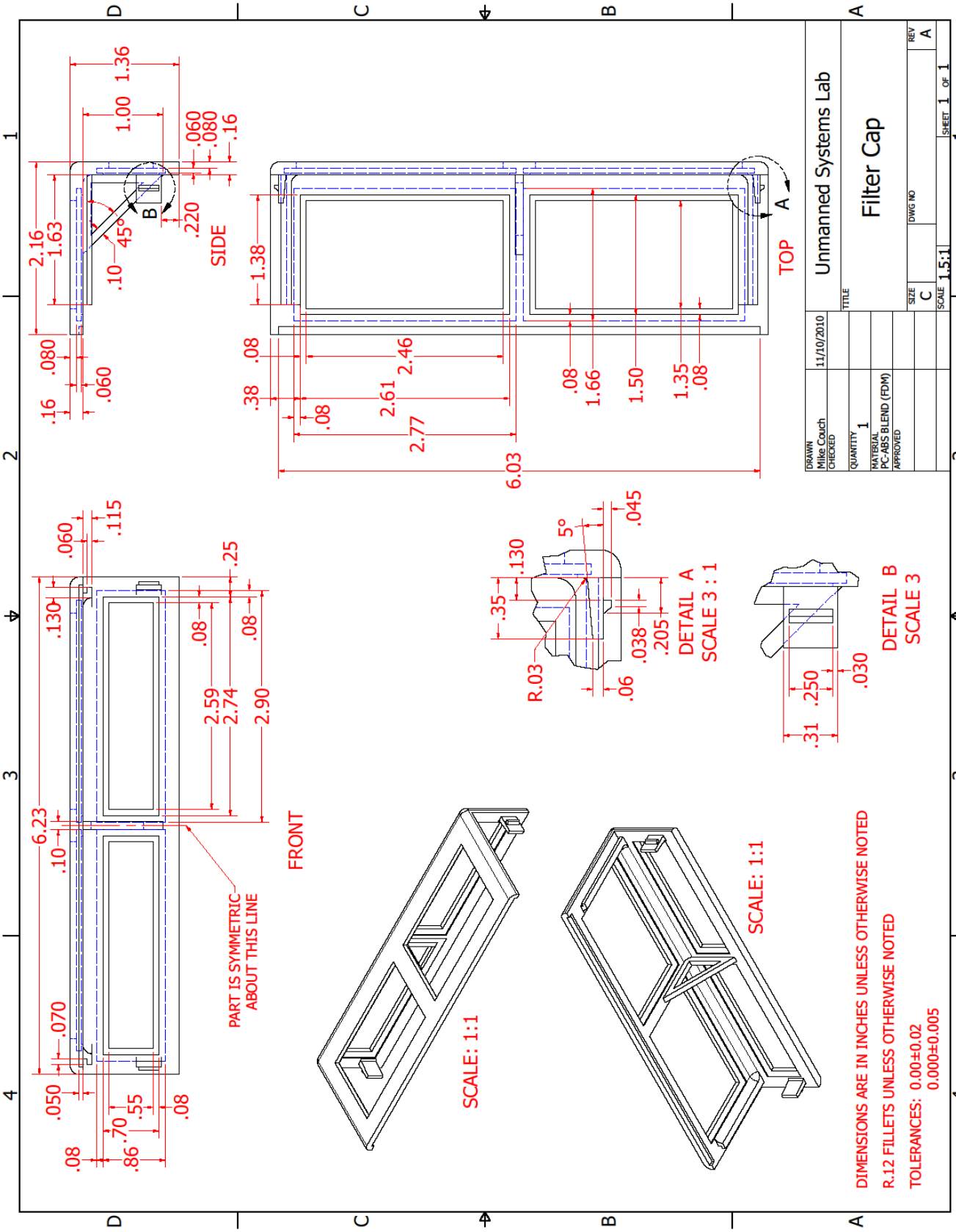
SIDE
TOP
FRONT
DETAIL A
SCALE 3 : 1
DETAIL B
SCALE 3
SCALE: 1:1
SCALE: 1:1
PART IS SYMMETRIC ABOUT THIS LINE
DIMENSIONS ARE IN INCHES UNLESS OTHERWISE NOTED
R.12 FILLETS UNLESS OTHERWISE NOTED
TOLERANCES: 0.00±0.02
0.000±0.005
DRAWN Mike Couch 11/10/2010
CHECKED
QUANTITY 1
MATERIAL PC-ABS BLEND (FDM)
APPROVED
TITLE
Unmanned Systems Lab
Filter Cap
SIZE C
SCALE 1.5:1
DWG NO
REV A
SHEET 1 OF 1

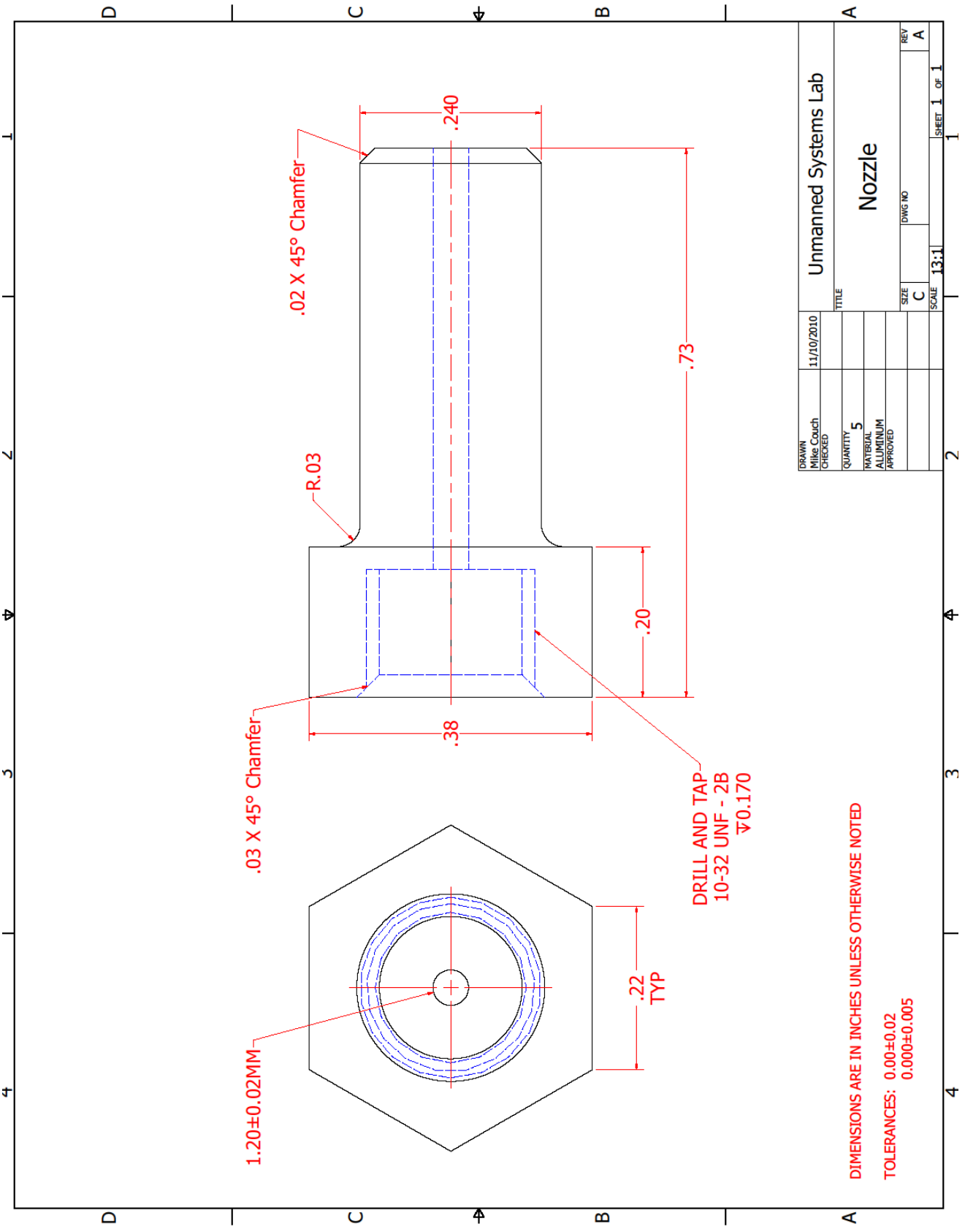
.240
.02 X 45° Chamfer
.73
R.03
.20
.38
.03 X 45° Chamfer
DRILL AND TAP
10-32 UNF - 2B
↧0.170
1.20±0.02MM
.22
TYP
DIMENSIONS ARE IN INCHES UNLESS OTHERWISE NOTED
TOLERANCES: 0.00±0.02
0.000±0.005
DRAWN Mike Couch 11/10/2010
CHECKED
QUANTITY 5
MATERIAL ALUMINUM
APPROVED
TITLE
Unmanned Systems Lab
Nozzle
SIZE C
DWG NO
REV A
SCALE 13:1
SHEET 1 OF 1

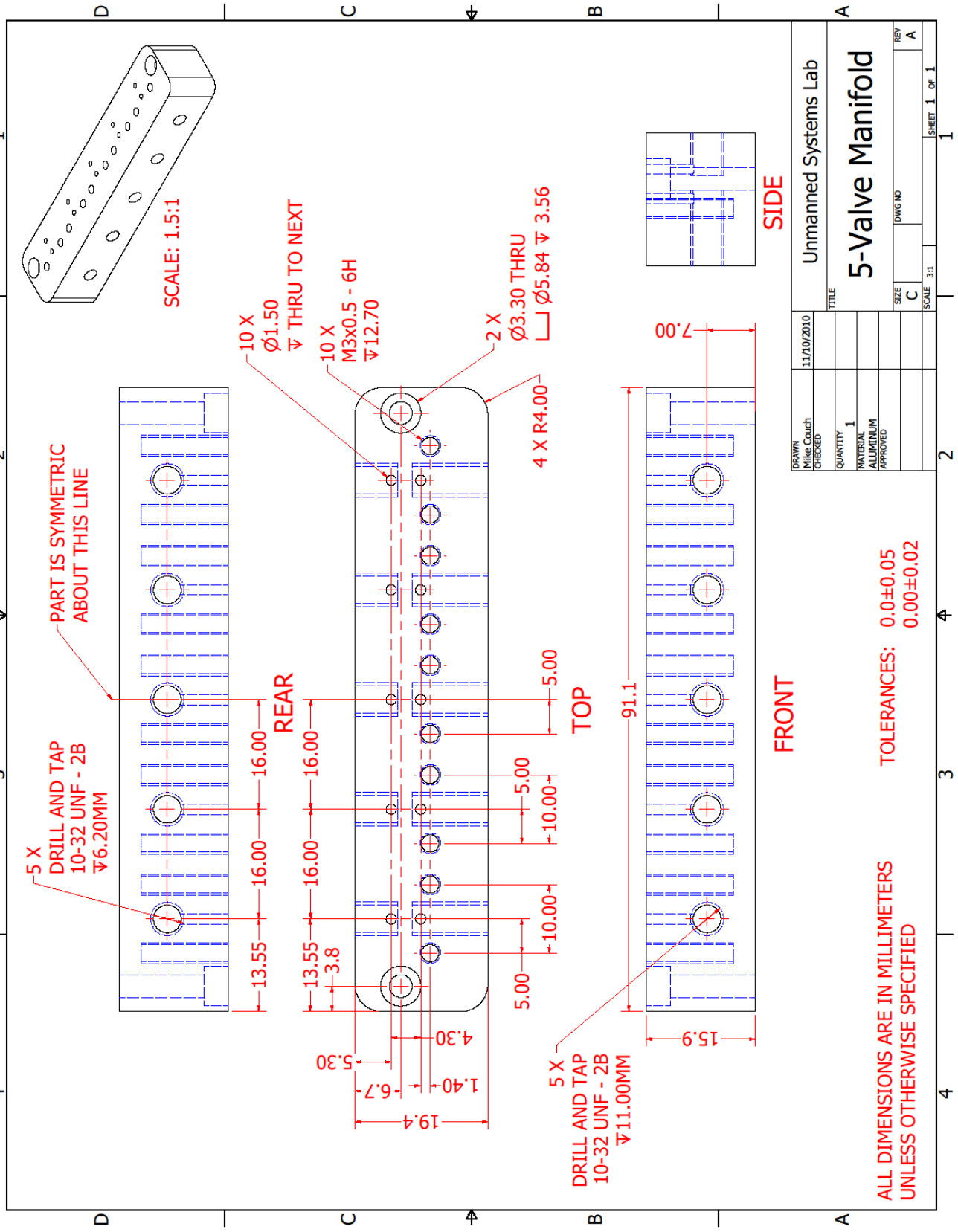
SCALE: 1.5:1
SIDE
FRONT
TOP
REAR
PART IS SYMMETRIC
ABOUT THIS LINE
5 X
DRILL AND TAP
10-32 UNF - 2B
↧6.20MM
10 X
Ø1.50
↧ THRU TO NEXT
10 X
M3x0.5 - 6H
↧12.70
2 X
Ø3.30 THRU
⌴ Ø5.84 ↧ 3.56
4 X R4.00
5 X
DRILL AND TAP
10-32 UNF - 2B
↧11.00MM
16.00
13.55
3.8
5.00
10.00
91.1
7.00
15.9
4.30
5.30
1.40
6.7
19.4
DRAWN Mike Couch 11/10/2010
CHECKED
QUANTITY 1
MATERIAL ALUMINUM
APPROVED
TITLE
5-Valve Manifold
Unmanned Systems Lab
SIZE C
DWG NO
REV A
SCALE 3:1
SHEET 1 OF 1
TOLERANCES: 0.0±0.05
0.00±0.02
ALL DIMENSIONS ARE IN MILLIMETERS
UNLESS OTHERWISE SPECIFIED

Appendix F

Rapid Prototype Material Data Sheets

Used under Fair Use Guidelines

STRATASYS

Polycarbonate

A true industrial thermoplastic, PC (polycarbonate) is widely used in automotive, aerospace, medical and many other applications. PC offers accuracy, durability and stability, creating strong parts that withstand functional testing. It also has superior mechanical properties to ABS and a number of other thermoplastics. When combined with Stratasys FDM (Fused Deposition Modeling) systems, PC gives you Real Parts™ for producing design verification prototypes and manufacturing end-use parts. Refer to the FDM System Material Availability spec sheet for system availability and color options.

Mechanical Properties[1]	Test Method	Imperial	Metric
Tensile Strength, Type 1, 0.125	ASTM D638	7,600 psi	52 MPa
Tensile Modulus, Type 1, 0.125	ASTM D638	290,000 psi	2,000 MPa
Tensile Elongation, Type 1, 0.125	ASTM D638	3 %	3 %
Flexural Strength	ASTM D790	14,000 psi	97 MPa
Flexural Modulus	ASTM D790	310,000 psi	2,137 MPa
IZOD Impact, notched	ASTM D256	1 ft-lb/in	53.39 J/a
IZOD Impact, un-notched	ASTM D256	5 ft-lb/in	266.95 J/a

Thermal Properties	Test Method	Imperial	Metric
Heat Deflection Temperature @ 66 psi	ASTM D648	280° F	138° C
Heat Deflection Temperature @ 264 psi	ASTM D648	261° F	127° C
Glass Transition Temperature (Tg)	DMA (SSYS)	322° F	161° C
Coefficient of Thermal Expansion	---------	3.8E-05 in/in/F	-----
Melt Point	---------	Not Applicable[2]	Not Applicable[2]

Other	Test Method	Value
Specific Gravity	ASTM D792	1.2
Rockwell Hardness	ASTM D785	R115
Flame Classification	UL 94	V2, 1.1 mm
Dielectric Strength kV/mm	IEC 60112	15
Dielectric Constant @ 60Mhz	IEC 60250	3.17
Dielectric Constant @ 1Mhz	IEC 60250	2.96

The information presented are typical values intended for reference and comparison purposes only. They should not be used for design specifications or quality control purposes. End-use material performance can be impacted (+/-) by, but not limited to, part design, end-use conditions, test conditions, etc. Actual values will vary with build conditions. Tested parts were built on Titan Ti, 0.010 inch slice (0.245mm).

[1] Build orientation is on side edge. [2] Do to amorphous nature, material does not display a melting point.

STRATASYS®

Polycarbonate-ABS

PC-ABS (polycarbonate-ABS) is one of the most widely used industrial thermoplastics. PC-ABS offers the most desirable properties of both materials - the superior mechanical properties and heat resistance of PC and the excellent features of ABS. PC-ABS blends are commonly used in automotive, electronics and telecommunications applications. When combined with Stratasys FDM (Fused Deposition Modeling) systems, PC-ABS gives you Real Parts™ for conceptual prototyping through design verification through direct digital manufacturing. Refer to the FDM System Material Availability spec sheet for system availability and color options.

Mechanical Properties[1]	Test Method	Imperial	Metric
Tensile Strength, Type 1, 0.125	ASTM D638	5,040 psi	34.8 MPa
Tensile Modulus, Type 1, 0.125	ASTM D638	265,000 psi	1,827 MPa
Tensile Elongation, Type 1, 0.125	ASTM D638	4.3 %	4.3 %
Flexural Strength	ASTM D790	8,600 psi	50 MPa
Flexural Modulus	ASTM D790	270,000 psi	1,863 MPa
IZOD Impact, notched	ASTM D256	2.3 ft-lb/in	123 J/a
IZOD Impact, un-notched	ASTM D256	6.1 ft-lb/in	326 J/a

Thermal Properties	Test Method	Imperial	Metric
Heat Deflection Temperature @ 66 psi	ASTM D648	230° F	110° C
Heat Deflection Temperature @ 264 psi	ASTM D648	205° F	96° C
Glass Transition Temperature (Tg)	DMA (SSYS)	257° F	125° C
Vicat Softening	ASTM D1525	234° F	112° C
Coefficient of Thermal Expansion	---------	4.10E-5 in/in F	------
Melt Point	---------	Not Applicable[2]	Not Applicable[2]

Other	Test Method	Value
Specific Gravity	ASTM D792	1.20
Density	ASTM D792	0.0397 lb/in^3 (1.1 gr/cm^3)
Flame Classification	UL 94	HB 0.85mm
Rockwell Hardness	ASTM D785	R110
Dielectric Strength kV/mm	IEC 60112	35
Dielectric Constant @ 100Hz	IEC 60250	3.1
Dielectric Constant @ 1Mhz	IEC 60250	3.0

The information presented are typical values intended for reference and comparison purposes only. They should not be used for design specifications or quality control purposes. End-use material performance can be impacted (+/-) by, but not limited to, part design, end-use conditions, test conditions, etc. Actual values will vary with build conditions. Tested parts were built on Titan Ti, 0.010 inch slice (0.245mm).

[1] Build orientation is on side edge. [2] Do to amorphous nature, material does not display a melting point.